

PENNSTATE



Department of Meteorology  
College of Earth and Mineral Sciences

(814) 865-0478  
(814) 865-0479  
FAX: (814) 865-3663

The Pennsylvania State University  
503 Walker Building  
University Park, PA 16802-5013

October 27, 1994

Dr. David O. Starr  
Laboratory for Atmospheres  
NASA/Goddard Space Flight Center  
Code 913  
Greenbelt, MD 20771

*FINAL*  
*IN-46-CR*  
*9 CIT.*  
*30665*  
*91P*

Re: NASA Goddard Earth Sciences Graduate Student Program  
Research Grant Number NAG 5-1810

Dear Dr. Starr:

This is a final technical report on the academic achievements of Dr. Gerald Mace, who was the recent recipient of a graduate fellowship from the NASA Goddard Earth Science Graduate Student Program (NGESGSP). Gerald successfully completed all requirements for the degree of Doctor of Philosophy and graduated from The Pennsylvania State University in May, 1994. The title of Gerald's doctoral dissertation is "Development of Large-Scale Diagnostic Analysis Techniques Applicable to Regional Arrays of Wind Profilers and Radiosondes."

The enclosed curriculum vita summarizes the presentations given and papers published during Gerald's tenure as a NGESGSP Fellow. Most of his work centered around the First International Satellite Cloud Climatology Project Regional Experiment (FIRE Cirrus II) held in Coffeyville, KS, during November and December, 1991, where he served as lead weather forecaster for the field project. Data collected during this period were subsequently analyzed by Gerald and led to the bulk of the results discussed in his doctoral dissertation. Other major projects in which Gerald participated while a NGESGSP Fellow included the US Department of Energy's Atmospheric Radiation Measurement Program and NASA's deployment to Townsville, Australia during January and February, 1993, as part of the Tropical Oceans Global Atmosphere Coupled Ocean-Atmosphere Response Experiment where he provided weather forecasting support.

A major portion of Gerald's work has recently been accepted to the FIRE Cirrus II special issue of the Journal of Atmospheric Sciences. It is entitled "Examination of coupling between an upper tropospheric cloud system and synoptic-scale dynamics diagnosed from wind profiler and radiosonde data." Gerald is lead author on this work with three co-authors including yourself, myself and Patrick Minnis of NASA Langley. This manuscript is attached as the scientific portion of this final report. In addition,



**Publications** (*conference proceedings*)

- Long, C.N., T.P. Ackerman and G.G. Mace, 1994: Surface radiation studies from the ARM/PROBE project. *Science Data Workshop II for TOGA COARE Proceedings*, Albuquerque, NM, Mar. 15-17, 66-69.
- Mace, G. G., and T. P. Ackerman, 1994: On the utilization of remotely sensed data in support of the ARM single column modeling concept. *Proceedings from the Third International Symposium on Tropospheric Profiling: Needs and Technologies*, Hamburg, Germany, Aug. 30 - Sep. 2, 142-144.
- Mace, G. G., D. O'C. Starr, P. Minnis and T. P. Ackerman, 1994: Modulation of cloud optical properties by vertical circulations associated with a jet-streak exit region: The November 26 FIRE cirrus case study. In *Preprints of the Eighth Conference on Atmospheric Radiation*, Jan. 23-28, Nashville, TN, 217-219.
- Mace, G.G., and T.P. Ackerman, 1993: Examination of the observed synoptic scale cirrus cloud environment: The December 3-6 FIRE cirrus case study. *FIRE Cirrus Science Conference Proceedings*, Breckenridge, CO, June 14-17, 130.
- Mace, G.G., and T.P. Ackerman, 1993: Cirrus cloud development in a mobile upper tropospheric trough: The November 26th FIRE cirrus case study. *FIRE Cirrus Science Conference Proceedings*, Breckenridge, CO, June 14-17, 134.
- Mace, G. G., T. P. Ackerman and E. Clothiaux, 1993: Mesoscale diagnostic quantities from arrays of Doppler wind profilers and radiosondes. In *Preprints of the Fourth Symposium on Global Change Studies*, Jan. 17-22, Anaheim, CA, 53-56.
- Mace, G. G., and T. P. Ackerman, 1992: Large scale forcing of middle and upper level clouds: preliminary results from a FIRE cirrus case study. In *Proceedings from the 11th International Conference on Clouds and Precipitation*, Aug. 17-21, Montreal, Canada, 541-544.

**Invited Oral Presentations**

Examination of coupling between an upper tropospheric cloud system and synoptic scale dynamics diagnosed from wind profiler and radiosonde data. GKSS, Geesthacht, Germany, 8/28/94.

1. The first part of the document discusses the importance of maintaining accurate records of all transactions. It emphasizes that proper record-keeping is essential for the integrity of the financial system and for the ability to detect and prevent fraud. The text notes that without reliable records, it would be difficult to verify the accuracy of financial statements and to identify any irregularities.

2. The second part of the document outlines the specific requirements for record-keeping. It states that all transactions must be recorded in a clear and concise manner, using standardized formats and codes. This ensures that the information is easily accessible and can be analyzed consistently across different departments and time periods.

3. The third part of the document addresses the issue of data security. It highlights the need to implement robust security measures to protect sensitive financial information from unauthorized access, loss, or destruction. This includes the use of encryption, secure storage, and regular backups to ensure the continuity and confidentiality of the data.

4. The fourth part of the document discusses the role of technology in record-keeping. It notes that the use of modern accounting software and digital storage solutions can significantly improve the efficiency and accuracy of the record-keeping process. However, it also stresses the importance of ensuring that these technologies are properly implemented and maintained to avoid any potential risks.

5. The fifth part of the document concludes by emphasizing the overall importance of record-keeping in the financial system. It reiterates that accurate and secure records are the foundation of sound financial management and are crucial for the long-term success and stability of any organization.

6. The sixth part of the document provides a summary of the key points discussed and offers recommendations for further action. It suggests that organizations should regularly review their record-keeping practices to ensure they are up-to-date and effective, and should seek professional advice if needed to address any specific challenges.

7. The seventh part of the document contains a list of references and sources used in the document. This includes various accounting standards, industry best practices, and relevant legislation that guide the record-keeping process.

8. The eighth part of the document is a concluding statement that expresses the author's commitment to providing accurate and reliable information. It states that the information provided in this document is based on the best available knowledge and is intended to serve as a helpful guide for anyone involved in financial record-keeping.

***NASA Goddard Earth Sciences  
Graduate Student Program***

**NAG 5-1810**

Principal Investigator : **Thomas P. Ackerman**  
Fellowship: **Gerald G. Mace**  
NASA Technical Officer: **David O. Starr**

**Final Technical Report**



**Examination of Coupling Between an Upper Tropospheric Cloud System and Synoptic-Scale Dynamics Diagnosed from Wind Profiler and Radiosonde Data**

Gerald G. Mace

*Department of Meteorology  
The Pennsylvania State University*

David O'C. Starr

*Climate and Radiation Branch  
Goddard Space Flight Center*

Thomas P. Ackerman

*Department of Meteorology  
The Pennsylvania State University*

Patrick Minnis

*Atmospheric Sciences Division  
NASA Langley Research Center*

Submitted to *Journal of the Atmospheric Sciences*





## Abstract

The evolution of synoptic-scale dynamics associated with a middle and upper tropospheric cloud event that occurred on 26 November 1991 is examined. The case under consideration occurred during the FIRE CIRRUS-II Intensive Field Observing Period held in Coffeyville, KS during Nov. and Dec., 1991. Using data from the wind profiler demonstration network and a temporally and spatially augmented radiosonde array, emphasis is given to explaining the evolution of the kinematically-derived ageostrophic vertical circulations and correlating the circulation with the forcing of an extensively sampled cloud field. This is facilitated by decomposing the horizontal divergence into its component parts through a natural coordinate representation of the flow. Ageostrophic vertical circulations are inferred and compared to the circulation forcing arising from geostrophic confluence and shearing deformation derived from the Sawyer-Eliassen Equation. It is found that a thermodynamically indirect vertical circulation existed in association with a jet streak exit region. The circulation was displaced to the cyclonic side of the jet axis due to the orientation of the jet exit between a deepening diffluent trough and building ridge. The cloud line formed in the ascending branch of the vertical circulation with the most concentrated cloud development occurring in conjunction with the maximum large-scale vertical motion. The relationship between the large scale dynamics and the parameterization of middle and upper tropospheric clouds in large-scale models is discussed and an example of ice water contents derived from a parameterization forced by the diagnosed vertical motions and observed water vapor contents is presented.



## 1. Introduction

In his review article, Liou (1986) states that cirrus clouds are one of the most important yet least understood components of the climate system. Covering as much as one-third of the earth's surface and having unique microphysical and radiative characteristics, cirrus undoubtedly has a profound influence on climate. The ability to characterize accurately these upper-tropospheric ice-phase clouds in General Circulation Models (GCMs) has long been recognized as a serious shortcoming of present-day simulations of future and past climate. Cirrus clouds present a multi-faceted challenge that spans the entire range of the cloud parameterization problem. At the smallest scales, the optical characteristics of cirrus that stem, in large part, from complicated crystal characteristics, are not well known and, therefore, difficult to accurately represent in a GCM parameterization. At smaller scales, cirrus clouds owe their existence primarily to turbulent motions. However, as shown in the modeling studies of Starr and Cox (1985a and b), the meso-synoptic scale ascent is quite important to the evolution of the macroscopic cloud properties. Macroscopic characteristics such as cloud thickness, aerial coverage and optical depth have been shown to be quite sensitive to the large-scale vertical motion. This sensitivity to the large-scale ascent contributes to the mesoscale organization of cirrus cloud systems documented in several case studies (Sassen, et al., 1989, Starr and Wylie, 1990).

The fact that cirrus cloud systems tend to be organized on scales approaching that of current GCMs makes realistic parameterization of cirrus an achievable goal. This presumes that relationships between the model dynamics and thermodynamics and the occurrence and characteristics of non-convective cirrus cloud are well understood. This is not, however, the case. Most GCMs diagnose the presence of supersaturation clouds in the upper troposphere based on undocumented relationships between cirrus occurrence and relative humidity (Slingo, 1987). The optical properties are, then, specified based on cloud height. While the humidity undoubtedly plays a crucial role in the existence of cirrus clouds, well-established statistical relationships between upper tropospheric relative humidity on any scale and the resulting cloud fraction, cloud depth or optical characteristics do not as yet exist. This is largely due to the difficulty of accurately measuring water vapor content at cold upper tropospheric temperatures (Starr and Melfi, 1991). As pointed out by Slingo (1987), several additional parameters may be useful in leading to correct diagnoses of the presence of cloud. These are the vertical velocity, stability and vertical wind shear. Considering the coarse vertical resolution of most GCMs relative to the observed scales of many cirrus layers (Starr and Wylie, 1990), Richardson Number considerations would not be useful as a diagnostic

since they ultimately depend on the depth over which the vertical finite differencing is conducted. This was shown in a radiosonde study by Starr and Cox (1980) where Richardson Numbers were found to be poor predictors of the presence of cirrus. The vertical resolution of the soundings they used was somewhat finer than that of most GCMs.

An example of a physically based parameterization that uses the large scale vertical velocity and the observed relative humidity is the ice water content parameterization described by Heymsfield and Donner (1990; hereafter referred to as the HD parameterization). This parameterization uses an expression that balances crystal sedimentation with vapor deposition. Ultimately, it is the large scale vertical velocity and the water vapor availability that determine the quantity of ice in a particular layer. Essentially, the HD parameterization is a diagnostic synthesis of the physics used in the cirrus model of Starr and Cox (1985a).

In a recent study, Soden and Donner (1994), using ECMWF analyses and ISCCP cloud products, demonstrated that the HD parameterization is able to capture the spatial variability of optical depth on global scales. However, they noted large discrepancies between the absolute values of the parameterized and satellite-derived optical depths. While several factors may have contributed to the differences, the largely unknown relationship between large scale vertical velocity and cirrus microphysical characteristics certainly contributed. This is evidenced by a strong latitudinal dependence of the discrepancies in their July study, the largest differences occurring in the southern hemisphere. While model error may have been a factor in the data-sparse Southern Hemisphere, it is equally likely that the cirrus formed in the baroclinic regions of the Austral Winter was fundamentally different from the cirrus formed in the more convectively active tropics and summer hemisphere. The relationship between the bulk optical characteristics of cirrus and the synoptic regime in which they form is not presently understood. This lack of knowledge represents a fundamental deficiency in our ability to characterize accurately cloud-climate interaction in GCMs.

An improved understanding of the instantaneous radiative transfer through observed cirrus will *not* benefit climate prediction efforts unless a concomitant connection is achieved unambiguously between the clouds being studied and the actual dynamics on multiple scales. Furthermore, even though a correct diagnosis of the large-scale ascent and upper tropospheric humidities is crucial, simply knowing these quantities is insufficient. The radiative characteristics of cirrus in a particular situation are undoubtedly a reflection of the history of the airmass in which they have formed (Sassen et al. 1994). The evolution of the vertical motions and the upper tropospheric water vapor fields must be placed into the context of the evolving dynamics. In short, to advance toward the stated goals of FIRE (Starr, This Issue),

it is requisite upon us to quantitatively connect the observed radiative transfer and microphysics to a thorough and verifiable explanation of the observed GCM-resolvable large scale dynamics.

The association of cirrus with midlatitude synoptic regimes has a long history in the literature (Stone, 1957; Conover, 1960). Heymsfield (1977) presented a detailed aircraft-based study of cirrus formation in a spectrum of midlatitude synoptic situations. Shapiro (1978) suggested using satellite-observed cirriform cellular structure as a means of diagnosing the turbulent scales associated with certain jet flows. Sassen et al. (1989) using lidar and radiosonde data, correlated the occurrence of cirrus with subtropical jet streams and elevated frontal zones. Using radiosonde network analyses and surface-based lidar and aircraft observations, Starr and Wylie (1990) analyzed several cirrus events associated with the passage of a jet streak and upper tropospheric ridge. They found strong evidence for mesoscale organization of the cloud decks and noted that the cirrus formed in association with lower tropospheric weather systems although this association was due to a natural superposition of separate forcings rather than a common cause. They demonstrated that large scale vertical motions in the cirrus generating regions tended to be about  $5\text{-}7\text{ cm s}^{-1}$  although unambiguous estimates of the large-scale ascent could not be made in all cases.

In explaining the meso- and larger-scale dynamics of the cirrus events presented below, we will couch the explanation in terms of vertical circulations forced in jet flows (Keyser and Shapiro, 1986). In a straight jet streak with negligible thermal advection, transverse ageostrophic motions associated with along-stream parcel accelerations lead to thermodynamically direct (indirect) vertical circulations in the jet entrance (exit) region. The vertical branches of these cells tend to straddle the jet axis with the relative magnitudes of the vertical and horizontal branches proportional to the potential vorticity, as can be seen by examining the Sawyer-Eliassen equation (Keyser and Shapiro, 1986). More generally the thermal advection cannot be neglected owing to the phase lags between the thermal and momentum fields. Therefore, cold (warm) air advection is typically found in the entrance (exit) region. The combined effect of thermal advection and horizontal shear tend to shift the vertical circulations laterally. For instance, cold air advection in the entrance region of jet tends to shift the transverse ageostrophic circulation to the anticyclonic side of the jet axis. The placement of the descending branch beneath the jet axis in the entrance region occurs in association with elevated frontal zones and tropopause folds (Keyser and Shapiro, 1986). Arguing from gradient wind concepts, Keyser and Shapiro (1986) conjectured that when a jet is placed at the base of a long-wave trough, the along-stream ageostrophic motions induced by flow curvature will reinforce the vertical branches of the ageostrophic motions. It is the modulation of the ascending branches of the ageostrophic circulations by the flow field

dynamics and their superposition with the upper tropospheric moisture field that are of direct importance to the development and maintenance of cirrus cloud decks. For instance, Sassen et al. (1994) describe several cirrus events that displayed unusual microphysical and optical characteristics. It was shown that the characteristics of these clouds came about through complicated history of tropopause folds associated with polar and subtropical jet streaks. The injection of stratospheric aerosol into the upper troposphere interacted with subtropical moisture layers in the jet entrance regions to form these clouds. The dynamical history of the airmass was all-important to the resulting cirrus cloud characteristics.

Placing cloud evolution into a dynamical context can be accomplished quite efficiently using cloud-resolving mesoscale models (Jensen et al., this issue). However, in such studies it is difficult to attribute discrepancies between observation and model output to the simulated dynamics or the cloud modeling algorithm. In order to compliment the mesoscale modeling efforts, we have implemented an analysis scheme based exclusively on combined wind profiler and radiosonde data. While a measure of uncertainty exists in the data, this uncertainty is generally quantifiable and places known bounds on the objectively analyzed quantities. The resulting description of the synoptic scale dynamics represents a ground truth against which finer-scale models can be compared.

While the dynamical characteristics of elevated jet streaks have been discussed theoretically and diagnosed in the output of idealized models, few studies have used observations. A notable exception is the work of Shapiro (1981) who solved the Sawyer-Eliassen equation with the forcing defined via analysis of radiosonde and aircraft data. He demonstrated that horizontal shear of the geostrophic wind in the cross-stream direction acting on along front thermal gradients can force mid-tropospheric subsident motions. The front examined by Shapiro displayed a direct vertical circulation in the lower troposphere while an indirect circulation was diagnosed in the upper troposphere. More recently, Sanders (1990) examined an intense northwesterly jet and investigated the evolution of the potential vorticity field and strong subsidence beneath the jet core forced by cold air advection. Cammas and Ramond (1989) used ECMWF analyses to decompose the horizontal divergence and ageostrophic wind in a natural coordinate reference frame to show that the association of flow curvature with along-stream speed accelerations can significantly modify the classical models derived from the Sawyer-Eliassen equation and gradient wind concepts.

We will adopt the conceptual approach of Cammas and Rammond (1989) in this study. Working from objectively analyzed wind profiler and radiosonde data, the transverse ageostrophic circulation and its associated forcing will be estimated. The vertical circulations will be combined with analyses of the thermodynamic and water vapor structure in the upper troposphere to describe the evolution of a middle and upper tropospheric cloud

field sampled during the FIRE Cirrus-II field campaign. The diagnosed dynamics and thermodynamics will be combined with the water vapor field in the HD parameterization to demonstrate the advantage of using data-based techniques to evaluate and improve cloud parameterizations.

## **2. Data Processing and Analysis Techniques**

The goal of the analysis presented herein is to document the evolution of the synoptic scale dynamical mechanisms important to regional cloud formation. Given typical spacing between observing points of 175-200 km, the characteristics of the synoptic scale dynamics are well resolved. While the dynamics on the mesoscale can be inferred from the data in certain cases, the spacing between data points precludes a quantitative analysis of the spatial characteristics of the meso- and smaller-scale features. Therefore, the data processing and analysis techniques described below are specifically designed to remove atmospheric signal below the spatial resolution of the network.

### **2a. Initial Processing of Wind Profiler Data**

The diagnostic analyses presented below rely exclusively on data collected from the Wind Profiler Demonstration Network (WPDN; Chadwick, 1986) and the spatially and temporally augmented conventional radiosonde network. Fig. 1 shows the geographic distribution of the radiosonde network and WPDN as it existed in November 1991. The WPDN, composed of 18 profilers, existed in a roughly 350 km wide swath from southeast Wyoming to northern Louisiana. We will refer to the hexagonal array of wind profilers centered on the Lamont, OK (LMN) profiler as the inner array of the WPDN. Coffeyville, KS, the operational hub of the FIRE CIRRUS-II IFO, is located at the northeast vertex of the inner array approximately 30 km south of the Neodesha, KS (NDS) profiler. Note that a special network of four cross-chain linked atmospheric sounding systems (CLASS) was situated such that Coffeyville was centered on the eastern side of an approximately equilateral triangle. The location of an array of National Weather Service (NWS) radiosonde stations that conducted three hourly soundings during the case study period are also shown in Fig. 1. The operational modes of the radiosonde networks (CLASS and NWS) are described by Starr (this issue).

The WPDN wind profilers, which operate at a frequency of 404.37 MHz, a wavelength of 74 cm, provide two modes of data sampling, a high mode and a low mode. The low mode is designed to sample the lower troposphere and provides measurements from

500 m above ground level (AGL) to 9.25 km AGL. The vertical resolution in this mode is 250 m with 250 m gate spacing. The high mode provides measurements from 7.5 km to 16.25 km AGL. This mode provides 1 km vertical resolution and 250 m gate spacing. Shorter pulse widths are used in the low mode and enable a higher vertical resolution. However, low signal to noise frequently becomes a problem for this mode above approximately five to six kilometers. Therefore, the high mode observations are always used where the modes overlap, sacrificing vertical resolution for better overall data quality in the middle troposphere. For further details concerning wind profiler technology, the reader is referred to Gage and Balsley (1978). The wind profiler data used in this study are hourly averaged horizontal winds derived from the six-minute Doppler moments. As described in detail by Mace (1994), a consensus averaging scheme (Strauch et al., 1981; Fischler and Bolles, 1984) was applied to remove erroneous observations from the moments time series. After converting the radial velocities to horizontal components, a running hourly average, centered on the nominal observation time, was applied to create the hourly mean horizontal winds. The hourly averaged winds were hand filtered to remove any obviously bad data from the time series and all winds were linearly interpolated to 250 m height increments above mean sea level up to 15 km. This technique was applied to all data collected by the WPDN profilers during the FIRE Cirrus-II field campaign.

The regional proximity of the WPDN to the FIRE Cirrus-II operational area provides an opportunity for investigation of the wind field throughout the troposphere and lower stratosphere. Apart from the obvious sampling differences between radiosondes and wind profilers, the primary advantage of the WPDN observations is their nominal 1 hour temporal resolution. However since the length scales resolved by observations spaced at approximately 250 km are on the order of 1500-2000 km (Thiebaut and Pedder, 1987; Davies-Jones, 1993; Mace, 1994), one hour temporal resolution may be more than is needed to adequately characterize the synoptic-scale evolution of meteorological features. Therefore, to take full advantage of the temporal resolution of the WPDN data, a time-space conversion scheme is applied. Described in Appendix A, this algorithm takes the observations collected 1 hour before and after a particular time and places them along a curved trajectory streamline estimated from the spatial and temporal characteristics of the wind field. The assumption is made that the only acceleration acting on the air parcels is the centripetal acceleration required to maintain the parcels on the curved trajectory. While this scheme effectively coarsens the temporal resolution to 3 hours, the number of observations available every third hour increases substantially, thereby, decreasing the uncertainty in horizontal derivatives diagnosed from the wind fields (Davies-Jones, 1993). This is



especially advantageous in the inner array of the WPDN where, under ideal circumstances, a dense network of observations can be created from the 7 available profilers.

## 2b. Initial Processing of Radiosonde Data

All radiosonde data collected during FIRE Cirrus-II were processed at full vertical resolution. The raw NWS radiosonde data has six second (roughly 30 m) vertical resolution and consists of temperature, pressure, humidity and elevation and azimuth angles. Processing of the raw data combined several steps designed to generate a research product interpolated to pressure levels at 40 to 60 meter vertical resolution. The data were scanned for obvious or potential errors such as increasing pressure with height or for values that had been previously flagged or interpolated by the NWS processing routines. The raw pressure, elevation and azimuth angle data were smoothed using a variable-width, multi-pass regression technique that was designed to reduce Root Mean Square (RMS) uncertainty in the derived products. Using the smoothed pressure time series, the time series of standard pressure levels was determined and the observed temperature and relative humidity profiles were interpolated to the standard levels. Location information was generated at the standard pressure levels using the smoothed elevation and azimuth angles. Horizontal winds were then calculated using a centered differencing scheme with the location data. Quality flags were assigned to each sounding using manual inspection.

Further processing of the radiosonde soundings was motivated by the desire to combine the mass and water vapor fields observed by the radiosondes with simultaneous WPDN wind observations. While both sets of observations ultimately compliment one another, meshing data from the two observational platform types into a dynamically consistent whole needs to be carefully considered. The wind profilers provide horizontal wind velocities in 250-meter layers. The hourly wind reported within a layer closely approximates a true average, being composed of several six-minute time integrations of the backscattered radar energy from that volume. Radiosondes, however, report nearly instantaneous thermodynamic quantities at approximately 30-meter vertical intervals. Since a radiosonde flight takes 1-2 hours and the sensor typically drifts several tens of km during the flight, the vertical profile of a sounding is a collection of individual point measurements, each a function of latitude, longitude, elevation and time. The four dimensionality of a sounding is typically not a problem when considering data from the operational radiosonde network. With soundings at 12-hour intervals and separated by 400 km, 50-km drift over a couple of hours does not introduce significant error when considering the temporal and spatial scales that can be resolved by the conventional network (Sanders, 1988). However,

during the FIRE Cirrus-II field deployment, radiosonde sites in the Kansas-Oklahoma region were separated by less than half the normal spacing (Fig. 1) and the temporal resolution was enhanced much of the time (Starr, This Issue). Therefore, taking full advantage of the combined radiosonde and wind profiler networks requires a careful accounting of balloon drift and the temporal characteristics of the observations.

The temporal and vertical coordinates defined by the wind profiler observations are specified as the coordinate values to which the radiosonde data are interpolated. This choice is intuitive since enough information exists in each radiosonde sounding to unambiguously interpolate the data to any vertical coordinate; this is clearly not the case for the wind profilers. Additionally, regional kinematic analyses using the wind profiler data are possible at a much finer temporal resolution than from the radiosonde data. For consistency, therefore, physical height will be used as the vertical coordinate in this work.

So that the radiosonde and wind profiler data can be combined into a single diagnostic framework, the vertical resolution of the radiosonde data were coarsened and the soundings were temporally interpolated to approximate the vertical resolution and the nominal times of the wind profiler observations. The soundings were vertically averaged to the same 250 meter height increments as the wind profiler data using all available observations 125 m above and below each profiler data level. All data elements in the sounding were treated in this way including the latitudes, longitudes and times of each observation. After performing the vertical averaging on a time series of soundings from a particular observing site, the layer-mean time values were used to temporally interpolate the vertically averaged temperature, pressure, specific humidity,  $u$  and  $v$  wind components and latitude and longitude to the top of each hour to match the nominal valid times of the hourly wind profiler data.

This technique, which is similar to one described by Frankhauser (1969), accounts for the drift in the radiosonde during flight and for the time interval of the ascent. Thus, displacements of the sensors in both space and time are considered when performing spatial objective analysis of the data. The most obvious limitation is the temporal resolution of the soundings relative to the wind profiler observations. Therefore, in practice, diagnostics that require thermodynamic information will only be performed at the nominal sounding times. Also, only temporally enhanced sounding periods (3-6 hourly) are considered when temporal derivatives of the thermodynamic data are necessary. These processing techniques were applied to all radiosonde data collected during FIRE Cirrus-II.

## 2c. Spatial Objective Analysis of Wind Profiler and Radiosonde Data

After the initial processing steps have been completed, the wind and thermodynamic data tend to be randomly distributed over the analysis region. In principle it would be possible to perform spatial objective analysis using the function surface fitting techniques traditionally applied to data of these types: namely, to divide the analysis domain into data polygons, perform function surface fitting of low order polynomials to the polygon centroids and conduct a diagnostic analysis directly from the centroid-analyzed data fields (Zamora et al, 1987; Carlson and Forbes, 1988). As shown by Davies-Jones (1993), however, direct examination of the polygon centroid values tends to be most applicable to smaller data networks (from three to seven or so data points) that extend over limited geographical regions. When applied to extended arrays with a variable spatial distribution of data points, it becomes difficult to optimize the function surface fitting technique to reduce the uncertainty in observational and aliasing error at the polygon centroids. Furthermore, interpretation of the centroid results from several polygons is uncertain since polygons of varying spatial extent and geometry have different responses to observational error and to meteorological features below the resolution of the data network (Mace, 1994). Therefore, we choose a slightly more involved process that is designed to minimize the influence of observational and aliasing uncertainty.

Initially, the observations are mapped to a  $1^\circ$  latitude-longitude grid using the bivariate interpolation scheme described by Akima (1978, 1984). This algorithm uses the irregularly distributed data point positions to divide the analysis domain into triangular cells. A bivariate quintic polynomial is then fitted to these cells. Interpolation to the latitude-longitude grid is performed using a fifth-order polynomial with coefficients determined from the data triangles. Interpolation from the grid points back to the data points returns the input values to within machine precision. Accuracy away from the data points depends largely on the spatial density of the observations. Not surprisingly, spurious oscillations of the interpolated values are noted when the interpolation grid is much finer than the density of the observations. In order to avoid this undesirable characteristic, the diagnostic domain we consider for quantitative analysis is restricted to the region bounded by the wind profiler locations and enhanced (Fig. 1) radiosonde sites. However, all wind profiler and radiosonde sites available are used at each analysis time. In other words, each analysis encompasses most of the western two-thirds of the continental United States. Also, it should be noted here that the radiosonde-observed winds are not used in Kansas or Oklahoma. Inclusion of the radiosonde winds into the wind field analysis in this region caused sharp discontinuities in the time-series of kinematic quantities. This inconsistency is likely a reflection of the vastly different measurement strategies employed by wind profilers and in calculating horizontal winds from radiosondes. The wind profilers sample volumes of air in a height range as the

air passes over the instrument. Here we average these volume means for one hour. Radiosonde winds, on the other hand, are computed from a single horizontal displacement at a particular time. Radiosonde winds are, therefore, much more likely to contain components from much smaller scales of motion: scales that could not be resolved by the current observational network. These smaller-scale components are likely averaged out of the wind profiler winds. Therefore to maintain consistency in the analysis product, only the profiler winds are considered in the Kansas-Oklahoma region.

The interpolation scheme maps the observed fields exactly without consideration to objective analysis uncertainties. Therefore, the mapped fields are considered to be equivalent to the data in every way. By this it is meant that the observational quantities ( $u$ ,  $v$ ,  $T$ ,  $p$ ,  $q$ ) now distributed on the regular grid contain the desired large-scale atmospheric signal, as well as contributions from random observational error and from atmospheric signal of scale below the network's spatial resolution. Our analysis goal is to filter the data such that only the desired atmospheric signal remains. As shown by Thiebaut and Pedder (1987) and Davies-Jones (1993), this analysis goal can be addressed by using overdetermined low-order polynomials fitted to data in a least squares sense. Applying these techniques reduces the magnitude of objective analysis uncertainties in a predictable way. Assuming that the minimum length scale that can be resolved accurately by a network with 250 km spacing is about 2500 km, a spatial filter based on an overdetermined plane surface is applied to the gridded observations. The distribution of input data and an amplitude response curve of the spatial filter is shown in Fig. 2. The spatial resolution of the smoothed data fields tends to be 2 degrees latitude by 2 degrees longitude. The RMS uncertainty of the analyzed quantities is approximately  $\eta 5 \times 10^{-6}$  where  $\eta$  is the uncertainty in the observed quantity. By interpolating the filtered wind fields back to the wind profiler locations, the amount of smoothing can be examined. Shown in Fig. 3, the RMS difference of the smoothed to the original data is  $3.5 \text{ ms}^{-1}$ . While the accepted uncertainty in the wind profiler data is near  $2 \text{ ms}^{-1}$  the additional smoothing can be attributed to meteorological features below the specified resolution of the analysis grid.

### 3. Case Study: November 26, 1991

The region we will concentrate on for quantitative analysis is bounded by southern Nebraska, eastern Colorado, northern Texas, and western Missouri and Arkansas. This area, which encloses the densest network of wind profiler and radiosonde sites (Fig. 1), will be referred to as the analysis domain. Within this domain, the wind observations are supplied exclusively by the WPDN. Outside of this region, the radiosonde-derived winds are used in

the objective analysis scheme by are not displayed here or considered for quantitative application. We examine the period from 18 UTC 26 Nov. 1991 (26/12) to 00 UTC 27 Nov. 1991 (27/00). This period is chosen for several reasons. All radiosonde sites in the western two-thirds of the United States began a three hourly launch schedule at 26/12. This enhanced sounding period coincided with two distinct synoptic-scale upper tropospheric cloud systems west of the Mississippi, one of which propagated through the analysis domain and was sampled by surface-based instrumentation and research aircraft at Coffeyville.

### 3a. Synoptic Setting

The synoptic setting for this period is shown in Fig. 4a and b. A low-amplitude ridge-trough pattern was established over North America early on 26 November. Northwesterly flow in the upper troposphere ahead of the offshore ridge existed over the West Coast while a broad diffluent trough is analyzed in the central United States. A strong jet is embedded in the northwesterly flow over the western third of the United States. Speed maxima of more than  $60 \text{ ms}^{-1}$  were observed by radiosondes in southwestern Wyoming and the Pacific Northwest. In the Kansas-Oklahoma region, wind speeds decreased substantially compared to the West and the flow became diffluent in the upper troposphere. At the surface, the western United States was dominated by a region of high pressure under the broad upper level ridge while low pressure and an associated frontal system were situated in the central United States. The analysis area was influenced by a broad southerly flow east of the surface trough. The southerly flow extended from the Gulf of Mexico into southern Canada.

By 27/00 a general amplification of the long-wave pattern is noted. Heights were rising over the Rocky Mountain states at 300 mb (Fig. 4c) while height falls occurred over the Pacific coast and central United States. A low-amplitude trough is evident at 300 mb extending from the western Gulf of Mexico into southern Canada. The northwesterly jet had become firmly established in the region of rising heights over the Rocky Mountain states. The exit region of the jet had propagated into the analysis domain and a strong wind speed gradient existed from east Texas northward to the Dakotas. At the surface (Fig. 4d), the low in the north-central United States and the associated frontal system had propagated eastward and deepened slightly.

Fig. 5 shows GOES infrared (IR) imagery for this period. While cold cloud tops denoting optically thick cirrus cover much of the western one-half of the United States, two identifiable broad-scale features can be identified. The eastern-most of these is oriented perpendicular to the upper tropospheric flow and extends through central Oklahoma and into

central and eastern Kansas. The east-west scale of this system increases considerably in the northern Plains and extends from central Nebraska to the western Great Lakes. This system bears a resemblance (at least in its southern portions) to a baroclinic leaf cirrus system (Weldon, 1979; Starr and Wylie, 1990). This system appears to be correlated with the deepening surface low and amplifying upper tropospheric disturbance identified above. Cirrus westward of the Rocky Mountains, on the other hand, is associated with the amplifying upper-tropospheric ridge. Cloud patterns here suggest an along-stream orientation with optically thick cirrus occurring near the ridge axis and progressively thinner and more patchy clouds extending to the flow inflection downstream of the ridge axis. This large-scale cloud pattern is readily classified as a ridge-crest cirrus system in accordance with Starr and Wylie (1990).

### 3b Kinematic Analysis

The 10 km profiler-derived wind field in the analysis region at 26/18 and 27/00 is shown in Fig. 6. This height corresponds to the level of maximum wind speed in the northwesterly jet. The strong speed gradient associated with the exit region of the northwesterly jet is quite evident. A well-defined minimum in horizontal wind speeds can be seen in association with the trough axis that extended through central Oklahoma and Kansas at this time. By 27/00, the main features in the wind field at 10 km had propagated eastward at approximately  $12 \text{ m s}^{-1}$  (Fig. 6b). The region of sharpest cyclonic turning in the wind field is now analyzed in extreme western Missouri and Arkansas. The jet axis is now clearly identifiable extending through Colorado into the Panhandle Region of Oklahoma. The intense isotach gradient between the jet core and trough axis is squarely within the wind profiler network at this time. It is quite evident that air exiting the jet core in western Oklahoma experienced rapid deceleration as it flowed southeastward toward the trough axis.

The horizontal divergence and relative vorticity at 10 km are shown in Fig. 7. At 26/18, a maximum in positive vorticity is located over the panhandle of Oklahoma with positive values extending eastward to western Missouri and Arkansas. The trough axis that was situated in eastern Oklahoma at 26/18 (Fig. 6b) is not clearly delineated in the vorticity field. The observed vorticity over Oklahoma and Kansas will be shown to be due to horizontal speed shear associated with the jet and cyclonic turning in the low amplitude trough. By 27/00, however, the north-south oriented axis of positive vorticity (Fig. 7d) is more clearly aligned with the trough axis identifiable in the wind field (Fig. 6b). Values near the trough axis have increased during the previous six hours. This is indicative of an overall amplification of the upper tropospheric wave pattern.

The horizontal divergence at 10 km is also closely coupled to the advancing jet streak and to the short-wave trough. At 26/18, an axis of positive horizontal divergence was oriented through central Oklahoma west of the trough axis and east of the maximum wind speed gradient (Fig. 7a). Convergence was diagnosed in the speed gradient from the panhandle region, northward. At 27/00 (Fig. 7c), the southern portion of the divergence axis at 10 km had shifted eastward with the propagating and evolving wind field while the more northerly portions had remained stationary. This is consistent with the jet core advancing into Oklahoma and the trough axis moving eastward. Also, the maximum in horizontal divergence along this axis had shifted northward at 27/00 although the central Oklahoma maximum at 26/18 had moved beyond the coverage of the WPDN. An axis of horizontal convergence becomes identifiable at 27/00 aligned along the northwesterly jet core (Fig. 6b) through Colorado and into the Oklahoma Panhandle. A maximum in horizontal convergence occurs in the jet core over the Red River.

Since the horizontal divergence plays such a key role in determining ageostrophic motions and vertical velocity, it is instructive to examine the contributions of the individual components of this quantity. Using a natural coordinate system oriented with the wind flow, the horizontal divergence can be written

$$Div = \frac{\partial U}{\partial s} - U \frac{\partial \beta}{\partial n} + \frac{U}{R_t} \quad (1)$$

Where  $U$  is the horizontal wind speed,  $s$  is directed along the observed airflow,  $n$  is directed to the right of the motion,  $\beta$  is the wind direction and  $R_t$  is the radius of trajectory curvature. The first term on the right of Eqn. 1 accounts for the divergence of air parcels along the direction of motion, the second term quantifies the diffluence of streamlines and the third term is due to advection of trajectory curvature by the mean wind. Following Cammas and Ramond (1989), the along- and cross-stream gradients are calculated, where:

$$\frac{\partial}{\partial s} = \hat{s} \cdot \nabla = \frac{1}{U} \bar{V} \cdot \nabla = \frac{1}{U} \left( u \frac{\partial}{\partial x} + v \frac{\partial}{\partial y} \right)$$

$$\frac{\partial}{\partial n} = \hat{n} \cdot \nabla = \frac{1}{U} \nabla \cdot (\hat{k} \times \bar{V}) = \frac{1}{U} \left( -v \frac{\partial}{\partial x} + u \frac{\partial}{\partial y} \right).$$

The curvature advection term in Eqn. 1 is determined as a residual by differencing the Cartesian coordinate representation of the horizontal divergence and the sum of the speed divergence and directional diffluence terms. For the case considered here, the contribution to

the horizontal divergence by the curvature advection remained at least a factor of five smaller than the sum of the first two terms on the right of Eqn. 1.

The contribution of the natural coordinate components of the horizontal divergence at 10 km is shown in Fig. 8. A large degree of cancellation can be seen between the speed and directional diffluence terms. The directional diffluence, however, did tend to be slightly more positive (Fig. 8b) than the speed diffluence was negative (Fig. 8a) in central and eastern Oklahoma at 26/18. Not unexpectedly, the speed diffluence was negative or convergent in the exit region of the strong jet while directional diffluence was positive ahead of the speed gradient. The cancellation vanished, however, ahead of the speed gradient in eastern Oklahoma at 26/18 where the speed diffluence was weakly positive while the directional diffluence in the trough resulted in positive values of the total horizontal divergence. The contribution due to curvature advection was positive in the region of cyclonic turning (Fig. 8c) although the magnitudes tended to be much smaller. Interestingly, the axis of the divergent contribution due to curvature advection is displaced west of the trough axis. This displacement is due to the lower relative wind speeds in the trough axis. While the maximum cyclonic curvature was in eastern Oklahoma (roughly parallel to the  $1 \times 10^{-6} \text{s}^{-1}$  isopleth in Fig. 8c), the wind speeds and curvature correlated most positively approximately 200 km west of the trough axis.

The changes in the natural coordinate contributions to the horizontal divergence between 26/18 and 27/00 are consistent with the eastward propagation of the wind field. Since the exit region of the jet is more squarely within the profiler array at 27/00, the resolution of the divergence components is more certain. Directional diffluence tends to remain dominant in eastern Oklahoma while a region of directional confluence is resolved extending from western Oklahoma into northeastern Colorado. The axis of speed confluence now extends northward from south-central Oklahoma and curves northeastward along the wind speed gradient west of the trough axis. While the trough remains evident in southwestern Missouri and northwestern Arkansas in the curvature term, the primary contribution over the analysis region is convergent owing to anticyclonic curvature in the wind speed gradient.

The ageostrophic winds were estimated using the horizontal momentum equations after Zamora et al. (1987):



$$\frac{dv}{dt} = \left( \frac{\partial}{\partial t} + u \frac{\partial}{\partial x} + v \frac{\partial}{\partial y} + w \frac{\partial}{\partial z} \right) v = -f u_a$$

$$\frac{du}{dt} = \left( \frac{\partial}{\partial t} + u \frac{\partial}{\partial x} + v \frac{\partial}{\partial y} + w \frac{\partial}{\partial z} \right) u = f v_a$$

where  $u_a$  and  $v_a$  are the eastward and northward components of the ageostrophic wind, respectively and  $w$  is the vertical motion calculated using the kinematic method described in Appendix B. Time derivatives were estimated using centered differencing. Uncertainties in the kinematic vertical velocity are discussed in appendix B; however, we assume an overall uncertainty of  $2 \text{ cm s}^{-1}$  in this term. The ageostrophic components will be most influenced by this uncertainty in regions of strong vertical shear where the horizontal gradient of  $u$  and  $v$  are small (*e.g.*, below the level of maximum wind along the jet axis). If we assume a vertical shear of  $10 \text{ m s}^{-1} \text{ km}^{-1}$  in a horizontal wind component and an uncertainty of  $2 \text{ cm s}^{-1}$  in the vertical velocity, this translates to an uncertainty in the ageostrophic wind speed of about  $2 \text{ m s}^{-1}$ .

In order to further delineate between the components of the ageostrophic wind in the along- and cross-stream directions, consider the natural coordinate components of the ageostrophic wind in a frictionless atmosphere (Cammis and Ramond, 1989),

$$V_{an} = + \frac{1}{f} \frac{dU}{dt}$$

$$V_{as} = - \frac{1}{f} \frac{U^2}{R_t}$$

where  $V_{an}$  and  $V_{as}$  are the cross and along-stream components of the ageostrophic wind, respectively. It can be seen that the cross-stream ageostrophic wind is due primarily to along-stream accelerations of air parcels while ageostrophic motions along the airstream arise from centripetal accelerations on curved trajectories.

The ageostrophic winds and their associated natural coordinate components at 10 km are shown in Fig. 9. The influence of the trough and the jet exit region are the dominant factors at this level. While  $V_{an}$  nearly vanishes near the trough axis in eastern Oklahoma and Kansas, the influence of the jet exit region is evident (to a greater extent at 27/00) with ageostrophic flow to the right of the wind indicative of the deceleration of air parcels as they pass from the jet core into regions of weaker pressure gradient. This pattern of  $V_{an}$  also suggests a transverse ageostrophic circulation that is thermally indirect in the jet exit. This

will be considered in more detail below. While the transverse ageostrophic flow is negligible near the trough axis, the observed winds are subgeostrophic here, as expected, at 26/18 and 27/00. This can be seen by examining the  $\mathcal{V}_{as}$  field. At 26/18, the trough axis (Fig. 6a) is not clearly identifiable in the  $\mathcal{V}_{as}$  field, although the region of negative  $\mathcal{V}_{as}$  in Oklahoma and Kansas correlates well with the rather broad region of cyclonic turning seen in the wind field. By 27/00, subgeostrophic flow is concentrated along the trough axis delineated by the region of negative  $\mathcal{V}_{as}$  in eastern Oklahoma and Kansas and western Missouri and Arkansas. The alignment of the subgeostrophic flow regime along the trough axis and the apparent increase in magnitude of negative  $\mathcal{V}_{as}$  support the hypothesis that the flow was amplifying during this period. Also at 27/00, large positive values of  $\mathcal{V}_{as}$  are resolved over much of the western portion of the analysis region. Positive values of  $\mathcal{V}_{as}$  indicate that air parcels in this region are following anticyclonic trajectories. This hypothesis can be examined by considering the curvature contribution to the relative vorticity at 27/00. Shown in Fig. 10, these values were calculated as a residual by differencing the shear vorticity and total Cartesian representation of the relative vorticity. The streamline curvature in the western portions of the analysis region was clearly negative. When anticyclonic streamlines move eastward at phase speeds slower than the wind speed, the resulting radii of trajectory curvature tend to be less negative than the streamline curvature since parcels are moving through the advancing streamline pattern (Holton, 1979). While the eastward progression of the anticyclonically curved exit region would have resulted in less negative values of the trajectory curvature, the relatively slow phase speed of the pattern relative to the airflow would still lead to a negative trajectory curvature and positive along-stream ageostrophic flow in this region.

The diagnostic framework provided by the natural coordinate representation of the ageostrophic winds aids in an understanding of the pattern of upper tropospheric divergence shown in Fig. 7. Consider the ageostrophic wind vectors and speeds at 27/00 (Fig. 9d). An axis of horizontal convergence is suggested extending from south-central Kansas to north-central Texas. This feature is also evident at 26/21 (not shown) where it extended in a north-south direction from western Kansas through the Texas panhandle. Since the geostrophic winds are approximately non-divergent, the horizontal divergence is closely coupled to the ageostrophic wind. It is not surprising, then, to find a close correspondence between the convergence resolved from the total wind field and the axis of convergence in the ageostrophic winds in this region. The convergence in western Oklahoma was induced by a superposition of the ageostrophic flow near the trough east of the convergence axis, the transverse ageostrophic flow associated with the jet exit and the ageostrophic wind induced by the anticyclonic parcel trajectories in the western portion of the analysis region.

The transverse ageostrophic flow and horizontal divergence pattern at 10 km suggest a thermally indirect circulation across the jet exit region. The vertical cross section of the horizontal wind at 26/21 through the analysis domain is shown in Fig. 11a. The jet streak is evident in the southern half of the cross section with a strong vertical shear between 7 and 10 km. The cross-stream ageostrophic winds (Fig. 11b), as expected, reach maximum magnitudes in excess of  $30 \text{ m s}^{-1}$  in the jet portion of the cross section and become positive (to the left of the flow) in the middle and lower troposphere. The vertical motions in the plane of the cross section (Fig. 11c) show ascent, maximizing in the middle troposphere at just over  $3 \text{ cm s}^{-1}$ , across the northern half of the cross section under the upper divergence discussed above. Descent is diagnosed further south under the elevated convergence region. Combining these two terms into a vector quantity yield a qualitative image of the transverse ageostrophic circulation (Fig. 11d). Overlaid on the potential temperature pattern, we find ascent in the relatively colder air north of the jet axis while the warmer air beneath the jet core is descending. In other words, we diagnose a thermally indirect transverse circulation centered near 5 km. The horizontal gradient of the vertical motion is clearly frontogenetical with vertical gradients in potential temperature being tilted into the horizontal plane.

An interesting characteristic of the transverse ageostrophic circulation diagnosed late on 26 November is the placement of the circulation to the cyclonic side of the jet axis. While a thermally indirect transverse circulation is expected in the exit region of a jet streak (Keyser and Shapiro, 1986), the circulation cell would tend to be centered on the jet axis in the absence of thermal advection. The orientation diagnosed here places subsident vertical motions beneath the advancing jet core. Unfortunately, the anticyclonic shear side of the jet was not sampled by the profiler array during this time. We are, therefore, unable to determine what the characteristics of the vertical motions were to the right of the jet axis. However, by building on the previous discussion of the kinematic characteristics of the upper troposphere, understanding the orientation of the ageostrophic circulation in the left exit region is straightforward. The displacement of the indirect circulation resulted from the juxtaposition of the diffluent trough axis in the northeast of the analysis domain, the jet exit region and the anticyclonic curvature in the west. The upper tropospheric divergence in the region of directional diffluence and small but positive curvature divergence coupled with lower tropospheric convergence associated with the weak front and developing low pressure forced the ascending branch of the circulation. While the influence of streamline curvature on the horizontal divergence was small in the northeast areas, the westerly ageostrophic motions that resulted from the positive curvature (Fig. 9) contributed to the development of upper tropospheric convergence west of the trough axis (Fig. 7). This convergence was strengthened by a confluence of the northeasterly ageostrophic flow in the jet exit region

(caused by along-stream parcel decelerations, Fig. 9) and the positive along-stream ageostrophic flow associated with anticyclonic trajectories (Fig. 10) beneath the jet core. This resulted in strong upper tropospheric convergence over western Oklahoma and Kansas forcing the diagnosed descent in this region.

An alternate interpretation of the forcing of the ageostrophic circulation can be obtained by considering the geostrophic forcing of the Sawyer-Eliassen equation. Provided that the potential vorticity is everywhere positive, this equation is a second order elliptic partial differential equation that diagnoses an ageostrophic streamfunction required to maintain thermal wind balance in straight jet-front systems (Keyser and Shapiro, 1986). Symbolically and qualitatively we can write,

$$\omega \propto \frac{\partial v_g}{\partial y} \frac{\partial \theta}{\partial y} + \frac{\partial u_g}{\partial y} \frac{\partial \theta}{\partial x} = Q_1 + Q_2$$

where  $\omega$  is the circulation streamfunction,  $u_g$  and  $v_g$  are the geostrophic components in the along front (parallel to  $x$ ) and cross front (parallel to  $y$ ) directions and  $x$  and  $y$  are oriented along and across the upper level jet-front system respectively.  $Q_1$  is the geostrophic stretching deformation and quantifies the effect of geostrophic confluence forcing scale contractions on the frontal temperature gradient.  $Q_2$  accounts for horizontal geostrophic shear rotating along front thermal gradients into the cross front direction. A schematic representation is shown in Fig. 12. While there are inherent difficulties in a quantitative application of this equation to data (Cammis and Ramond, 1989), without excessive flow curvature, the diagnosed vertical circulation should agree qualitatively with the geostrophic forcing.

The Sawyer-Eliassen forcing,  $Q_1$  and  $Q_2$ , in the plane of the cross section of Fig. 11 are displayed in Fig. 13. The total geostrophic forcing of the transverse circulation is negative and would, therefore, tend to force a thermally indirect circulation. The total forcing reaches a maximum near 9.0 km over central Oklahoma. The location of the maximum forcing coincides with the diagnosed center of circulation (Fig. 11c) although the forcing maximum is displaced several km above the circulation center. By examining the components of the geostrophic forcing, we find that the geostrophic confluence,  $Q_1$ , is the dominant term. The dominance is due, in large part, to very small magnitudes of  $\partial u_g / \partial n$  in the cross section. While considerable warm air advection is diagnosed (strongest warm air advection is found near the diffluent trough), the small cross-stream shear in  $u_g$  would have little effect in rotating the thermal gradient into the cross-stream direction. As expected from thermal wind arguments, the cross-stream thermal gradients are maximized just below the jet core in the extreme southwestern portion of the cross section. However, due to a decrease in

the magnitude of the horizontal confluence in the geostrophic wind in this region  $Q_1$  reaches maximum magnitudes northeast of the jet core on the cyclonic side.

The important point here is that the kinematically-derived ageostrophic circulation agrees qualitatively with the total geostrophic forcing. We have found that this forcing is generated predominantly by a frontogenetical amplification of the cross-stream temperature gradients by the geostrophic wind. Recall Fig. 11d that shows the vertical gradient of potential temperature being tilted into the horizontal plane by the thermally indirect vertical circulation.

### 3c The Cloud Event of November 26: Regional and Local Description

The analysis of the objectively analyzed radiosonde and wind profiler data has enabled us to infer the dynamical characteristics of the large scale flow during this period. However, our primary goal is to understand how the cloud fields (cirrus, in particular) evolved in concert with the dynamics. Indeed, it is this connection between the large-scale characteristics and the macroscopic properties of the resulting clouds that will ultimately be combined with the observed microphysical and radiative characteristics to yield improved parameterizations of cloud occurrence and optical properties in GCMs.

Consider again the GOES satellite imagery (Fig. 5) of the cloud band as it progressed over central and eastern Kansas and Oklahoma from 26/18-27/00. At 26/18, the cloud system appeared as a linear feature oriented approximately south to north from central Texas through Oklahoma and into eastern Kansas where the system broadened into a fairly extensive cloud system centered on Iowa. In north Texas, the band appears to be composed primarily of middle-level clouds while the clouds become progressively brighter and more cirriform in nature from central Oklahoma, northward. The horizontal width of the band increases from approximately 100 km in central Oklahoma to more than 250 km in northeast Kansas. It is important to note here that this particular cirrus system cannot be classified as a typical jet-stream cirrus event where cirrus is often observed to be elongated parallel to the wind flow. The upper tropospheric flow here is generally perpendicular to the orientation of the cloud field and the system propagates roughly at the phase speed of the dynamical pattern. East of the cloud band in Texas, Oklahoma and Arkansas, low and middle-level clouds with some cirrus was associated with a developing southerly flow from the Gulf of Mexico. Skies cleared considerably in western Kansas and the panhandle region of Oklahoma and Texas.

The high cloud optical depths calculated using visible GOES 7 data and the technique of Minnis et al. (1993) are shown in Fig. 14. Optically thin cirrus is diagnosed along much

of the band through central Oklahoma. Optical depths increase substantially in southern Kansas. It is noteworthy that a simple examination of the IR imagery does not suggest a large change in the character of the cloud band in south-central Kansas. While some variability in the brightness is evident, no large changes occur in the IR from central Oklahoma into northern Kansas. However, at visible wavelengths, the southwest-northeast oriented spur of cirrus in south-central Kansas identifiable in the infrared imagery represents the southern extent of the optically thickest cloud line. We speculate that these characteristics are evidence of the well-known property of thin cirrus that the infrared emissivity approaches unity more rapidly than the visible reflectivity (Ackerman et al., 1988).

By 26/21, the entire cloud structure had progressed eastward. The leading edge of the main cloud band in the infrared imagery is identified in eastern Texas and Oklahoma. Evaluation of the satellite-derived visible optical depths are not possible at 26/21 due to increasing solar zenith angles. Farther north in northeastern Oklahoma and southeast Kansas, a series of three southwest-northeast oriented cloud lines are identified. Animation of the imagery suggests that these lines were becoming increasingly brighter with time, indicating active cirrus generation, and propagating southeastward toward the leading edge of the primary cloud system. Apparently, cloud generation was occurring in a wave-like pattern oriented nearly parallel to the weak southwesterly flow aloft. The southwestern portion of these active generation regions tended to be advected faster toward the east by the advancing jet streak (Fig. 6) than the northeastern segments. This resulted in the north-south orientation of the cloud line in the infrared imagery. This is particularly evident between 26/21 and 27/00. Fig. 15 shows the brightest band as it passed through southeast Kansas between 26/21 and 27/00. The initial southwest-northeast orientation at 26/21 gradually became more north-south as the southern portions were more rapidly advected eastward relative to the northern parts.

By 27/00, the leading edge of the main cloud band had passed eastward into Arkansas and Missouri. The trailing portions of the band are identified over southeastern Kansas and eastern Oklahoma. The region of clear skies had also progressed eastward into central Oklahoma and Kansas while cirrus can be identified in the northwesterly flow over Colorado, western Kansas and Oklahoma in association with the ridge-crest cirrus system identified earlier.

The broad characteristics of the cloud field that passed over Kansas and Oklahoma are strongly coupled to the synoptic-scale dynamics discussed above. During its passage through the analysis region, the cloud band existed *between* the wind speed gradient associated with the advancing jet streak and the diffluent trough axis to the east. The cloud

band propagated eastward with these dynamical structures and maintained its overall orientation with them throughout the period. This correspondence can be understood by considering the horizontal divergence in the upper troposphere (Fig. 7). At 26/18, the cloud band can be seen to extend along the axis of horizontal divergence through central Oklahoma and Kansas. The placement of the horizontal divergence west of the trough axis and east of the speed gradient was discussed earlier. The coupling between the cloud and upper tropospheric divergence remained strong at 27/00 (Fig 6b) where the axis of horizontal divergence existed along the Kansas-Oklahoma border. At this time, the maximum divergence had shifted north into eastern Kansas. Satellite imagery suggests the brightest clouds at 27/00 were north of the Kansas-Oklahoma border with dissipating cloud cover over eastern Oklahoma where upper tropospheric divergence had decreased.

Of course, any correspondence of the cloud features with the horizontal divergence pattern in the upper troposphere follows directly from the vertical motions implied by mass continuity. Fig. 16 shows a time sequence of kinematic vertical velocity cross sections that transect the cloud band along the Kansas-Oklahoma border. As expected, large scale ascent is diagnosed in the middle and upper troposphere during this period. Broad gentle descent is also resolved in the lower stratosphere (the tropopause during this period was near 10.5 km). At 26/18, ascent is diagnosed between 2 and 8.5 km along the entire cross section with maximum vertical velocities of just over  $3 \text{ cm s}^{-1}$  occurring along  $97.5^\circ \text{ W}$  - the approximate location of the cloud band identified in Fig. 5a. Values greater than  $2 \text{ cm s}^{-1}$  are estimated to extend to 7.5 km at this time. By 26/21, the vertical motion pattern along the cross section had shifted eastward and intensified significantly. Maximum ascent is still resolved near 4.5 km with peak values greater than  $5 \text{ cm s}^{-1}$  along  $95\text{-}96^\circ \text{ W}$ . Positive vertical motions are also resolved to a higher elevation at 26/21 with values greater than  $2 \text{ cm s}^{-1}$  occurring to 8 km and positive vertical motions suggested to 11 km. Recall that during this period, active cirrus cloud formation was occurring in bands near the Kansas-Oklahoma border. These bands were propagating southeastward towards the leading edge of the main cloud formation. The cross section of vertical motions along the central portion of the main cloud shield at 26/21 is shown in Fig. 17. As before, peak upward motions are resolved in the middle troposphere near  $37^\circ \text{ N}$  just south of the Kansas-Oklahoma border. The upper troposphere near this latitude is ascending while upper tropospheric subsidence is diagnosed north and south of the cirrus generation area. Also, as suggested by imagery, the vertical motions throughout the troposphere decrease markedly in central and southern Oklahoma. By 27/00 (Fig. 16c), the region of maximum ascent had shifted eastward into southwest Missouri and subsidence is resolved west of  $98^\circ \text{ W}$  in all but a thin tropospheric layer between 9 and 12 km. The positive vertical motions are consistent with cirrus advancing into the western

portion of the area in association with the approaching large-scale ridge-crest cloud system. The trailing edge of the cloud band under consideration now existed over extreme eastern Kansas and Oklahoma.

Fortuitously, the Hub of the FIRE CIRRUS-II project at Coffeyville, Kansas (Fig. 1) was located very near the maximum large scale vertical motions and most intense cirrus generating region. This allowed extensive sampling of the characteristics of the clouds forced by the vertical motions described above. Fig. 18 shows a time-series of the data collected by The Pennsylvania State University 94 GHz cloud radar (Clothiaux et al., 1994) on the afternoon of 26 Nov. The leading edge of the cloud shield was first observed over Coffeyville at about 9 km. The layer of cirrus rapidly thickened after 1900 UTC, resulting in a cloud layer with a base at about 6.5 km and top ranging from 8.8 to 9.5 km. Aircraft reports indicate very thin cirrus extended up to about 10.5 km. The radar profile shows regions of enhanced power after 1915 UTC indicative of convective cells within the main cloud layer. Three organized precipitation streamers that penetrated below 6 km occurred between 1945 and 2115 as cloud base gradually lowered (Fig. 18). After 2115, a definite change in the character of the cloud was noted as cloud base lowered quite rapidly and returned power increased. By 2200 UTC cloud base was observed near 3 kilometers. (Note that the radar minimum range was set at 3 km during this period, which precluded measurements below this height; cloud base did drop below 3 km as evidenced by ceilometer measurements.) Cloud top during this time was observed to decrease slightly to 8 km. The next major change in the cloud deck occurred after 2215 UTC. Cloud top and the upper extent of the region of enhanced reflectivity became more diffuse and cloud top began to decrease rapidly while the lower portions remained nearly unchanged. By 2330 UTC only scattered clouds were observed by the radar.

The local evolution of the vertical thermodynamic and moisture structure is of considerable importance when attempting to understand the coupling between the diagnosed dynamics and the observed local and regional cloud fields. We will consider the CLASS radiosonde soundings (see Fig. 1) recorded at Coffeyville, Iola (IOL), Arkansas City (ARK) and Muskogee (MUS) at 26/12, 26/15, 26/18, 26/21 and 27/00. Relative to Coffeyville, ARK is about 140 km to the west, IOL about 100 km to the north and MUS about 160 km to the south. Also recall that the actual release times of the soundings are 30-45 minutes prior to the nominal sounding time and that the sondes reached 8 km about 25 minutes after launch. The time series of soundings for Coffeyville are shown in Fig. 19 where each successive sounding is offset by 10 °C. Fig. 20 shows time-height cross sections of relative humidity and plotted in Fig. 21 are time series of potential temperature profiles.



The tropopause at Coffeyville was located at about 10.5 km (245 mb at  $-59.5^{\circ}\text{C}$ ) at 26/15 and slightly lower at 26/18 and 26/21 (Fig. 19). A much lower tropopause (9.4 km at 290 mb and  $-51.1^{\circ}\text{C}$ ) was observed at 27/00 although the region between 9.8 and 10.7 does have a tropospheric lapse rate at this time with relative humidity (ice) greater than 60%. Recall that this last sounding passed through the most vertically developed portion of the cirrus cloud band. Complex upper tropospheric stability structure (multiple tropopause) is common in soundings taken in the vicinity of jet cores (*e.g.*, Starr and Wylie, 1990). The ARK soundings show a similar pattern with continued tropopause lowering and complex structure after the cloud band had passed while IOL and MUS show less dramatic changes (Fig. 21). The general tendency is consistent with the diagnosed weakly subsident vertical motions in the lower stratosphere (Fig. 16).

The soundings generally exhibit a remarkable degree of thermal structure with a number of persistent and highly stable features (Fig. 21). Each location has a strong inversion at about the 2 km level that does not appear to change with time. Each also shows a second inversion that initially occurred at about the 3 km level (26/12) but then subsequently lifted (especially after 26/18) before becoming fairly diffuse by 27/00 at Coffeyville and IOL where intense moistening and cloud development occurred below the 6 km level. By 27/00, this feature was located just below the 5 km level at ARK. Another less distinct but persistent stable feature was also initially observed just above the 6 km level at each site. This stable zone tended to lift weakly until 26/21 at Coffeyville and IOL followed by a dramatic rise. This feature has good correspondence with cloud base between 26/19 and 26/21 at Coffeyville and caps the region of very dry air below the region of initial cloud formation (Fig. 20). The observed vertical displacements of the mid-tropospheric stable features (and isentropes) is in very good agreement with the diagnosed pattern of vertical motion both temporally and spatially.

Warm air advection was observed at Coffeyville throughout the upper troposphere above 7 km in association with the progressive humidification of the region. However, strong cooling was observed between 26/21 and 27/00 (Fig. 21). Similar tendencies were observed at the other sites although differences are seen in the lower extent of the region of warm advection and in the timing of the changeover to cold advection. It is likely that the changeover from warm to cold advection roughly coincided with the dissipation of the upper portion of the cirrus band observed after 2245 at Coffeyville (Fig. 18) though this cannot be definitively established with the available data. The passage of the bright southwest-northeast cirrus band at IOL (Fig. 5b) also corresponds fairly well with the changeover there.

The thermal structure associated with this event showed a good deal of variability and complex development. The evolution of the moisture field as observed by the CLASS

radiosondes also exhibits quite interesting evolution. The 26/15 and 26/18 soundings from Coffeyville (Fig. 19) show a layer of enhanced moisture (60% or greater) at an altitude of 7 km with very dry air above and below this layer (Fig. 20). The 26/18 sounding was made in the cloud-free dry slot just ahead of the cloud band (Fig. 15). By 26/21, relative humidity exceeded 80% in layers located at 7 and 8.8 km. The latter corresponds fairly well to the location of cirrus cloud top while the former corresponds to the layer where cloud development was observed after 26/19 (Fig. 18). Later at 27/00, relative humidity exceeded 100 % in the lower layer that had merged with the upper moist layer. Very strong moistening had occurred between 3 and 6 km in agreement with the radar cloud observations at 26/23 and the calculated vertical motion forcing (Fig. 14). Enhanced humidity is found up to nearly 11 km. This sounding passed through the cloud system at its most vertically developed stage (Fig. 18).

Soundings made to the north at IOL show similar moisture structure (Fig. 20) although the humidification above the 8 km level was observed earlier (26/15). This is consistent with the satellite imagery that indicates a much broader region of cirrus cloud development to the north of Coffeyville. The relative humidity patterns at Coffeyville and IOL are remarkably similar at lower levels. The evolution of the moisture field to the west at ARK shows a less intense pattern of moistening. The final 27/00 sounding at ARK was made in the clear region following the cloud band (Fig. 5c) and indicates substantial drying of the upper troposphere. Besides resolving the main cirrus deck between 6 and 9 km, the 26/21 ARK sounding also gives some indication of another layer of possible cloud formation near the 10 km level that is consistent with observations from one of the research aircraft (M. Poellot, personal communication). It also appears that the downward extension of the cloud layer that was observed at Coffeyville after 26/2145 (Fig. 18) had probably not developed by the time the cloud band passed ARK. Soundings made to the south of MUS (Fig. 20) show elevated moist layers at higher altitudes (8 and 9.5 km) that were somewhat more distinct (e.g., at 26/21). As at ARK, the intense moistening below the 6 km level was not observed at MUS.

From our earlier discussions, it is quite apparent that rather intense large scale ascent existed over southeastern Kansas and northeastern Oklahoma as the synoptic scale dynamics evolved during the afternoon 26 Nov. Evidence for this ascent was also noted in the radiosonde time series discussed above. A time-height cross section of kinematically-derived vertical motions using WPDN data and interpolated to Coffeyville is shown in Fig. 22. As expected, ascent is diagnosed below 8 km throughout the period and vertical motions near zero are diagnosed at and above the tropopause. Peak ascent remains in the layer between 3 and 4 km. The vertical velocity in the cirrus generating region between 6 and 8 km and

26/19 and 26/21 is between 2 and 4 cm s<sup>-1</sup>. At 26/22, when cloud base decreased to less than 3 km, maximum vertical velocities were near 7 cm s<sup>-1</sup> at 3.5 km. After 26/23, the uplift decreases substantially throughout the troposphere, in reasonable correspondence with the change from warm to cold advection. This decrease in the vertical forcing also correlates well with the passage of the trailing edge of the main cloud band to the east of Coffeyville depicted on satellite imagery and in the radar time series.

Thus, the layer of initial cloud formation (7 to 9 km, Fig. 18) was a region of warm advection and progressive moistening in association with upward vertical motions. This region was bounded below by a stable frontal-like feature that progressively lifted. Two pre-existing sublayers of enhanced moisture appear to have resulted in initial cloud generation at the 9 km level and then subsequent cloud generation at about the 7 km level in response to the continued forcing as well as possibly the moistening due to evaporation of ice crystals sedimenting from the higher layer. These two layers quickly merged. At 26/18 just prior to cloud formation, the thermal stratification in the layer from about 7 to 8 km was approximately neutral with respect to ice pseudoadiabatic processes with distinct sublayers exhibiting conditional instability. By 26/21, this region of weak instability was located about 0.5 km higher in correspondence with the lifting of the bounding stable layer below. This corresponds well with the radar observations of cellular, i.e., convective, development in the cloud layer and the initial visual observations of cirrus generating cells. Layers of conditional instability were also observed at higher levels at 26/18; however, the general tendency was for progressive stabilization there, especially after 26/21.

The subsequent, rapid, downward growth of the cloud layer after 26/2130 at Coffeyville was associated with a very rapid moistening of the layer between 3 km and the base of the existing cirrus clouds. This moistening likely resulted from quasi-horizontal advection but was also forced by the adiabatic cooling arising from the peak in upward motion in this layer and evaporation of falling ice crystals. The region between the two stable zones, approximately from 4 to 6 km at 26/18, was quite conditionally unstable. The stability structure became highly variable by 26/21 but still with evidence of good convective potential. Even at 27/00, strong conditional instability was still observed between 3 and 4.5 km. The progressive lowering of the zone of conditional instability is consistent with the interpretation offered by Starr and Wylie (1990) based on the numerical simulations by Starr and Cox (1985a and 1985b) where evaporation of falling ice crystals leads to downward propagation of convective cloud generating layer through the combined effects of evaporative moistening and the destabilizing pattern of corresponding evaporative cooling. In the present case, we speculate that penetrative downdrafts could have developed in association with precipitation streamers falling into this conditionally unstable layer as

relative humidity approached ice saturation and led to the rapid downward growth seen in Fig. 18.

#### 4. Cirrus Parameterization

The analyses presented in the preceding section have provided a time series of vertical velocity and relative humidity averaged over spatial scales of several hundred kilometers and centered on the FIRE Cirrus II operational hub at Coffeyville. We believe that these fields provide an accurate description of the synoptic scale conditions at Coffeyville, unfiltered by any model assimilation. As such, these fields represent a purely data-based analogue to the fields generated by GCMs. The two primary differences are that these data fields represent a directly observable atmospheric state (as opposed to GCM fields, which represent some particular realization of the model climatology) and their time resolution is somewhat coarser than that of a GCM. Given that these fields are analogous to GCM fields, they can be used to drive a cloud parameterization just as the parameterizations are driven in an actual model (Jacobellis and Sommerville, 1991). Because observations of cloud properties were made during this period at the Coffeyville site, we have the unique opportunity to validate the clouds generated by the parameterization scheme. As an added benefit, our ability to simulate well the observed clouds can be used as a partial validation of the derived cloud fields.

To test this approach, we have used the HD parameterization (see Section 1 for a brief description) forced by the vertical velocity field shown in Fig. 22 and the relative humidity with respect to ice observed by CLASS radiosondes at Coffeyville (Fig. 20). Vertical velocities were computed at the top of each hour and are nominally valid during the 30 minutes before and after that hour. The humidities, however, were recorded only at 26/18, 26/21 and 27/00 and were, therefore, linearly interpolated to the hours where no observations were available. The resulting bulk ice water contents are shown in Fig. 23 for the period 26/18 to 27/00. The temporal and vertical variability of this figure should be compared with the radar reflectivities for the same period (Fig. 18). The simulated cloud is well correlated with the observations in terms of bulk structure, although some differences are apparent. The parameterization captured quite well the early development of the cirrus and the subsequent deepening of the cloud. This latter occurs somewhat earlier in the parameterized cloud than was actually observed. This may be due to the spatial averaging of the wind field but is more likely due to the linear interpolation of the water vapor time series.

We have attempted to quantify one aspect of the parameterized cloud by comparing optical depths retrieved from sun photometer observations and those derived from visible

satellite data (Minnis, 1993) with the optical depth parameterized from the ice water contents depicted in Fig. 23. To derive optical depths from the parameterized ice water contents, the temperature dependent size distribution parameterization reported by Heymsfield and Platt is used in conjunction with the radiative parameterization of Ebert and Curry (1992). Since the parameterized cloud properties represent time-averaged quantities, the sun photometer data of Shiobara and Asano (1994) were averaged to 30 minute values. These data were also corrected for forward scattering of photons into the solar beam. The satellite optical depths are computed after the technique of Minnis (1993) and represent spatially averaged (0.5 x 0.5 degree) data at a particular time. Table 1 shows the comparison. The parameterized and satellite-derived optical depths were temporally interpolated to the nominal valid times of the sun photometer data. Reasonable agreement is apparent early in the simulation with the three techniques reporting values less than or equal to two. At 1945 and 2019, the sun photometer and satellite techniques suggest thickening high clouds while the simulation suggests thinning. By 2045, however, agreement between the parameterized and sun photometer is apparent while the satellite-derived value changes little. The satellite-derived optical depth at 2045 is very uncertain due to increasing solar zenith angles. The discrepancies between the parameterized values and the observed quantities is maximized during the midpoint between soundings. In other words, agreement is good just after the 26/18 sounding and just before the 26/21 sounding. This indicates that three-hourly observations of the water vapor profile are not sufficient in this situation to resolve accurately the evolving moisture field. Comparisons for the entire period cannot be made because the sun photometer measurements are inaccurate at large optical thicknesses and low sun angles.

These simulation results are very encouraging from a number of perspectives. As shown theoretically by Starr and Cox (1985a and 1985b) and observationally by Starr and Wylie (1990) and Sassen et al. (1989), the large-scale vertical velocity is a crucial component in the dynamical forcing of tropospheric cloud systems. The quality of this simulation suggests that our analysis scheme captured the essence of the vertical velocity field during this time period. Obviously, large-scale thermodynamical fields are also critical. Again, the good quality of the simulation, including particularly the ice water path comparisons, attests to the accuracy of our analysis. The fact that the bulk characteristics of the cloud could be simulated adequately with synoptic-scale fields is encouraging from the point of view of GCMs, since our fields contain information at comparable scales to GCMs.

This approach also demonstrates a clear path whereby cloud parameterizations can be improved. By using the observed fields, we have decoupled the parameterization problem from the model generation of forcing fields. Thus, the simulated clouds rely only on the accuracy of the analysis and the details of the parameterization, and not on the model

simulation (or assimilation) of the large-scale fields. While our approach has some drawbacks, most importantly the lack of availability of the data we require, it permits a quantifiable, iterative approach to the improvement of cloud parameterizations.

Finally, we should emphasize that this is only a single case. We have compared results from several other periods during the FIRE Cirrus II campaign, finding varying degrees of agreement with cloud radar and satellite observations. For the most part, significant disagreement was caused by a lack of accurate water vapor data in the upper troposphere. This was due to obvious failure of the humidity sensors at cold temperatures and to poor temporal resolution of the sonde launches. The analyzed vertical velocities were questionable in several instances.

## 5. Summary and Conclusions

Field programs such as FIRE Cirrus II perform a valuable service to the scientific community by examining in great detail the evolution of cirrus clouds and associated radiative fields. Such a close examination provides a wealth of information from which generalizations can be made that ultimately influence the development of parameterizations. However, it can be stated unequivocally that one of the fundamental challenges to any attempt at improving cloud and radiation parameterizations in GCMs is how to actually couple the model atmosphere to the physical phenomena that are observed in the real atmosphere. This is true because, ultimately, it is the temporal and spatial scales of motion resolved by the model that drive the parameterizations. If the interaction between the scales represented by the GCM and that of the clouds is not thoroughly built into the parameterizations, increased knowledge of cloud microphysics and instantaneous radiation transfer through cirrus *will not* benefit climate prediction efforts. Examining the connection between the evolving large-scale meteorology (that which is resolvable by GCMs) and the observed macro-scale cloud properties has been the primary focus of this paper. We have concentrated on a 12 hour period from 12 UTC 26 November 1991 to 00 UTC 27 November 1991 during the field phase of FIRE Cirrus II held in Coffeyville, Kansas. The period we considered has become one of the focal cloud events of the field program.

We have utilized combined wind profiler and radiosonde data to generate the large-scale dynamical fields necessary for thorough analysis. Consistent with Thiebaut and Pedder (1987), Davies-Jones (1993) and Mace (1994), the analysis techniques were designed to minimize the uncertainty in the objectively analyzed quantities rather than to maximize the spatial resolution of the analysis product. As such, the analyses resolve synoptic scale variability and approximate a 2x2 degree grid resolution of a typical GCM. Hourly

kinematic analysis is possible using the time-space-converted (see Appendix A) WPDN data. However, thermodynamic analyses are limited by the launch schedule of the radiosonde network.

A primary result of this study is the obvious coupling that has been demonstrated between the evolution of the synoptic-scale dynamics and the maintenance of a middle and upper tropospheric cloud band. Central to our argument is the indirect vertical circulation associated with the exit region of the strong jet streak that propagated into the western portions of the analysis region during the afternoon of Nov. 26, 1991. The vertical circulation was found to be displaced to the cyclonic side of the jet, placing the descending branch below the jet axis and the ascending branch well to the left of the axis, just upstream of a small-amplitude, diffluent trough. The displacement of the circulation to the left of the axis was determined to have been caused by a combination of several factors. These included the amplifying diffluent trough, and a building ridge in the southwestern United States. This juxtaposition of evolving dynamical features ensured that the along-stream ageostrophic flow was evolving with time and could not be neglected as is assumed in the development of the Sawyer-Eliassen equation. The geostrophic forcing of the circulation was found to be due primarily to geostrophic confluence. While considerable warm air advection was diagnosed near the trough axis, small values of the geostrophic shearing deformation were ineffective in rotating the cross-stream thermal gradient into the along-stream direction. The forcing of the circulation due to scale contractions associated with geostrophic confluence was found to maximize just below the level of maximum wind and several kilometers above the center of the diagnosed vertical circulation.

Embedded within the ascending branch of the indirect circulation was a middle and upper tropospheric cloud band. The orientation of the cloud band with the dynamical structures identified above was maintained throughout the period of the case study. Satellite imagery indicated active cirrus generation in thin bands along the Kansas-Oklahoma border between 26/20 and 26/23. This region of cloud formation correlated positively in both space and time with the maximum vertical motions in the ascending branch of the jet-induced circulation. These cloud features were sampled extensively by the FIRE Cirrus-II field effort in southeastern Kansas and Northeastern Oklahoma. The cloud band consisted of cirrus generating cells early in the period (26/19-26/2130) and thickening middle tropospheric cloud after 26/2145.

We demonstrated that an effective technique to verify the response of cloud parameterizations to GCM-scale dynamics is to decouple the parameterization from the model and force it with data. The output of the parameterization can then be verified against observations. Forcing the HD parameterization with kinematically-derived vertical velocities

(Fig. 22) and radiosonde-observed humidities (Fig. 20), we were able to show good correspondence between the temporal and vertical variability of the parameterized clouds (Fig. 23) and that observed by cloud radar (Fig. 18). Additionally, reasonable agreement was displayed between HD parameterized ice water paths and those retrieved from sun photometer observations.

The favorable comparison between the observations and parameterized clouds leads to several conclusions:

1. Cirrus cloudiness formed as part of a baroclinic leaf cloud structure can be successfully parameterized using a diagnostic cirrus parameterization and large-scale dynamics. It should be noted that, due to low horizontal wind speeds in the cirrus generation region, horizontal advection of ice over large distances was likely not a factor. Thus, the bulk diagnostic scheme performed well.

2. Given the sensitivity of the HD parameterization to the large-scale vertical velocity, we conclude that the diagnostic analyses generated from the WPDN data were of high enough quality to capture the essence of the vertical velocity field over Coffeyville. This also lends credence to the overall dynamical setting derived from the WPDN analysis of a jet-induced vertical circulation displaced poleward of the jet axis.

3. The technique used to test the HD parameterization is viable assuming adequate availability of input fields and of suitable verification data. The technique *requires* hourly wind profiler data from at least seven stations spread in an array about a central location. Thermal and moisture fields with at least three hourly resolution are essential but may not be sufficient in certain situations. Hourly values derived from RASS and Raman lidar would be ideal and are necessary in certain situations. At this point the only verification of the parameterized cloud properties is through remote sensing measurements of internal structure. Since aircraft-based verification of these techniques may not be possible (Vogleman and Ackerman, This Issue), greater emphasis needs to be placed on accurate cloud property retrievals from remotely sensed data. Finally, it is quite obvious that a single case study is not sufficient. For this technique to be truly effective, examination of numerous events over a significant time period (1-2 years) needs to be carried out.

While short term intensive field campaigns like FIRE Cirrus II are absolutely essential for collecting in-situ and remotely sensed cloud data for process studies and model development, the points made above show the weakness of campaigns in parameterization



testing and verification from data. The Department of Energy's (DOE) Atmospheric Radiation Measurement (ARM) program (Sokes and Schwartz, 1994) is specifically designed to address point 3 above. ARM has established a long-term observational facility known as the Southern Great Plains (SGP) Clouds and Radiation Testbed (CART) site within the inner array of the WPDN (Fig. 1). This facility will provide the verification data needed for parameterization development and testing. The ARM program is, essentially, built around the concept known as single column modeling (SCM) where all physical parameterizations are forced by observed dynamical fields. The discussion we presented built around the HD parameterization is a first step in the SCM concept. If properly implemented over a significant period of time, improvements in GCM parameterizations will follow. However, the success of the SCM concept applied to the SGP CART site depends primarily on the quality of the input data. A primary component of the input data is observations from the inner array of the WPDN. No other observational platform can generate the temporal, vertical and spatial consistency needed in the SCM concept. It can be stated with reasonable certainty that without a high quality data stream from the inner array of the WPDN, the data-based SCM approach originally envisioned by ARM will not succeed.

Our future work is directed at more quantitative verification of cirrus cloud parameterizations. Using the size distributions described by Heymsfield and Platt (1984) and the radiative parameterization of Ebert and Curry (1991), we are performing full radiative calculations based on the HD parameterization derived from the entire FIRE Cirrus II dataset. These results are being verified with surface-based observations and satellite-derived properties. These techniques, derived from the FIRE Cirrus-II period, are being ported to operationally process the ARM SGP data stream. Current plans are to implement a full data-based single column model (Iacobellis and Sommerville, 1991) and to apply this model to long time series of data.

### *Acknowledgments*

We are grateful for to Miss Laurie Bothell for assistance in preparing the manuscript, to Dr. Eugene Clothiaux for many useful and insightful discussions and to Bill Smith and Andy Lare for help in preparing the figures and acquiring satellite data. This research was supported by the National Aeronautics and Space Administration (Grant NAG-1-1095) and by the U. S. Department of Energy (Grant DE-FG02-90ER61071).

## Appendix A

### Time-Space Conversion Technique

In the past, the temporal resolution of observed tropospheric wind profiles was limited to the time required for a radiosonde to make an ascent from the surface to the tropopause. The finest temporal resolution possible tended to be about 2-3 hours. Also, due to the cost of operating temporally enhanced radiosonde networks, this resolution was only possible for short durations. A distinct advantage of wind profiler observations is the temporal continuity of the vertical profiles. To take advantage of the temporal continuity, an algorithm has been developed that converts the observed temporal characteristics of the wind into a spatial distribution of independent observations.

To preserve the integrity of the data, the time-space conversion (TSC) technique described here is limited in scope and is applied during a three hour period only when certain conditions are met. The period that is considered for the conversion extends from 1 hour before (denoted  $t_{-1}$ ) to one hour after ( $t_{+1}$ ) a current ( $t_0$ ) observation. All three observations in time at a particular level must be present. The assumption is made that the winds along a curved trajectory streamline are subject only to the centripetal acceleration necessary to maintain the air parcels on the streamline. Additionally it is assumed that the wind speeds vary linearly along the trajectory. With these assumptions, the approximation can be made that  $\mathcal{V}_{s_u}^t \cong \mathcal{V}_{s_p}^{t+1}$  and  $\mathcal{V}_{s_d}^t \cong \mathcal{V}_{s_p}^{t-1}$  where the superscripts refer to the time and the subscripts refer to a distance upstream ( $s_u$ ), downstream ( $s_d$ ) and at the profiler location ( $s_p$ ). Therefore, the distances,  $s_u$  and  $s_d$  are increments of arc appropriate for the location of the winds  $\mathcal{V}_{s_p}^{t+1}$  and  $\mathcal{V}_{s_p}^{t-1}$ , respectively. These distances are estimated using forward and backward finite differencing to be,

$$s_u = -\Delta t \frac{(\mathcal{V}_{s_p}^0 + \mathcal{V}_{s_p}^{t+1})}{2}$$

$$s_d = \Delta t \frac{(\mathcal{V}_{s_p}^0 + \mathcal{V}_{s_p}^{t-1})}{2}$$

The endpoints of the streamline trajectories must be located in space. The schematic in Fig. A1 shows the geometry that is considered. It is assumed that the streamline defined by the three observations has a single radius of curvature.  $\mathcal{R}_t$  is estimated by first mapping the

WPDN observations at time,  $t_0$ , to a Cartesian grid and then estimating the radius of streamline curvature,  $\mathcal{R}_s$ , by incrementally stepping forward and backward along an arc of 100 km that is defined by the spatial distribution of wind observations. After determining  $\mathcal{R}_s$ ,  $\mathcal{R}_t$  can be estimated using the equation (Holton, 1993),

$$\frac{1}{\mathcal{R}_t} = \frac{1}{\mathcal{R}_s} + \frac{1}{V_s^b} \frac{\partial \beta}{\partial t}$$

where  $\beta$  is the observed wind direction at the profiler site and  $\partial \beta / \partial t$  is estimated using centered differencing. Since the uncertainty in  $\mathcal{R}_t$  increases with increasing curvature, the TSC algorithm does not continue if  $\mathcal{R}_t$  is found to be less than 1000 km. The center of rotation of the parcel trajectory is then determined by noting that  $\mathcal{R}_t$  is normal and to the wind direction and to the left (right) of the flow for positive (negative)  $\mathcal{R}_t$ . Therefore,

$$\begin{aligned} x_c &= x_p - \mathcal{R}_t \cos(\beta) \\ y_c &= y_p - \mathcal{R}_t \sin(\beta) \end{aligned}$$

where  $x_c$  and  $y_c$  are the coordinate locations of the center of curvature and  $x_p$  and  $y_p$  are the coordinates of the profiler. The upstream and downstream locations are then estimated by noting that,

$$\begin{aligned} \alpha_{s_u} &= \frac{s_u}{\mathcal{R}_t} \\ \alpha_{s_d} &= \frac{s_d}{\mathcal{R}_t} \end{aligned}$$

where  $\alpha_{s_u}$  and  $\alpha_{s_d}$  are the angles subtended by the upstream and downstream locations with the radius of trajectory curvature. Therefore,

$$\begin{aligned} x_u &= x_c + \mathcal{R}_t \cos(\alpha_u + \beta) \\ y_u &= y_c + \mathcal{R}_t \sin(\alpha_u + \beta) \\ x_d &= x_c + \mathcal{R}_t \cos(\beta - \alpha_d) \\ y_d &= y_c + \mathcal{R}_t \sin(\beta - \alpha_d) \end{aligned}$$

are the upstream and downstream locations assigned to the winds observed by the profiler at times  $t_{+1}$  and  $t_{-1}$  respectively.

Appendix B  
Kinematic Vertical Velocities from Wind Profiler Data

The profile of vertical velocity can be determined by solving the continuity equation (Holton, 1993),

$$\frac{\partial \rho}{\partial t} + (\nabla_h \bullet \rho \vec{v}_h) = -\frac{\partial}{\partial z}(\rho w) \quad (\text{B1})$$

assuming the vertical profile of horizontal divergence is known to good accuracy and appropriate boundary conditions are specified. In most previous applications of the kinematic method, pressure was used as the vertical coordinate since the winds necessary to determine the horizontal divergence were acquired from radiosonde data. An exception to this is the work of Carlson and Forbes, 1988, and Hermes, 1991. Since wind profilers measure the wind in physical height coordinates, no supplemental thermodynamic information is generally available that allows unambiguous mapping of the measured horizontal winds onto pressure surfaces. Therefore, in order to make the application of the kinematic method as general as possible, the continuity equation must be solved in a geometric height coordinate system.

Applying a vector identity to the mass flux convergence term on the right of Eqn. B1, using scale analysis for midlatitude synoptic-scale motion (Holton, 1993), substituting for the air density from the ideal gas law in the second term on the left, dividing through by the air density, and solving for the vertical gradient of the vertical velocity from the three dimensional velocity divergence, Eqn. B1 can be written,

$$\frac{\partial w}{\partial z} = w \left( \frac{g}{RT} + \frac{1}{T} \frac{\partial T}{\partial z} \right) - (\nabla \bullet \vec{v}_h) - \frac{\partial \ln \rho}{\partial t} \quad (\text{B2})$$

where all symbols take on their usual definitions and the subscript  $h$  is used to signify that only the horizontal components are considered. Eqn. B2 is a first order, linear, non-homogeneous differential equation that has a solution,

$$w_{i+1} = \exp \left[ -\int_{z_i}^{z_{i+1}} \frac{c_1}{T} dz \right] * \int_{z_i}^{z_{i+1}} \left( -\nabla \bullet \vec{V}_h - \frac{\partial \ln \rho}{\partial t} \right) \exp \left[ -\int_{z_i}^z \frac{c_1}{T} dz' \right] dz + c * \exp \left[ -\int_{z_i}^{z_{i+1}} \frac{c_1}{T} dz \right] \quad (\text{B3})$$

where  $c_1 = \frac{g}{R} + \frac{\partial T}{\partial z}$ . The subscripts  $i$  and  $i+1$  represent discrete vertical levels and  $w_{i+1}$  is the vertical velocity at the vertical level  $i+1$  determined by solving the right hand side using the vertical velocity,  $w_i$ , as a lower boundary condition. Eqn. B3 can be simplified by bringing the first exponential term on the right within the leading integrand. The integral arguments of the exponential terms then subtract, changing the limits of integration in the argument of the exponential. The resulting expression can be written,

$$w_{i+1} = \int_{z_i}^{z_{i+1}} \left( -\nabla \cdot \bar{V}_h - \frac{\partial \ln \rho}{\partial t} \right) \exp \left[ \int_{z'}^{z_{i+1}} \frac{c_1}{T} dz' \right] dz + c * \exp \left[ \int_{z_i}^{z_{i+1}} \frac{c_1}{T} dz' \right], \quad (B4)$$

The solution of the equation for the vertical velocity at some level then depends on the vertical profile of horizontal divergence, the time rate of change of air density and a boundary condition. For simplicity of notation, the time rate of change of air density will be incorporated in to the horizontal divergence in the remaining mathematical development and the difference of the horizontal divergence and the local air density tendency will be denoted by the horizontal divergence. The boundary value,  $c$ , is the vertical velocity at the bottom or top of the vertical interval depending of the integration is performed upwards or downwards. The development here will assume an upward integration. Since the horizontal divergence and temperature are assumed known, this equation can be solved analytically by accounting for the vertical discretization of the data.

Following Hermes (1991), the assumption is made that the horizontal divergence varies linearly between data points according to the following equation,

$$\text{Divg}(z) = m_D z + B_D$$

where  $m_D$  represents the slope of the divergence between data points, and  $B_D$  is the intercept. It must be further assumed that the temperature in the layer being considered is isothermal with a value midway between the temperature at the top and bottom of the layer. In other words, the assumption is made that the vertical temperature profile is piecewise isothermal. The impact of these two assumptions will be discussed below. Applying the isothermal assumption to the temperature profile and evaluating the integrals to the exponential arguments, Eqn. B4 becomes

$$w_{i+1} = -\exp\left\{-\frac{c_1}{T_0} z_{i+1}\right\} \int_{z_i}^{z_{i+1}} (\nabla \cdot \vec{v}_h) \exp\left\{-z \frac{c_1}{T_0}\right\} dz + w_i * \exp\left\{-\frac{c_1}{T_0} \Delta z\right\}.$$

Invoking the piecewise linear assumption to the horizontal divergence, we can write

$$w_{i+1} = -\exp\left[-\frac{c_1}{T_0} z_{i+1}\right] \left\{ m_D \int_{z_i}^{z_{i+1}} z \exp\left[-z \frac{c_1}{T_0}\right] dz + B_D \int_{z_i}^{z_{i+1}} \exp\left[-z \frac{c_1}{T_0}\right] dz \right\} + w_i \exp\left[-\frac{c_1}{T_0} \Delta z\right].$$

The two resulting integral terms on the right can now be evaluated analytically,

$$w_{i+1} = -\frac{\exp\left[-\frac{c_1}{T_0} z_{i+1}\right] T_0}{c_1} \left( m_D \left\{ \exp\left[-\frac{c_1}{T_0} z\right] \left(z - \frac{T_0}{c_1}\right) \right\}_{z_i}^{z_{i+1}} + B_D \left\{ \exp\left[-\frac{c_1}{T_0} z\right] \right\}_{z_i}^{z_{i+1}} \right) + w_i * \exp\left[-\frac{c_1}{T_0} \Delta z\right] \quad (\text{B5})$$

The sensitivity of Eqn. B5 to the assumptions imposed on the profiles of temperature and horizontal divergence was examined with several analytical functions. The sensitivity to the assumption imposed on the temperature profile was found to be negligible in all cases. The difference in the vertical velocities derived with an analytical divergence profile and a discrete version of the profile reached a maximum of  $0.5 \text{ cms}^{-1}$  only when a single convergence/divergence couplet existed in the vertical column.

A further limitation to the accuracy of Eqn. B5 when applied to wind profiler network data is the specification of an appropriate lower boundary condition. Since the lowest data level occurs near 500 m above the local ground level with the WPDN data, a significant portion of the near-surface layer is not sampled. Therefore, the most obvious boundary condition, that the vertical velocity at the surface is zero, becomes somewhat more difficult to impose. Hermes (1991) estimated the vertical velocity across the lower data boundary using estimates from a radiosonde network. Carlson and Forbes (1989) reasoned that the vertical motions in the lower stratosphere are typically small in a mass-weighted sense and solved the continuity equation from the top of the column to the lowest level. Since the data column observed by the WPDN wind profilers begins near 500 m above ground level (Hermes' data ended at 2.3 km while Carlson's and Forbes' data ended near 1 km), the horizontal divergence is linearly extrapolated from the lowest

data layers to the surface where the vertical velocity is known to be zero. The influence of sloping terrain is ignored due to the low relief typical of the analysis region.

As noted by numerous investigators (O'Brien, 1970; Holton, 1977; Carlson and Forbes, 1989; Starr and Wiley, 1990), errors in the horizontal divergence at a particular level tend to be communicated to all higher levels. This results in large uncertainties in the calculated vertical motions. Therefore, the technique described by O'Brien (1970) is applied. This procedure adjusts the profile of horizontal divergence so that the vertical motion is forced to obey a specified upper boundary condition. Since the WPDN data generally reaches the lower stratosphere, an upper condition of  $w=0$  is imposed. Using random error generally expected from objectively analyzed wind profiler and radiosonde data ( $\leq 2.5 \times 10^{-5} \text{ s}^{-1}$ ) it was found that the RMS uncertainty in the kinematic vertical velocity when adjusted by the O'Brien technique was on the order of  $2 \text{ cms}^{-1}$ .



## Figure Captions

Figure 1. Map showing the locations of wind profiler and radiosonde sites that were operational during the FIRE II Cirrus Intensive Field Operation during November and early December 1991. The blackened squares represent WPDN sites, the open squares represent operational radiosonde locations and the open diamonds denote the locations of CLASS radiosonde sites. Coffeyville, Ks is denoted by a diamond within an open square.

Figure 2. Scatter diagram of the objectively analyzed horizontal wind components (abscissa) compared with the wind profiler-observed horizontal wind components (ordinate). The units are  $\text{ms}^{-1}$ . The RMS difference in the objectively analyzed components and the observations is  $3.2 \text{ ms}^{-1}$ .

Figure 3. a) Amplitude response function of the overdetermined least squares spatial filter described in the text. The solid circles are the amplitude response of the wind speed and the open circles denote the amplitude response of the vertical component of the relative vorticity. b) Arrangement of grid points corresponding to the amplitude response curves shown in a). The solid circle is the central gridpoint that is being smoothed by the distribution of surrounding gridpoints.

Figure 4. The synoptic setting for the case study period under consideration. a) 300 mb heights and wind vectors at 12 UTC 26 November, 1991. b) surface pressure analysis at 12 UTC 26 November, 1991. The contour interval is 4 mb for the surface pressure and 60 m for the thickness. c) 300 mb heights and wind vectors at 00 UTC 27 November, 1991. Plotting convection as in a. d) surface pressure at 00 UTC 27 November, 1991. Plotting convention as in b.

Figure 5. Infrared satellite imagery. a) 18 UTC 26 November. b) 21 UTC 26 November. c) 00 UTC 27 November, 1991.

Figure 6. Horizontal wind vectors and speeds analyzed from the time-space converted WPDN data at a) 18 UTC 26 November, 1991 and b) 00 UTC 27 November, 1991. The wind vectors are compass direction and the vector lengths are proportional to wind speed. The contours are of wind speed in  $\text{m s}^{-1}$ . The contour interval is  $2 \text{ m s}^{-1}$ . The solid squares denote the location of wind profiler observations used in the objective

analysis. The straight solid, dashed and dotted lines in (b) denote the location of horizontal cross sections discussed discussed later in the text.

Figure 7. 10 km Horizontal divergence and relative vorticity. a) 18 UTC 26 November horizontal divergence. b) 18 UTC 26 November relative vorticity. c) 00 UTC 27 November horizontal divergence and d) 00 UTC 27 November relative vorticity. The contour interval in (a) and (c) is  $1 \times 10^{-5} \text{ s}^{-1}$  and in (b) and (d),  $4 \times 10^{-5} \text{ s}^{-1}$ . Thick solid lines denote negative contours.

Figure 8. Natural coordinate components of the horizontal divergence. a) 18 UTC 26 November speed diffluence. b) 18 UTC 26 November directional diffluence. c) 18 UTC 26 November curvature advection. d) 00 UTC 27 November speed diffluence. e) 00 UTC 27 November directional diffluence. f) 00 UTC 27 November curvature advection. The plotting convention is as in Figure 7 except that the contour interval for the curvature advection is  $1 \times 10^{-5} \text{ s}^{-1}$ .

Figure 9. Ageostrophic wind and natural coordinate components of the ageostrophic wind. a) 18 UTC 26 November ageostrophic vectors and speeds. b) 18 UTC 26 November along-stream component. c) 18 UTC 26 November cross-stream component. d) 00 UTC 27 November ageostrophic vectors and speeds. e) 00 UTC 27 November along-stream component. f) 00 UTC 27 November cross stream component. The vectors in a and d are as in Figure 6 with a contour interval of  $10 \text{ m s}^{-1}$ . The contour interval in b, c, e, and f are  $5 \text{ m s}^{-1}$  with negative values contoured with thicker lines.

Figure 10. Curvature component of the relative vorticity at 00 UTC 27 November. The contour interval is  $1 \times 10^{-5} \text{ s}^{-1}$  with negative values contoured with bolder lines.

Figure 11. Horizontal cross section at 21 UTC 26 November along the thick straight line shown in Figure 6. The cross section is oriented such that the left side of the plot is the southern end of the solid line in Figure 6b. a) Horizontal wind vectors and speeds. The vectors are compass direction with north towards the top of the page and the contour interval is  $5 \text{ m s}^{-1}$ . b) The cross-stream component of the ageostrophic wind. Contour interval is

5 m s<sup>-1</sup>. c) The kinematically derived vertical velocity. The contour interval is 2 cm s<sup>-1</sup>. d) The ageostrophic circulation vectors derived by combining the fields in (b) and (c). The vectors are overlain on the potential temperature contoured at a 2 K interval.

Figure 12. Schematic illustration of sign and forcing and sense of the transverse ageostrophic circulation from the diagnostic Sawyer-Eliassen equation. Ageostrophic circulation is denoted by solid lines; dashed lines depict an isentrope separating potentially colder from warmer air. Small circles enclosing  $x$  and dot respectively indicate along-front wind into and out of the cross section. Transverse ageostrophic circulation is thermodynamically direct in (a) and indirect in (b). (After Keyser and Shapiro, 1986).

Figure 13. Components and total forcing the Sawyer-Eliassen equation for 21 UTC 26 November 1991. a) Q1, b) Q2 and c) Q1+Q2. See text for description of the forcing terms and their physical significance to the diagnosed ageostrophic circulation.

Figure 14. High cloud visible optical depths derived from GOES data at 18 UTC 26 November.

Figure 15. GOES 7 Infrared imagery showing the progression of the middle and upper tropospheric cloud system through the Kansas-Oklahoma region at a) 21 UTC 26 November 1991, b) 22 UTC 26 November 1991, c) 23 UTC 26 November 1991 and d) 00 UTC 27 November 1991

Figure 16. Kinematic vertical velocity cross sections along the dashed line in Figure 6. The cross sections are oriented such that the left side of the plot is the western end of the dashed line in Figure 6. a) 18 UTC 26 November. b) 21 UTC 26 November. c) 00 UTC 27 November. The contour interval is 1 cm s and negative values are contoured with dashed lines.

Figure 17. Kinematic vertical velocity cross section along the dotted line in Figure 6 at 21 UTC 26 November. The cross section is oriented such that the left side of the plot is the northern end of the dotted line in Figure 6. The plotting convention is as in Figure 16.

Figure 18. Time-height cross of reflectivities (dBZe) observed by the Pennsylvania State University 94 GHz cloud radar from 1800 UTC 26 November to 0000 UTC 27 November, 1991.

Figure 19. Time series of temperature soundings at Coffeyville, Kansas from 15 UTC 26 November 1991 to 00 UTC 27 November 1991. The profiles are each offset by 10°C with 15 UTC on the left. Also depicted are the relative humidity profiles denoted by the shading extending to the right of each profile. The humidities are with respect to ice at temperatures below -20°C and with respect to liquid water at temperatures greater than 0°C. Between these temperatures the humidity is calculated as a linear combination of ice and liquid water. The shading begins at 40%.

Figure 20. Time-height cross sections of the relative humidity determined as in Figure 19 from 12 UTC 26 November 1991 to 00 UTC 27 November 1991 for a) Coffeyville, Kansas; b) Iola, Kansas; c) Arkansas City, Oklahoma and d) Muskogee, Oklahoma. See Figure 1 for the locations of these sites.

Figure 21. Potential temperature profile time series beginning at 12 UTC 26 November 1991 to 00 UTC 27 November 1991 for a) Coffeyville, Kansas; b) Iola, Kansas; c) Arkansas City, Oklahoma and d) Muskogee, Oklahoma. Each successive profile is offset by 10°C as in Figure 19 and isentropes are drawn every 1K.

Figure 22. Kinematic vertical velocity time-height cross section derived from the wind profiler horizontal divergence values interpolated to Coffeyville, Kansas. The plot is from 18 UTC 26 November to 00 UTC 27 November. The contour interval is 2 cm s<sup>-1</sup> and the zero contour is dashed.

Figure 23. Ice water content time-height cross section derived from the Heymsfield-Donner parameterization from 18 UTC 26 November to 00 UTC 27 November. These values were determined by forcing the parameterization with the vertical velocities shown in Figure 22 and the water vapor observed by radiosonde at Coffeyville (Figure 20). No calculations were performed for temperatures above freezing although the parameterization computes ice water contents at warmer temperatures due to precipitation from above.

Figure A1. The geometry considered in the time-space conversion algorithm discussed in Appendix A.

### **Table Caption**

Table 1. Comparison between visible optical depths during the local afternoon of 26 November 1991. The values were determined using the cirrus parameterization described in the text, 30 minute averaged sun photometer data and satellite-observed visible data. See the text for further explanation.

## References

- Ackerman, T. P., K. N. Liou, F. P. Valero, and L. Pfister, 1988: Heating rates in tropical anvils. *J. Atmos. Sci.*, **45**, 1606-1623.
- Akima, H., 1978: A method of bivariate interpolation and smooth surface fitting for values given at irregularly distributed points. *ACM-TOMS*, **4**.
- Akima, H., 1984: On estimating partial derivatives for bivariate interpolation of scattered data. *Rocky Mtn. J. Math.*, **14**.
- Cammas J. and D. Ramond, 1989: Analysis and diagnosis of the composition of ageostrophic circulations in jet-front systems. *Mon. Wea. Rev.*, **117**, 2447-2462.
- Chadwick, R. B., 1986. Wind profiler demonstration system. Handbook of MAP, Vo. 20, June 1986, URSI/SCOPEP Workshop on Technical and Scientific Aspects of MST Radar, 336-337.
- Clothiaux, E. E., M. A. Miller, B. A. Albrecht, T. P. Ackerman, J. Verlinde, R. M. Peters, W. J. Syrett, 1994: An Evaluation of a 94-GHz radar for remote sensing of cloud properties. *J. Atmos. Ocean. Technol.*, (Submitted).
- Conover, J., 1960: Cirrus patterns and related air motions near the jet stream as derived by photography. *J. Meteor.*, **17**, 532-546
- Davies-Jones, R., 1993: Useful formulas for computing divergence, vorticity, and their error from three or more stations, *Mon. Wea. Rev.*, **121**.
- Ebert E. E. and J. A. Curry, 1992: A parameterization of ice cloud optical properties for climate models. *J. Geophys. Res.*, **97**, 3831-3836.
- Fischler, M. A., and R. C. Bolles, 1981: Random sample consensus: A paradigm for model fitting with applications to image analysis and automated cartography. *Commun. Assoc. Comput. Mach.*, **24**, 381-395.
- Frankhauser, J. C., 1969: Convective processes resolved by a mesoscale rawinsonde network. *J. Appl. Meteor.*, **8**, 778-798.
- Gage, K. S. and B. B. Balsley, 1978: Doppler radar probing of the clear atmosphere. *Bull. Amer. Meteor. Soc.*, **59**, 1074-1092.
- Heymsfield, A. J., 1977: Precipitation development in stratiform ice clouds: A microphysical and dynamical study. *J. Atmos. Sci.*, **34**, 367-381.
- Heymsfield, A. J. and C. M. R. Platt, 1984: A parameterization of the particle size spectrum of ice clouds in terms of the ambient temperature and the ice water content. *J. Atmos. Sci.*, **41**, 846-855.
- Heymsfield, A. J., and L. J. Donner, 1990: A scheme for parameterizing ice-cloud water content in general circulation models. *J. Atmos. Sci.*, **47**, 1865-1877.

- Holton, J. R., 1979: *An introduction to dynamic meteorology*. Academic Press Inc., Orlando, FL, 391pp.
- Iacobellis II, S. F. and R. C. J. Somerville, 1991: Diagnostic modeling of the Indian monsoon onset. Part I: Model description and validation. *J. Atmos. Sci.*, **48**, 1948-1959.
- Keyser, D., and M. A. Shapiro, 1986: A review of the structure and dynamics of upper-level frontal zones. *Mon. Wea. Rev.*, **114**, 452-499.
- Liou, K. N., 1986: Influence of cirrus clouds on weather and climate: A global perspective. *Mon. Wea. Rev.*, **114**, 1167-1199.
- Mace, G. G. 1994: *Development of large-scale diagnostic analysis techniques applicable to regional arrays of wind profilers and radiosondes*. Ph. D. dissertation, The Pennsylvania State University, University Park, 261 pp.
- Minnis, P., K. Liou and Y. Takano, 1993: Inference of cirrus cloud properties using satellite-observed visible and infrared radiances. part I: parameterization of radiance fields. *J. Atmos. Sci.*, **50**, 1279-1304.
- Minnis, P., P. W. Heck and D. F. Young, 1993: Inference of cirrus cloud properties using satellite-observed visible and infrared radiances. Part II: verification of theoretical cirrus radiative properties. *J. Atmos. Sci.*, **50**, 1305-1322.
- Sanders, F., 1990: Initiation and evolution of an intense upper level front. *Mon. Wea. Rev.*, **119**, 1337-1367.
- Sassen, K., D. O'C. Starr, and T. Uttal, 1989: Mesoscale and microscale structure of cirrus clouds: Three case studies. *J. Atmos. Sci.*, **46**, 371-396
- Sassen, K., D. O'C Starr, G. G. Mace, M. R. Poellot, S. H. Melfi, W. L. Eberhard, J D. Spinhirne, E. W. Eloranta, D. E. Hagen and J. Hallet, 1994: The 5-6 December 1991 FIRE IFO II jet stream cirrus case study: The influence of volcanic aerosol. *J. Atmos. Sci.* (In Press).
- Shapiro, M. A., 1978: Further evidence of the mesoscale and turbulent structure of upper level jet stream-frontal zone systems. *Mon. Wea. Rev.*, **106**, 1100-1111.
- Shapiro, M. A., 1981: Frontogenesis and geostrophically forced secondary circulations in the vicinity of jet stream-frontal systems. *J. Atmos. Sci.*, **38**, 954-973.
- Shiobara, M. and S. Asano, 1994: Estimation of cirrus optical thickness from sunphotometer measurements. *J. Appl. Meteor.*, (In Press).
- Slingo, J. M., 1987: The development and verification of a cloud prediction scheme for the ECMWF model. *Q. J. R. Meteorol. Soc.*, **113**, 899-927.
- Soden, B. J. and L. J. Donner, 1994: Evaluation of a GCM cirrus parameterization using satellite observations. *J. Geophys. Res.*, (In Press)
- Starr, D. O'C and S. K. Cox, 1980: Characteristics of middle and upper tropospheric clouds as deduced from rawinsonde data. Colorado State University *Atmospheric Sciences Paper No. 327*, 71 pp.
- Starr, D. O'C. and S. K. Cox, 1985a: Cirrus clouds. Part I: A cirrus cloud model, *J Atmos. Sci.*, **42**, 2663-2681



- Starr, D. O'C. and S. K. Cox, 1985b: Cirrus clouds. Part II: Numerical experiments on the formation and maintenance of cirrus, *J Atmos. Sci.*, **42**, 2663-2681
- Starr, D. O'C., and D. P. Wylie, 1990: The 27-28 October 1986 FIRE cirrus case study: Meteorology and clouds. *Mon. Wea. Rev.*, **118**, 2259-2287.
- Stone, R. G., 1957: *A Compendium on Cirrus and Cirrus Forecasting*. AWS/TR 105-130, Air Weather Service, Scott AFB, IL, 62225, 80 pp.
- Strauch, R. G., B. L. Weber, A. S. Frisch, C. G. Little, D. A. Merritt, K. P. Moran and D. C. Welsh, 1987: The precision and relative accuracy of profiler wind measurements. *J. Atmos. Ocean. Technol.*, **4**, 563-571.
- Thiebaux, H. J. and M. A. Pedder, 1987: *Spatial objective analysis, with applications in atmospheric science*, Academic Press Inc., London, 299 pp.
- Weldon, R., 1979: *Cloud Patterns and the Upper Tropospheric Wind Field*. AWS/TR-79/003, Air Weather Service, Scott, AFB, IL, 62225, 80 pp.
- Zamora R.F., M.A. Shapiro, and C.A. Doswell III, 1987: The diagnosis of upper tropospheric divergence and ageostrophic wind using profiler wind observations. *Mon. Wea. Rev.*, **115**, 871-884.



	Parameterization	Sun Photometer	Satellite
1845	1.7	1.2	1.1
1915	2.0	1.7	1.9
1945	1.5	3.5	2.8
2019	1.5	3.0	3.6
2045	1.9	1.5	3.4

Table 1.

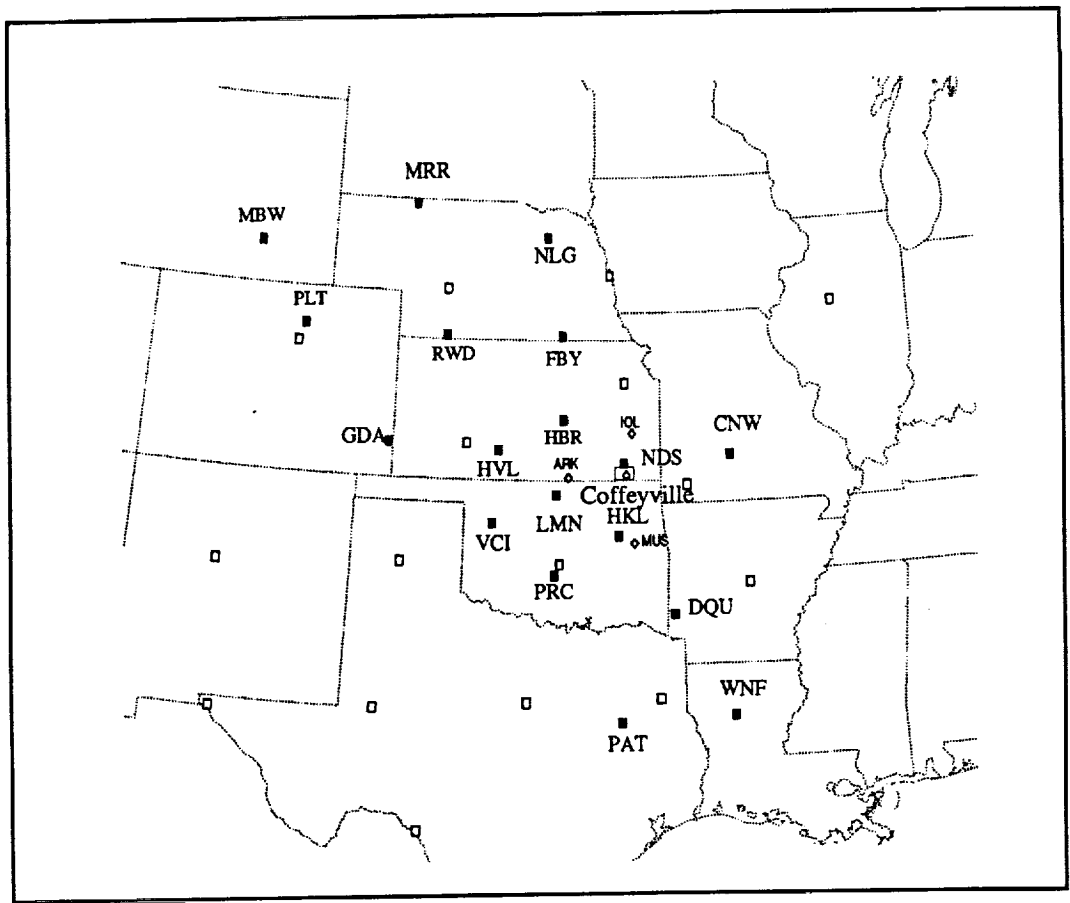


Fig 1

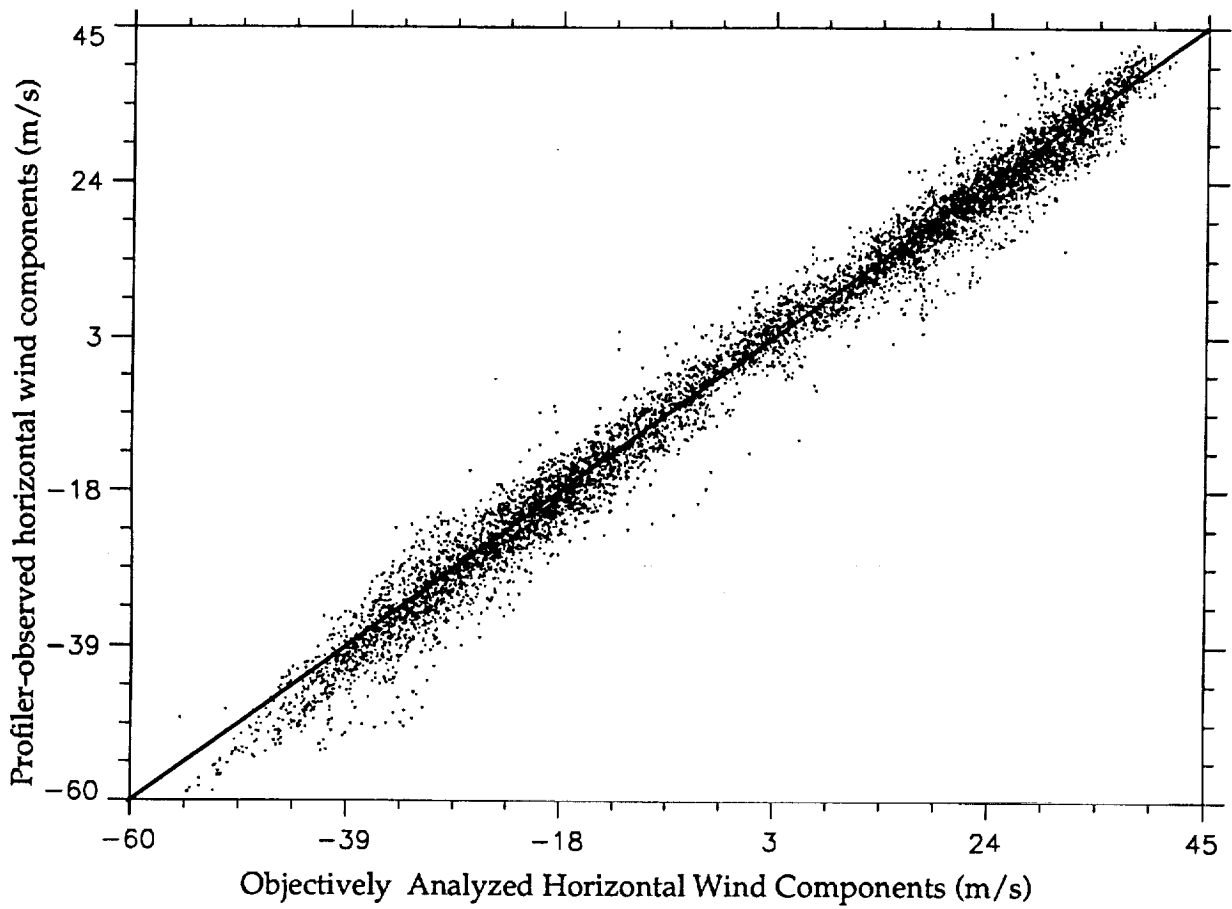


Fig. 2

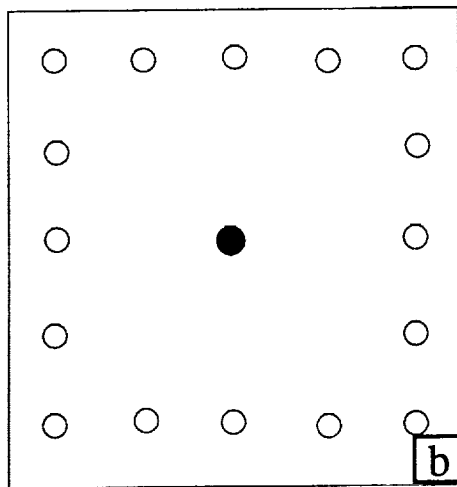
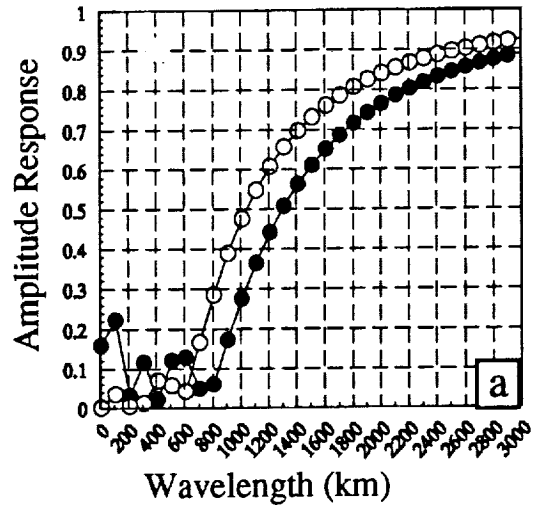


Fig. 3

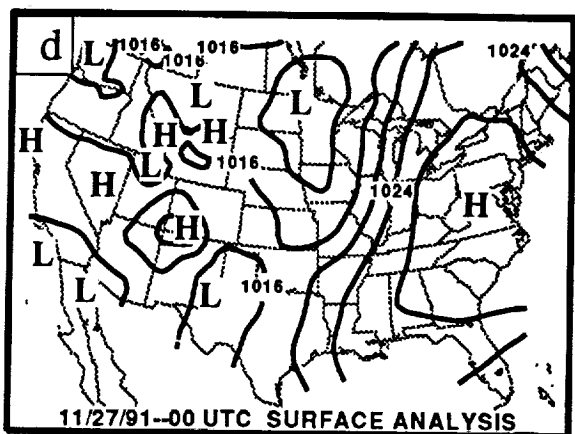
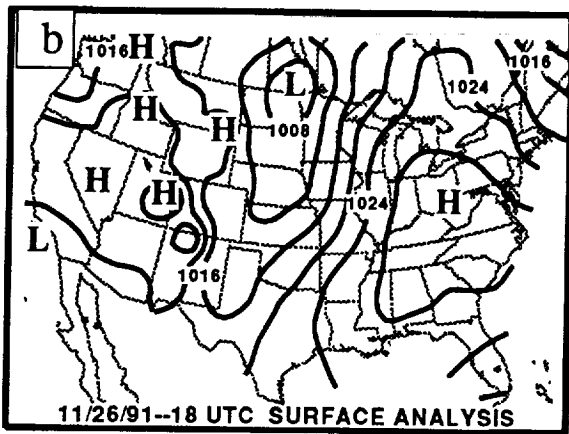
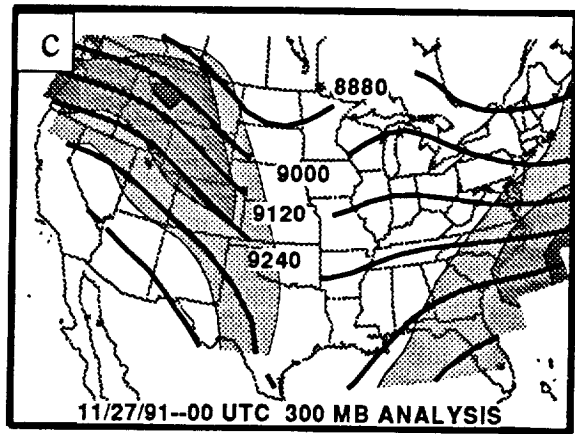
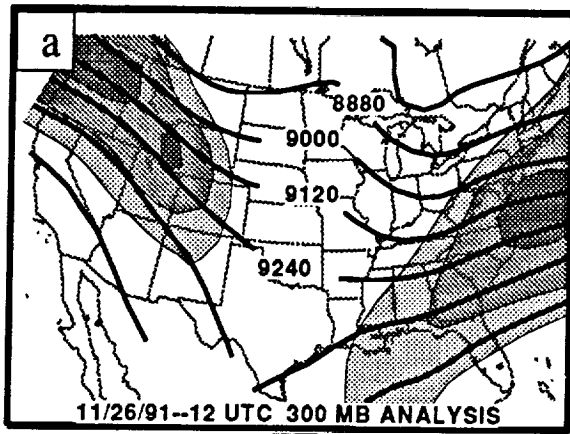
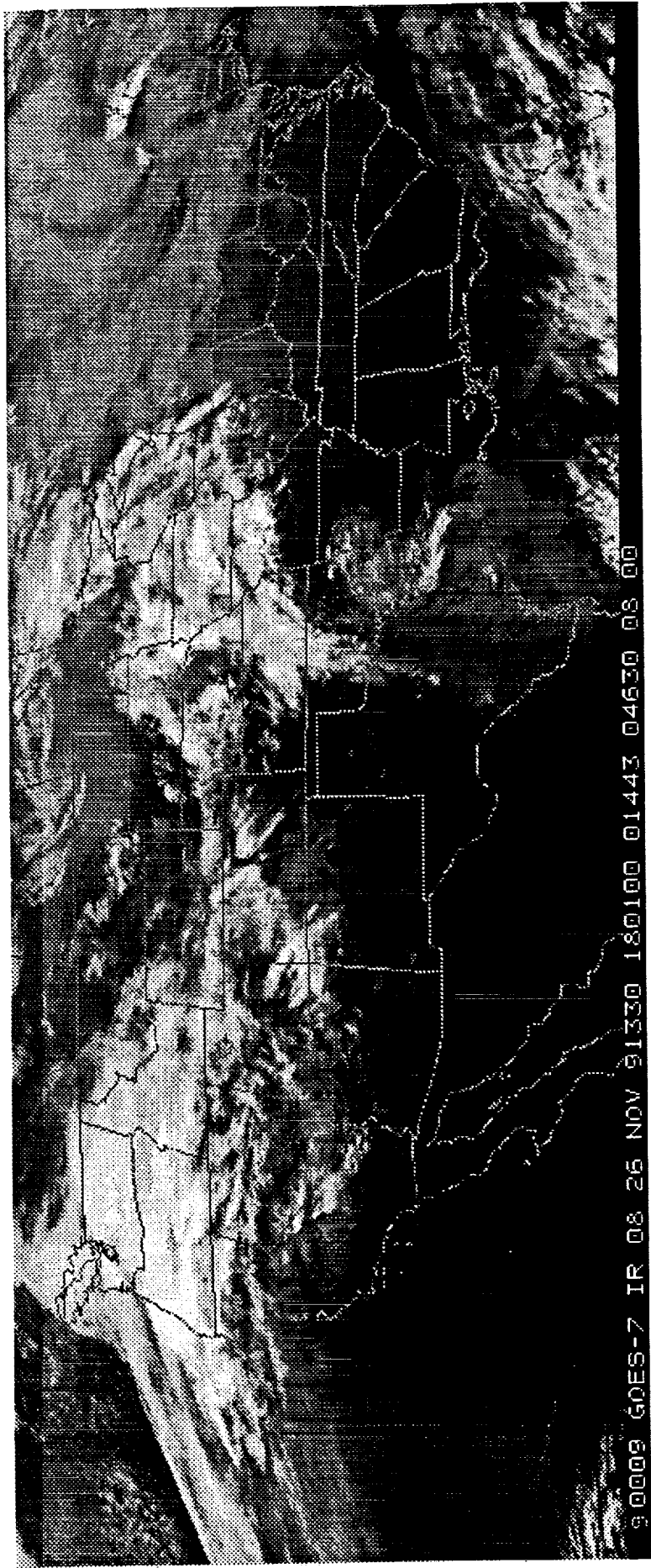
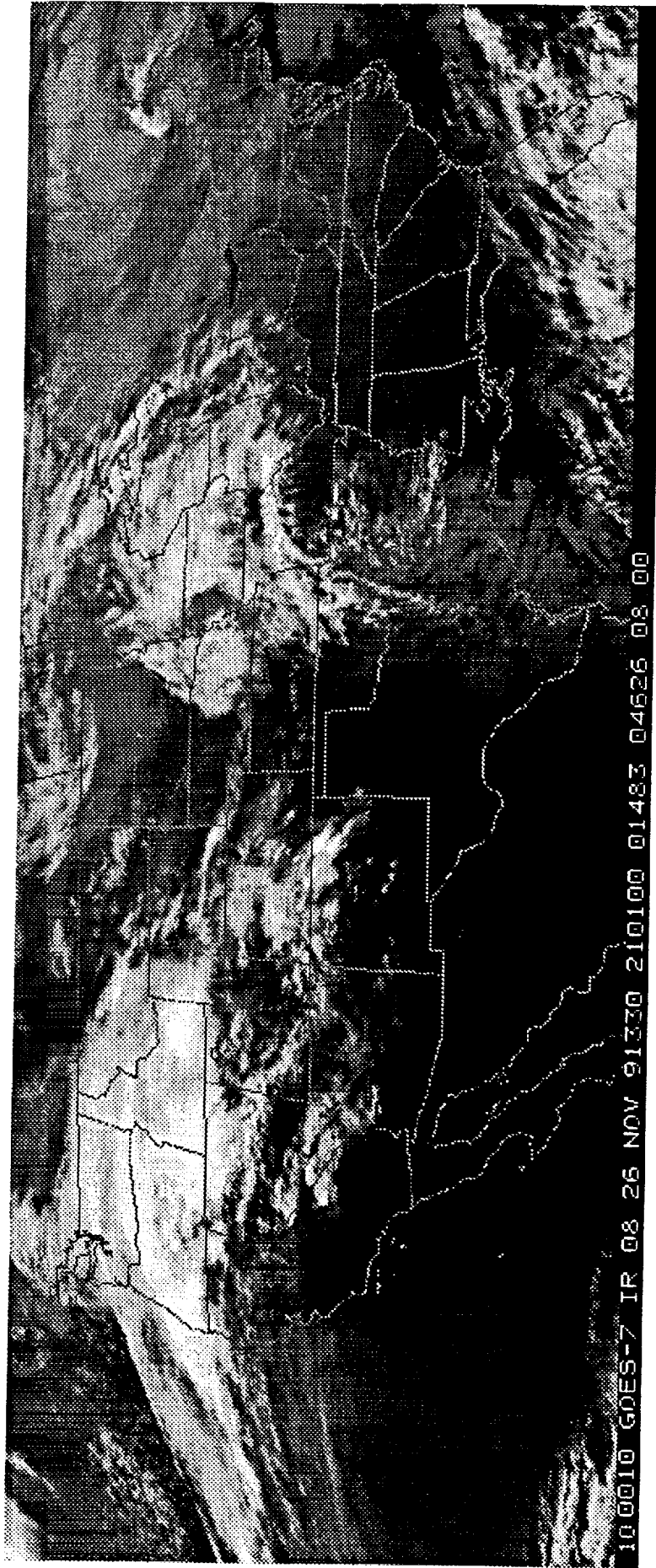
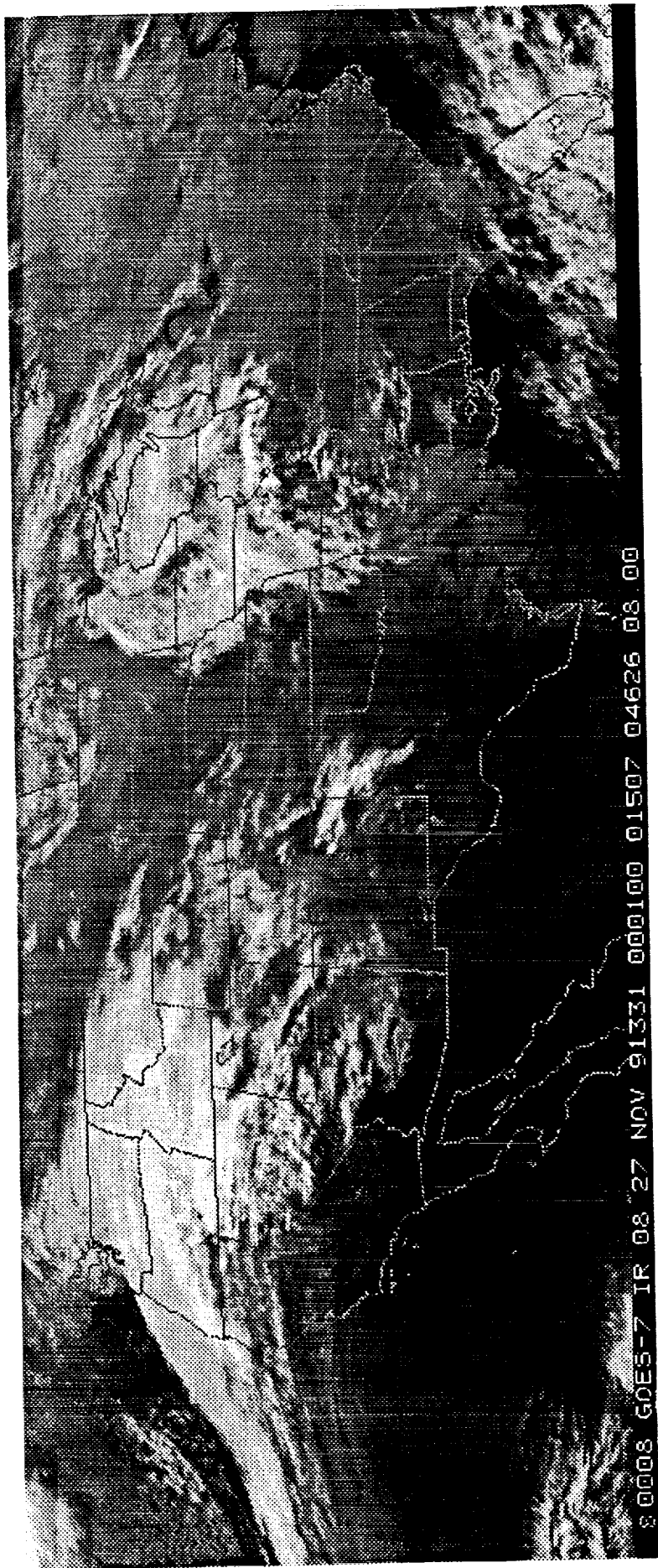


Fig. 4









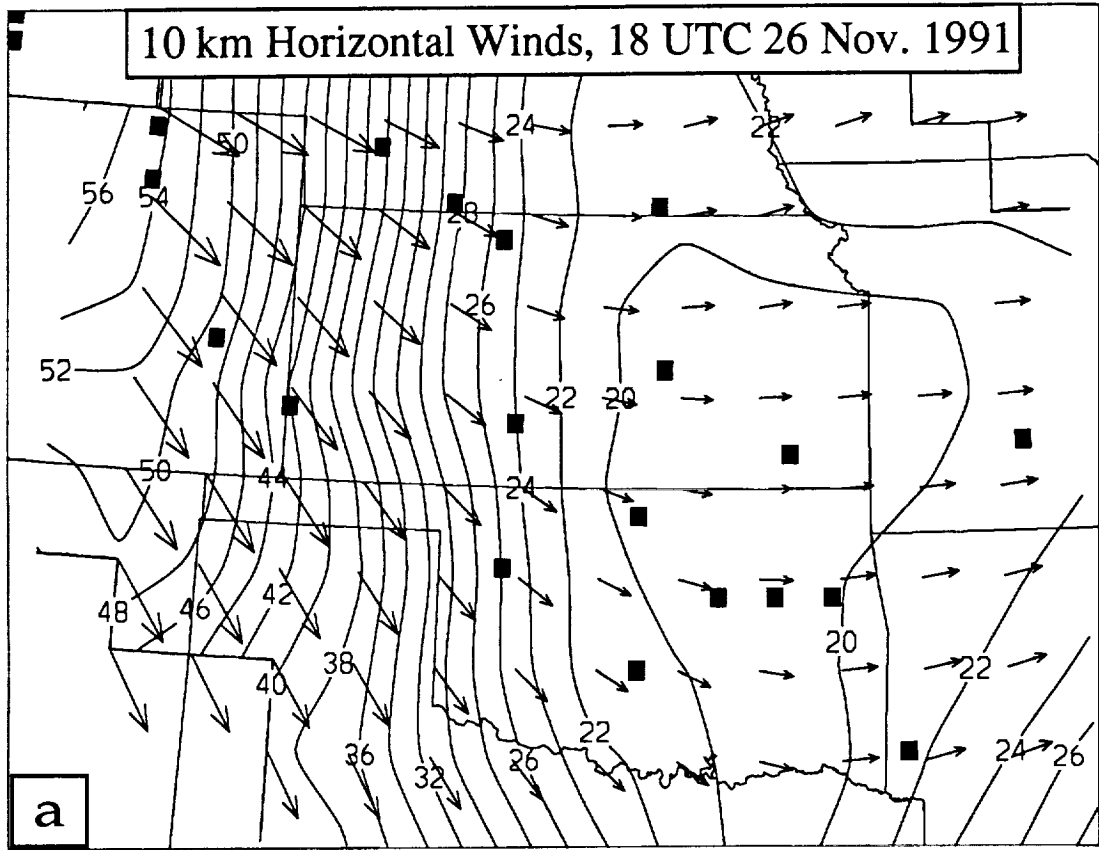


Fig. 6a

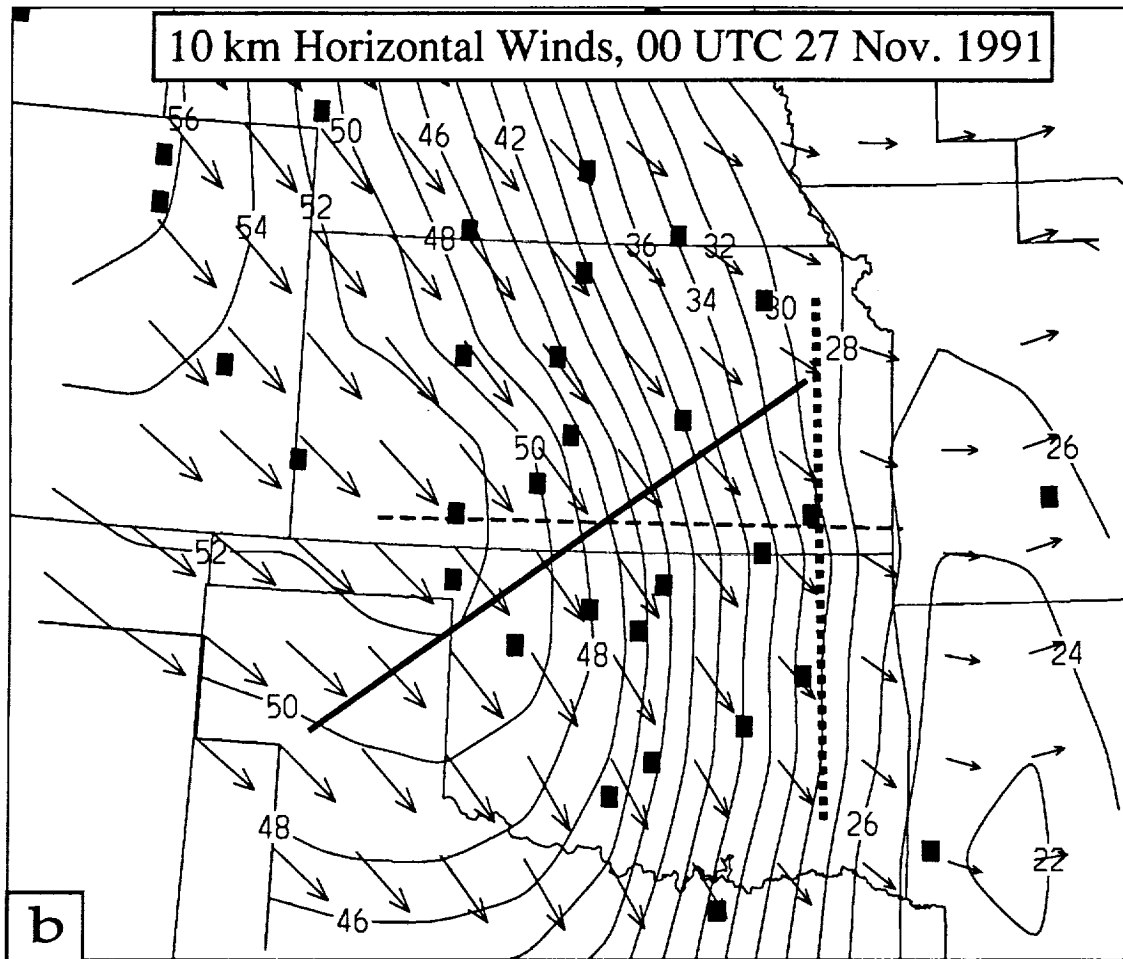


Fig. 6b

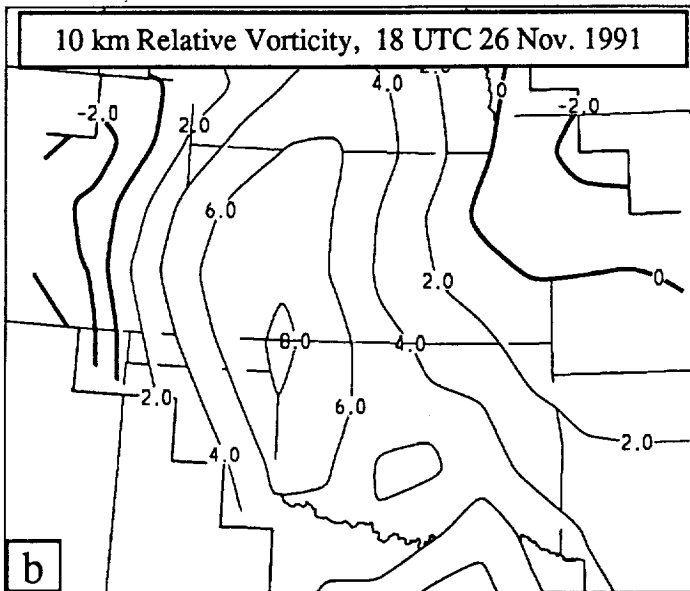
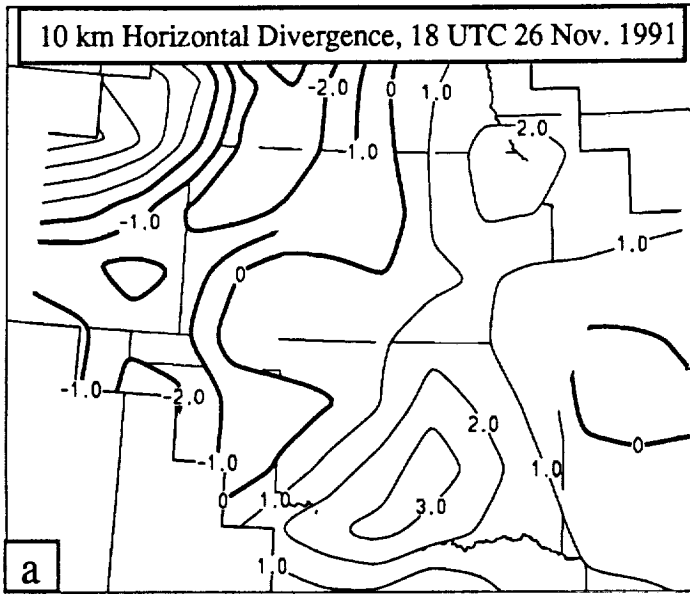


Fig. 7a & b

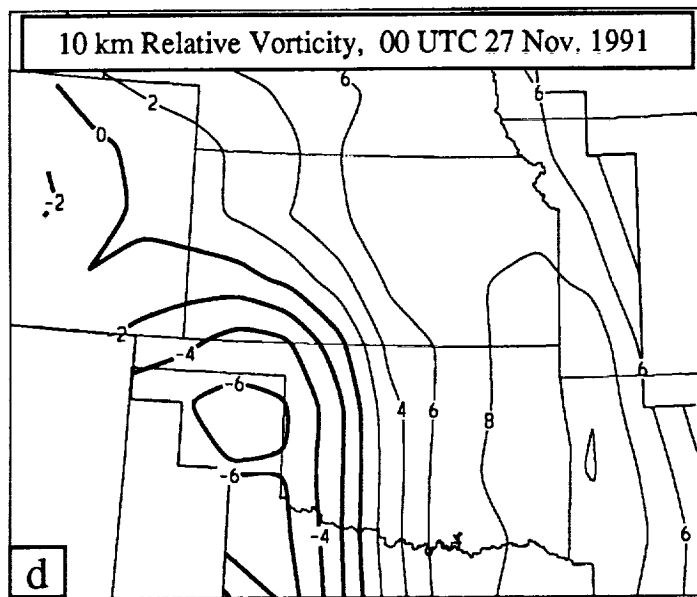
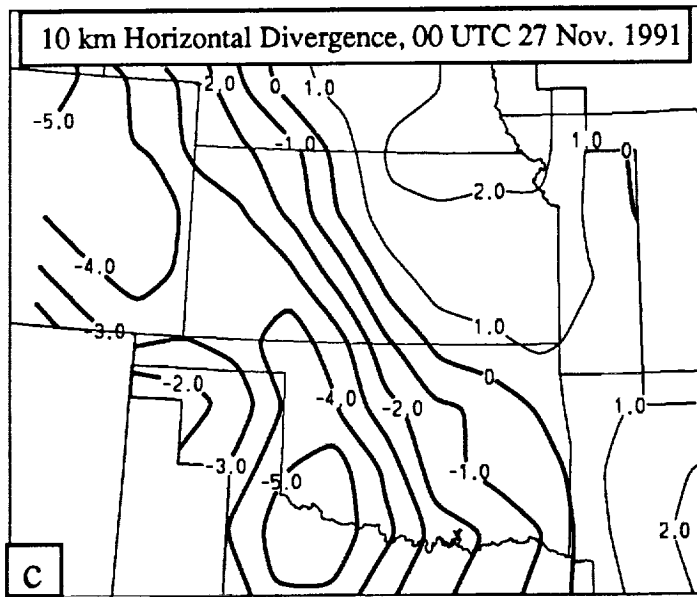


Fig. 7c & d

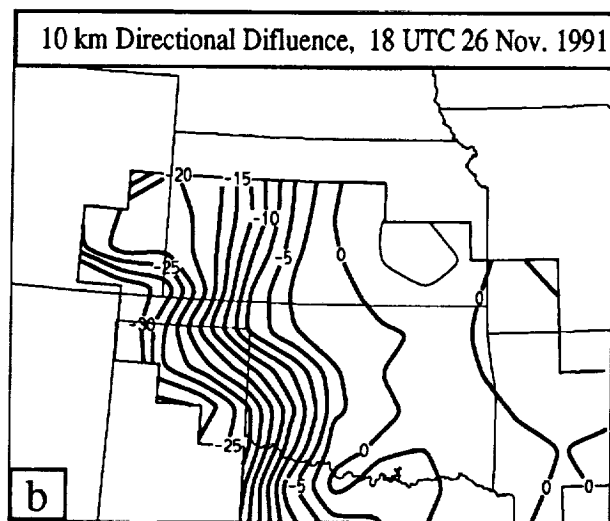
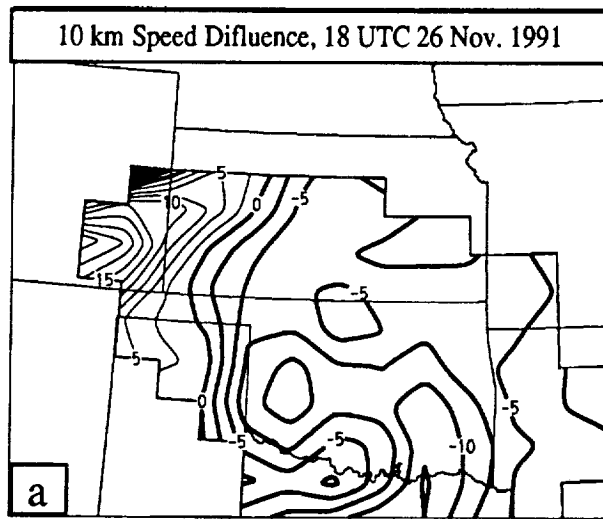


Fig. 8a & b

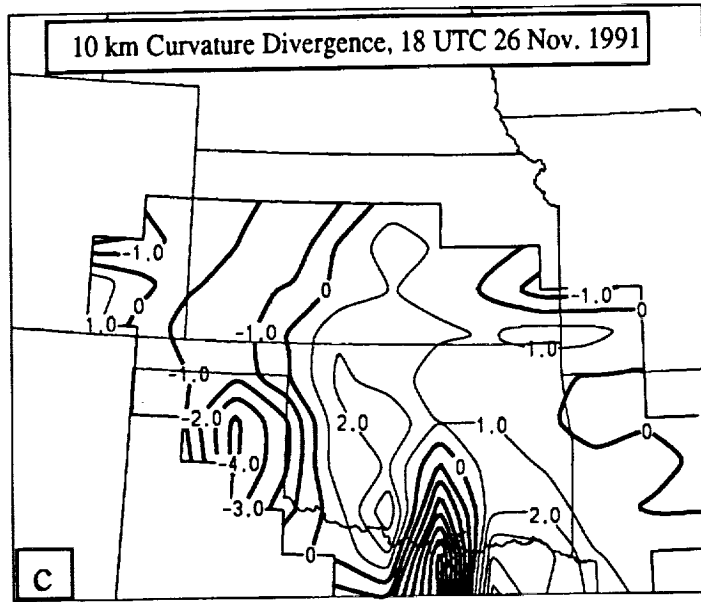


Fig. 8c



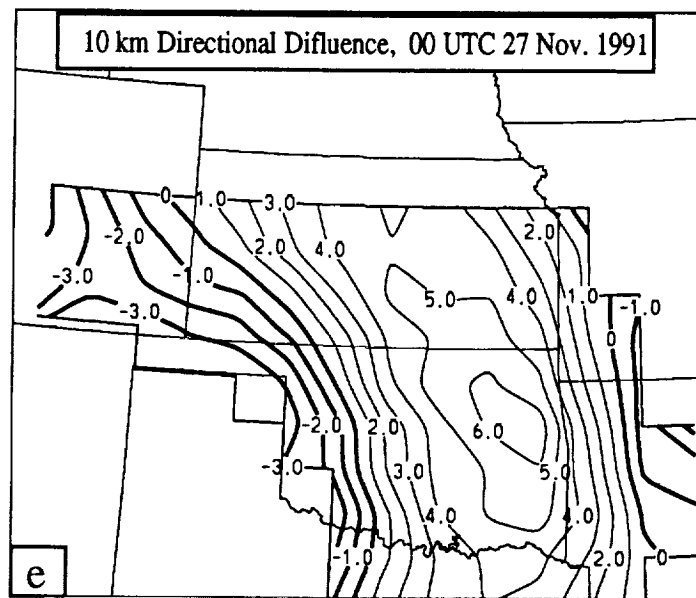
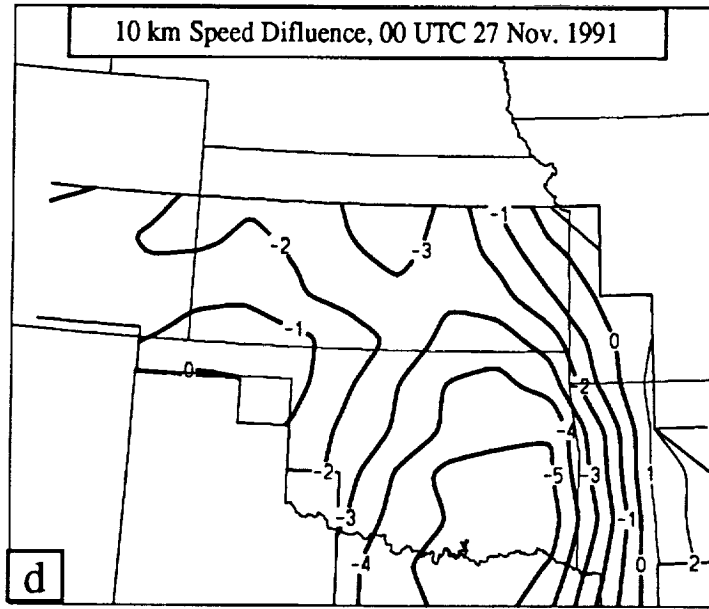


Fig. 8d & e

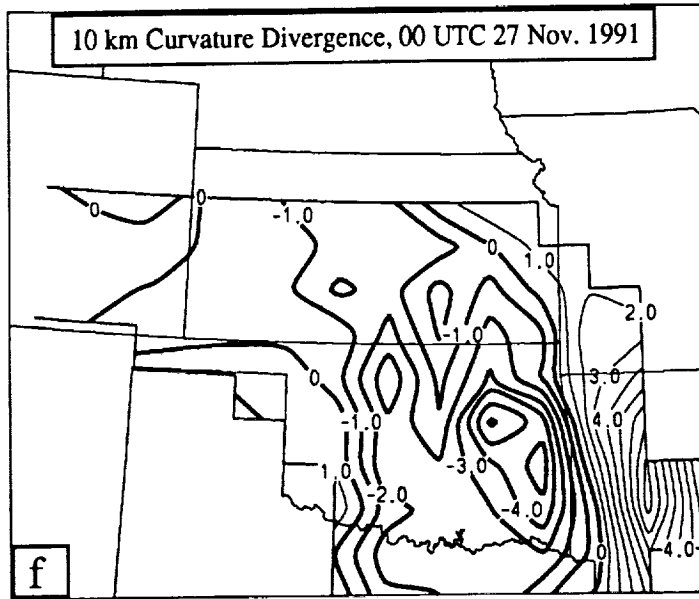


Fig. 8f

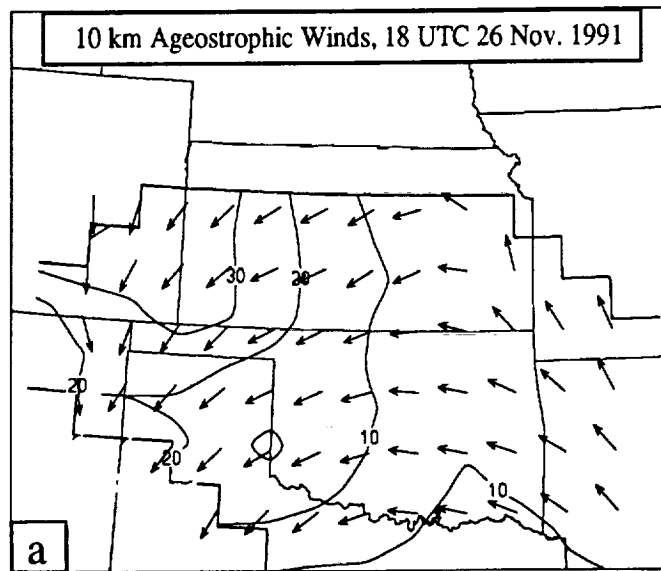


Fig. 9a

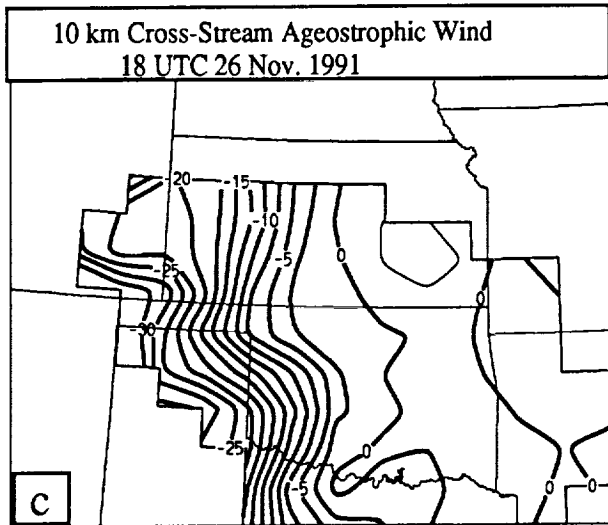
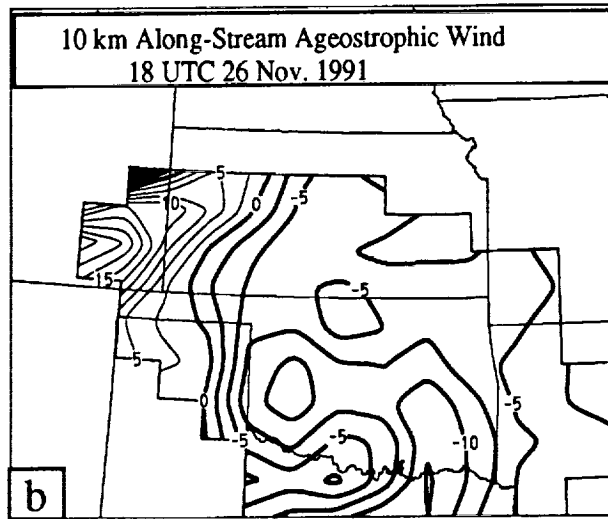


Fig. 9b & c

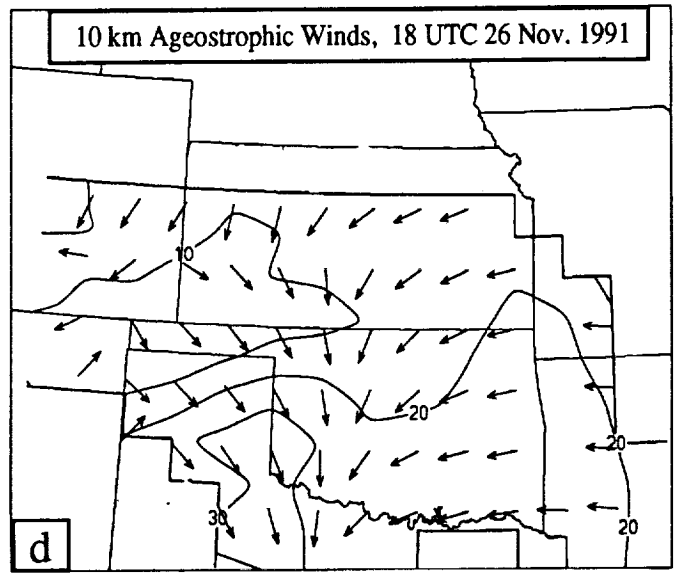


Fig. 9d

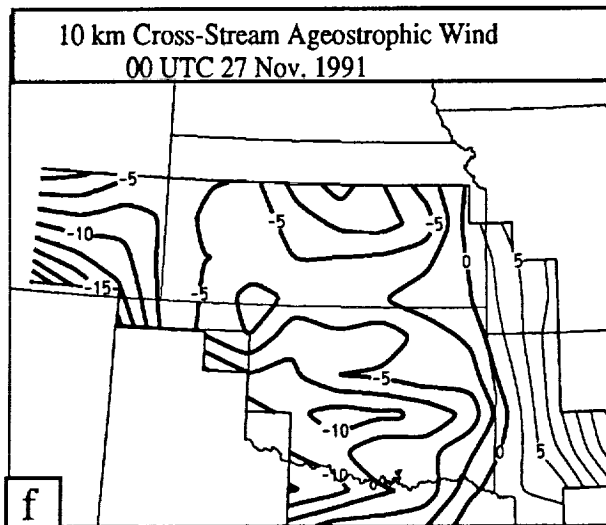
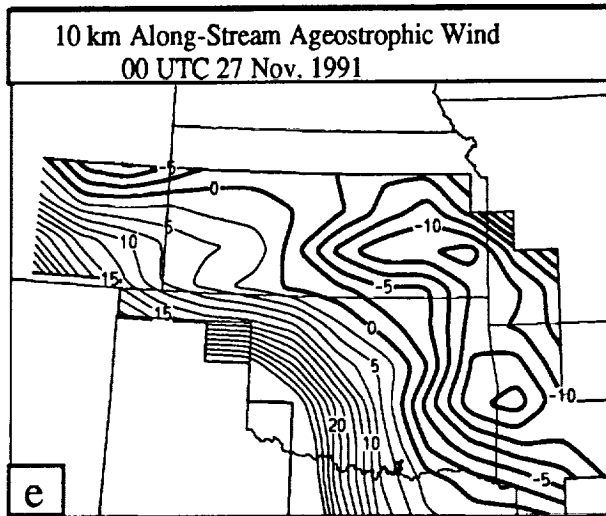


Fig. 9e & f

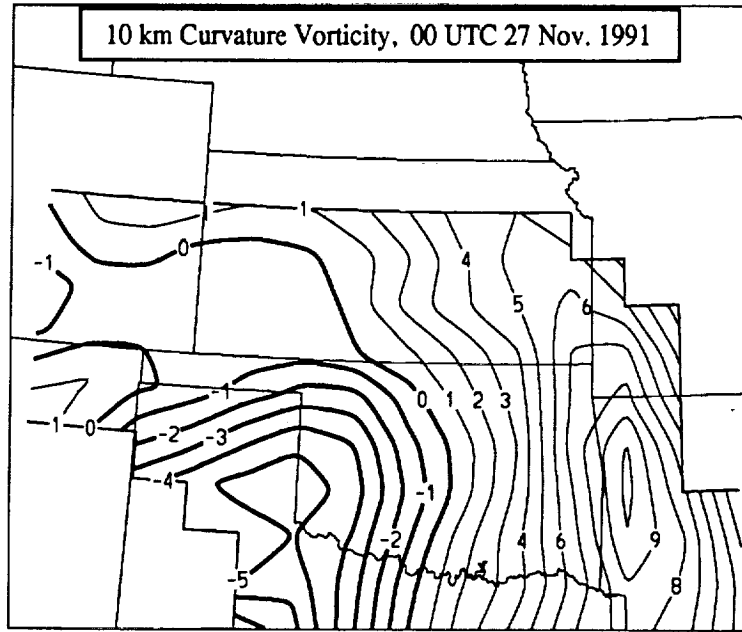


Fig. 10

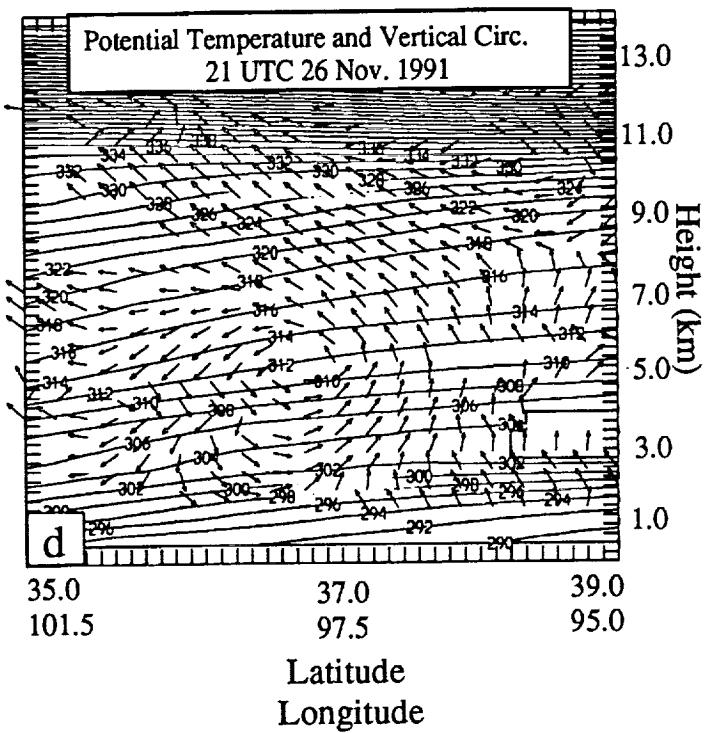
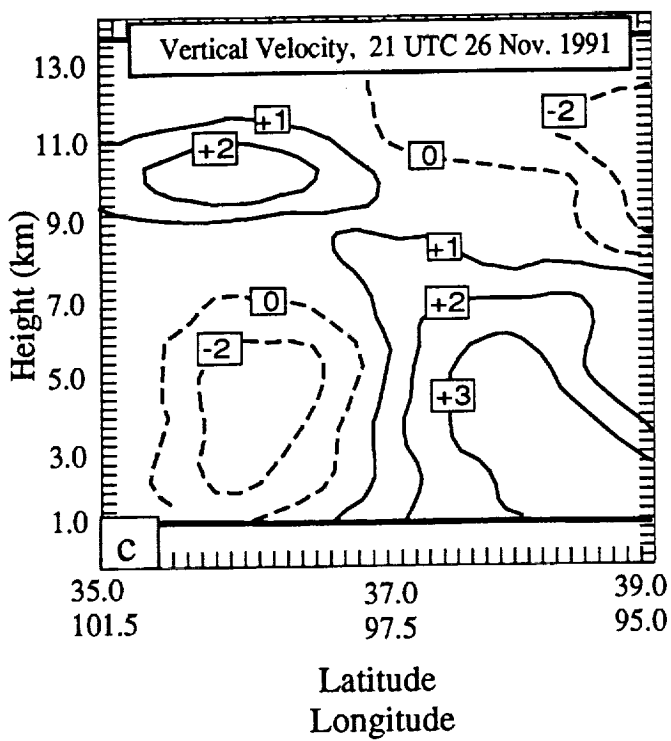
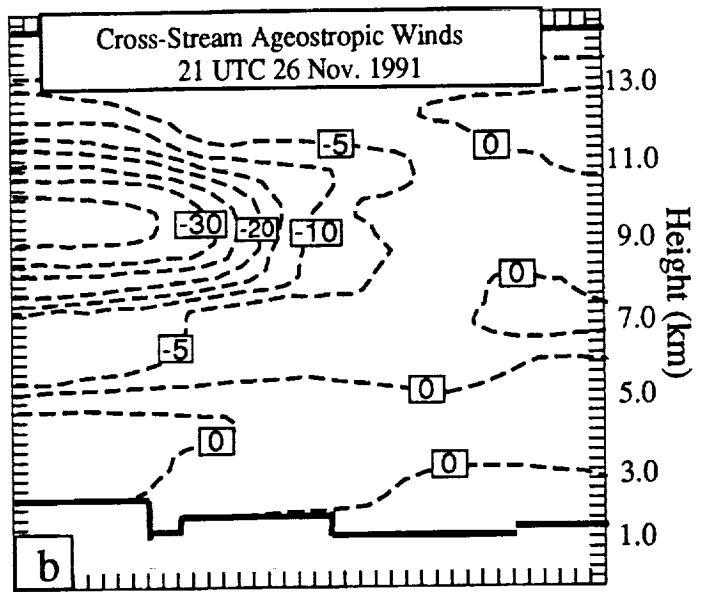
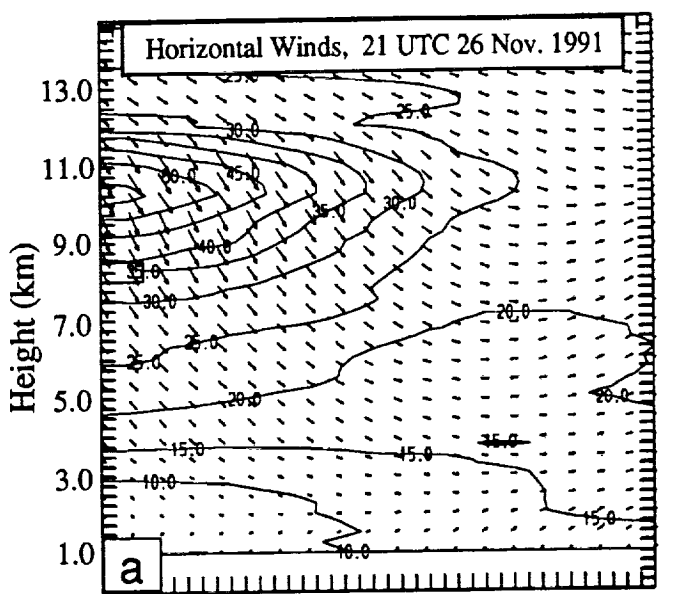
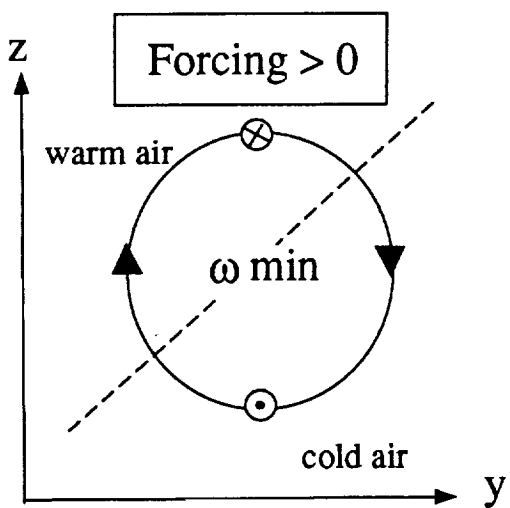
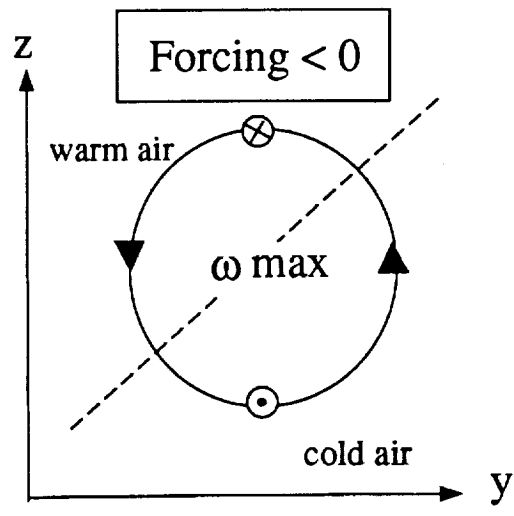


Fig. 11





(a)



(b)

Fig. 12

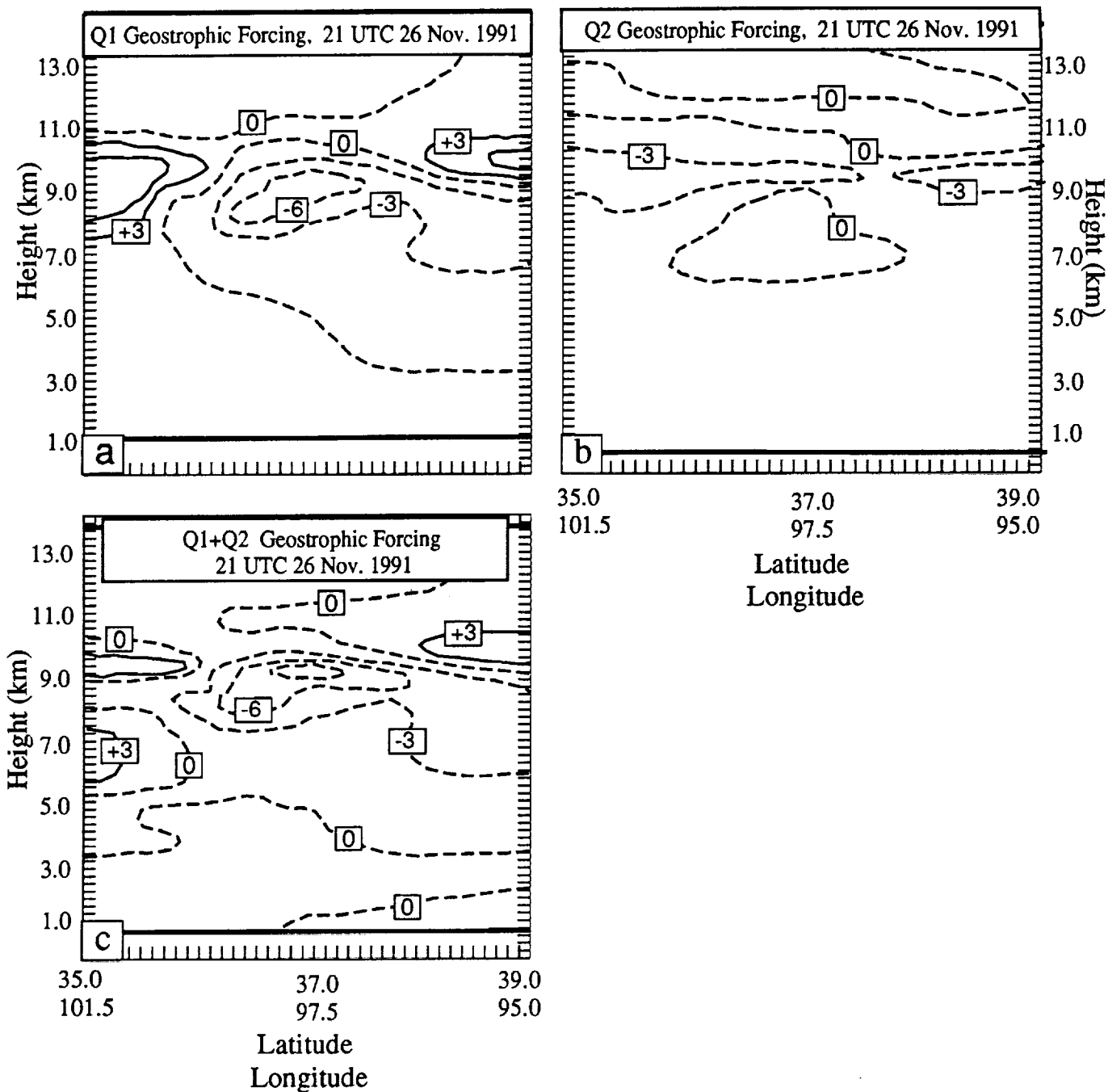


Fig 13

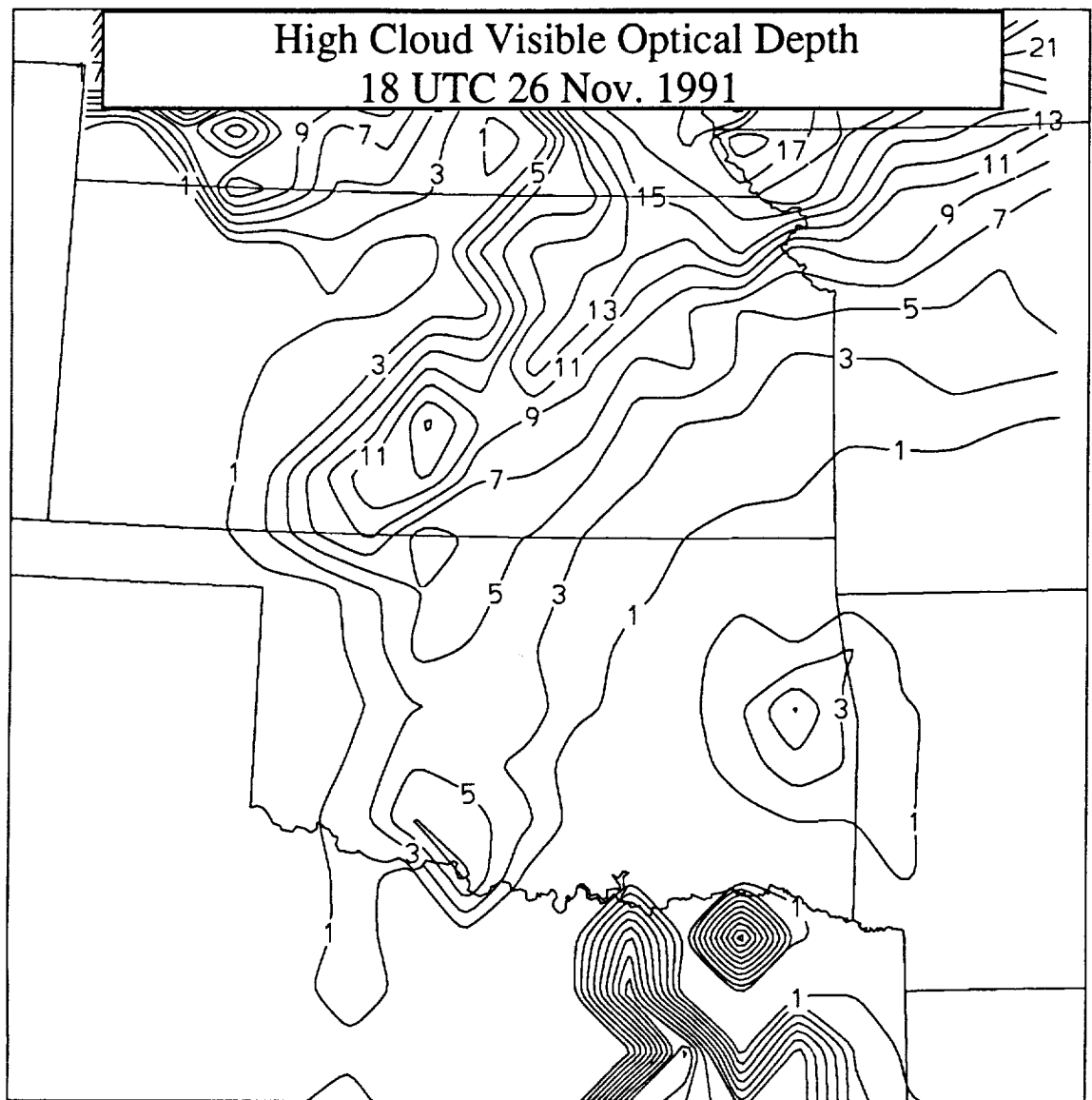
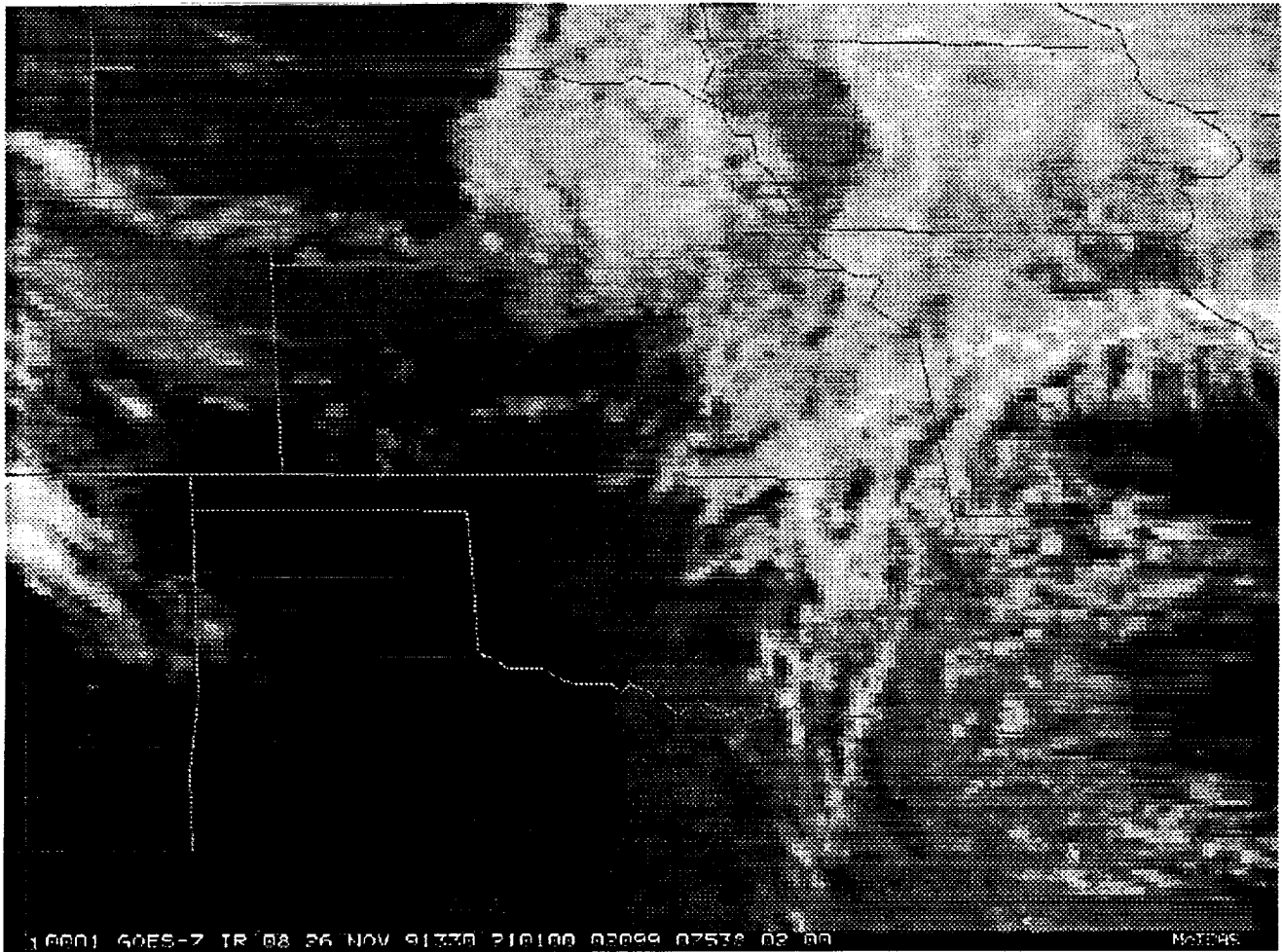
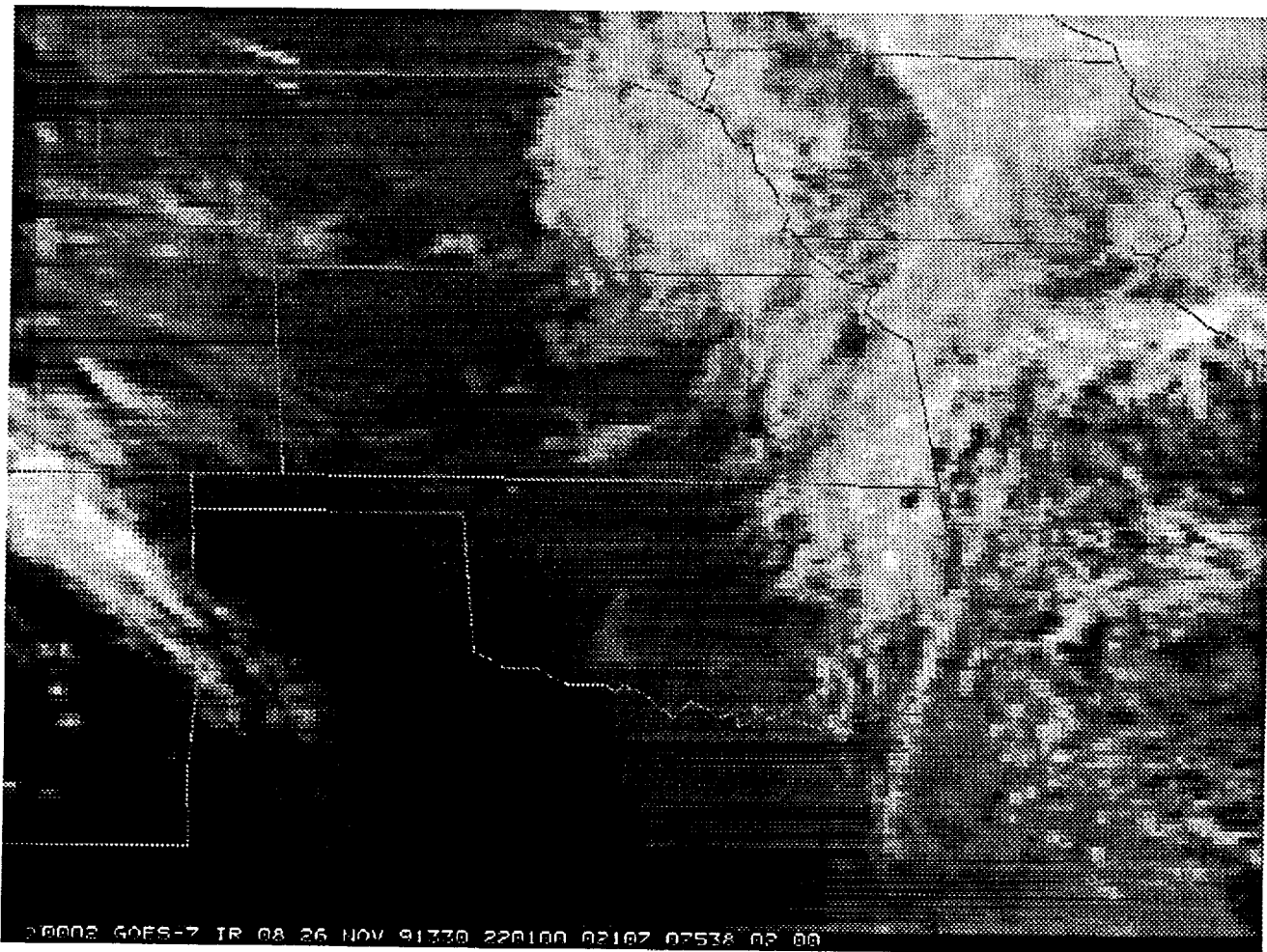
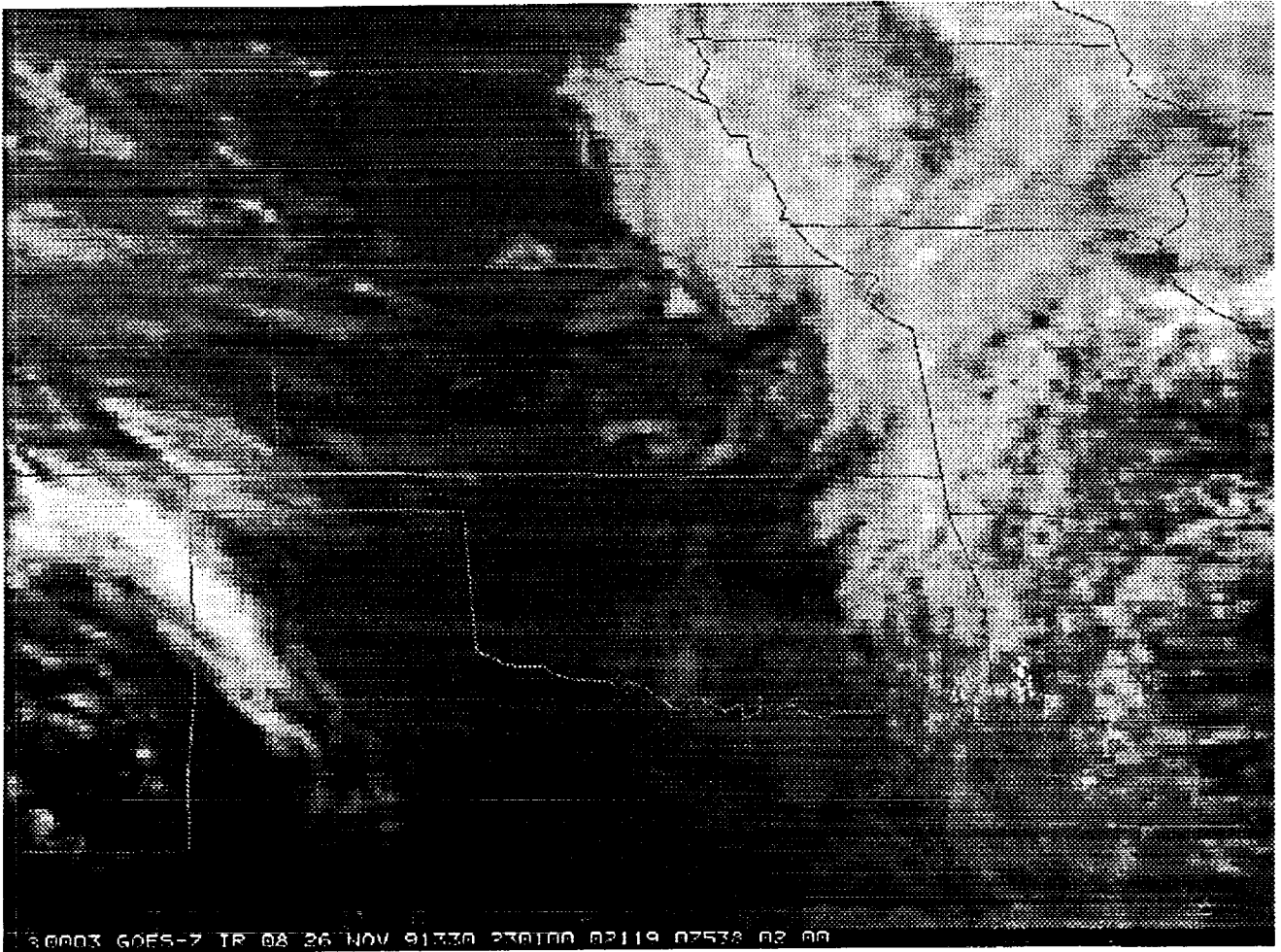


Fig. 14

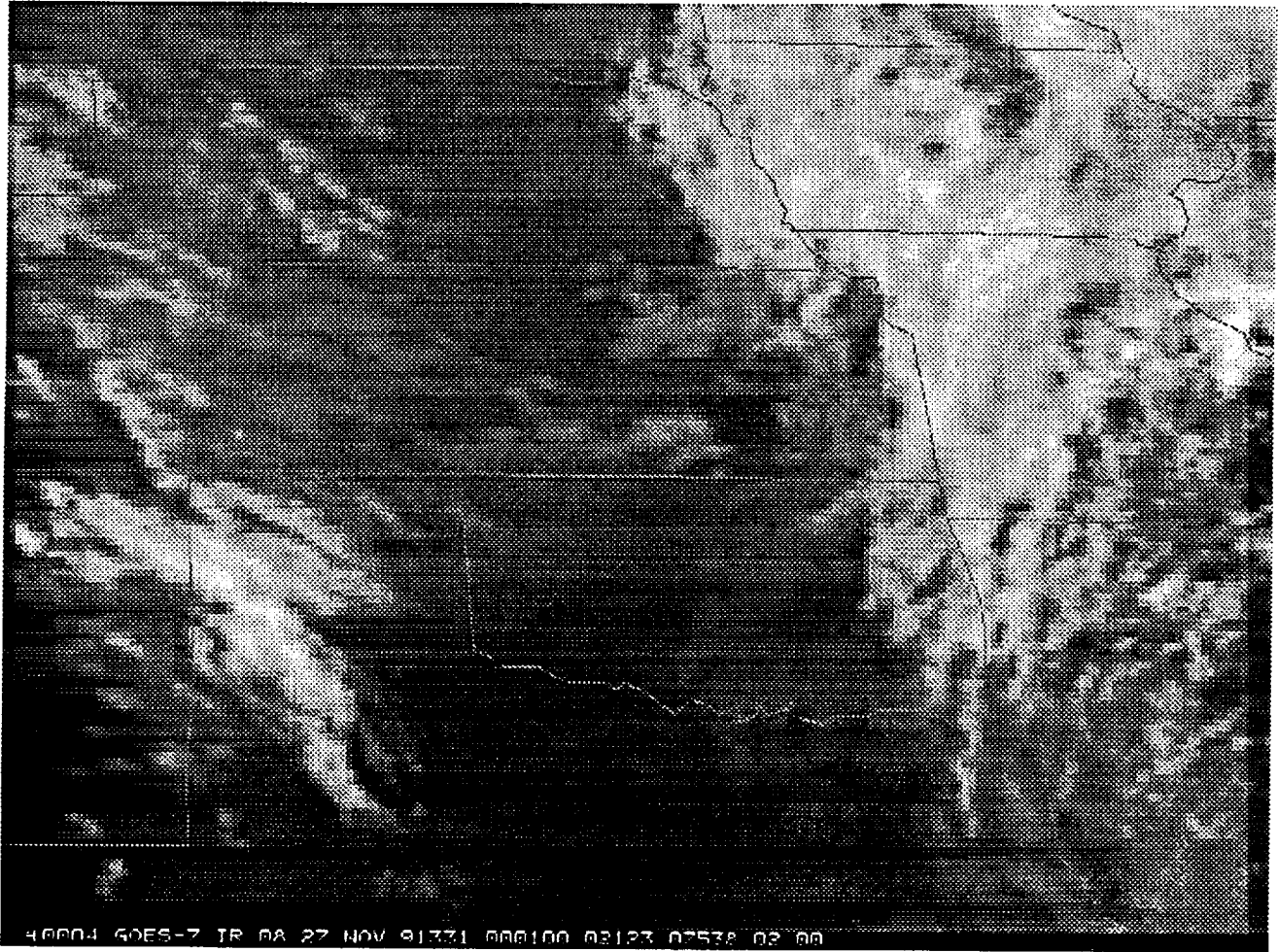






15c





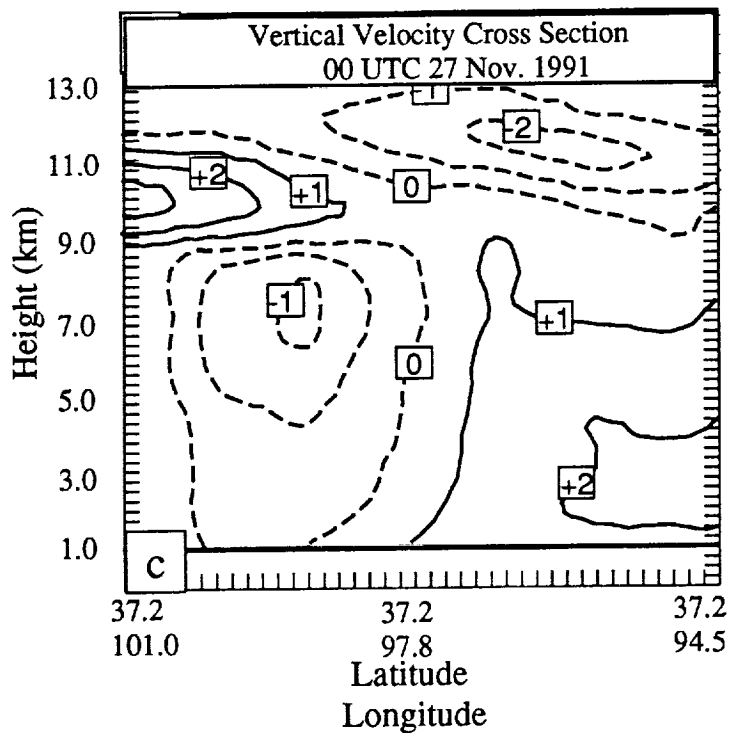
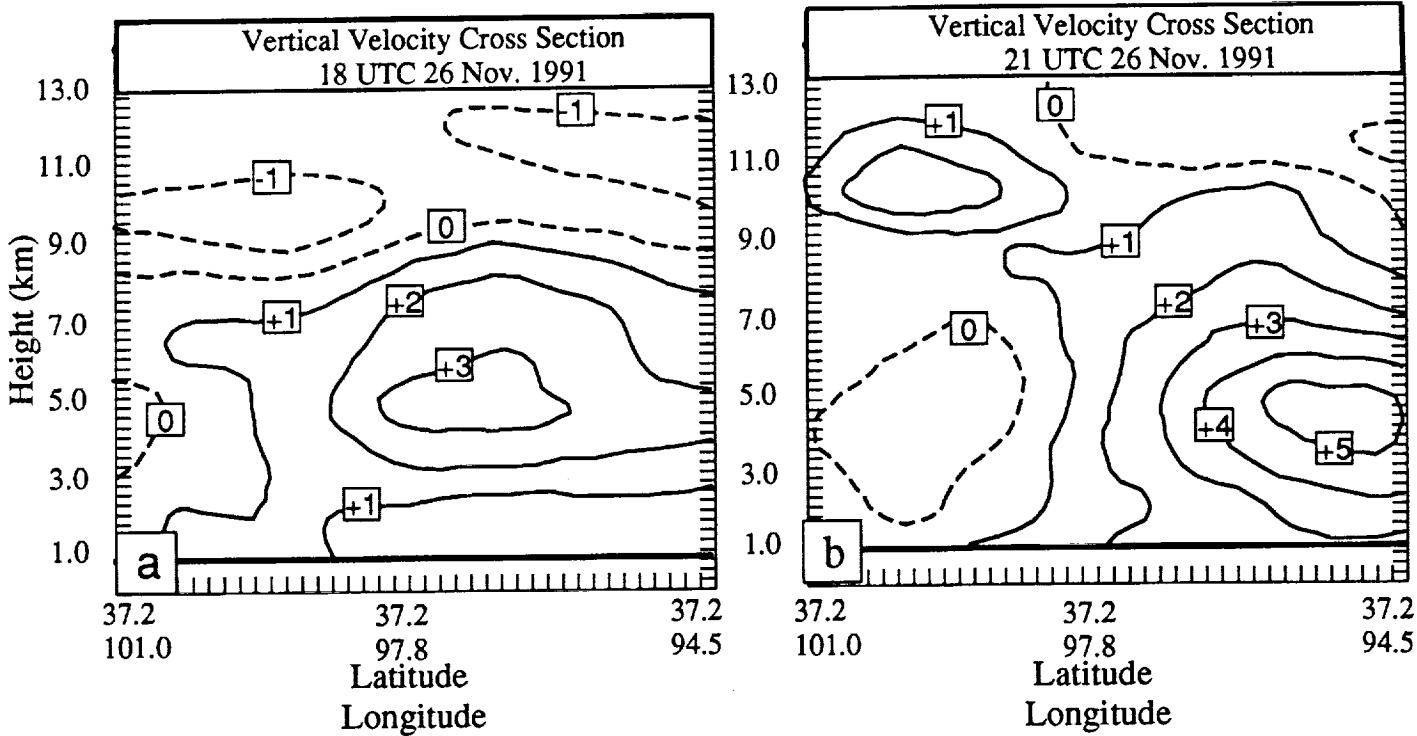


Fig. 16



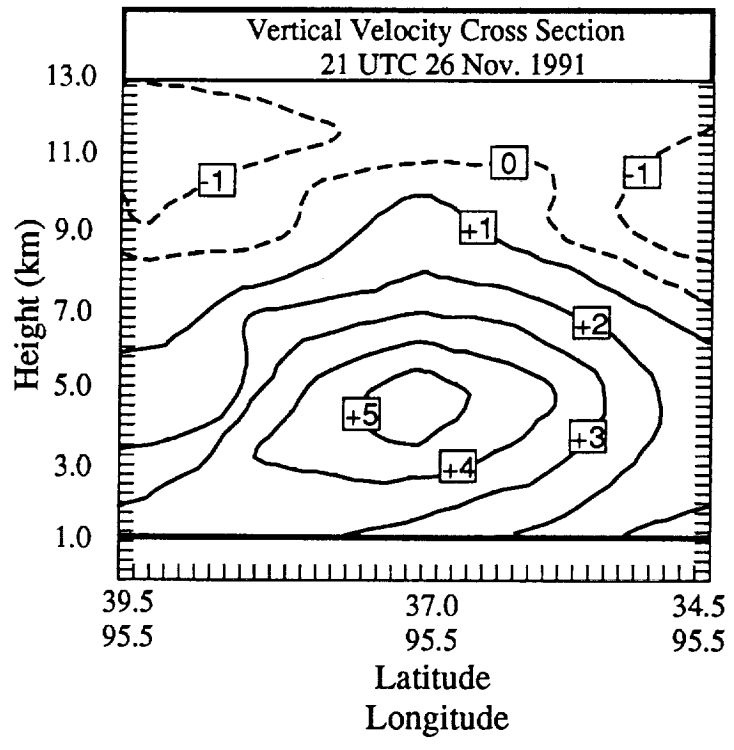


Fig. 17

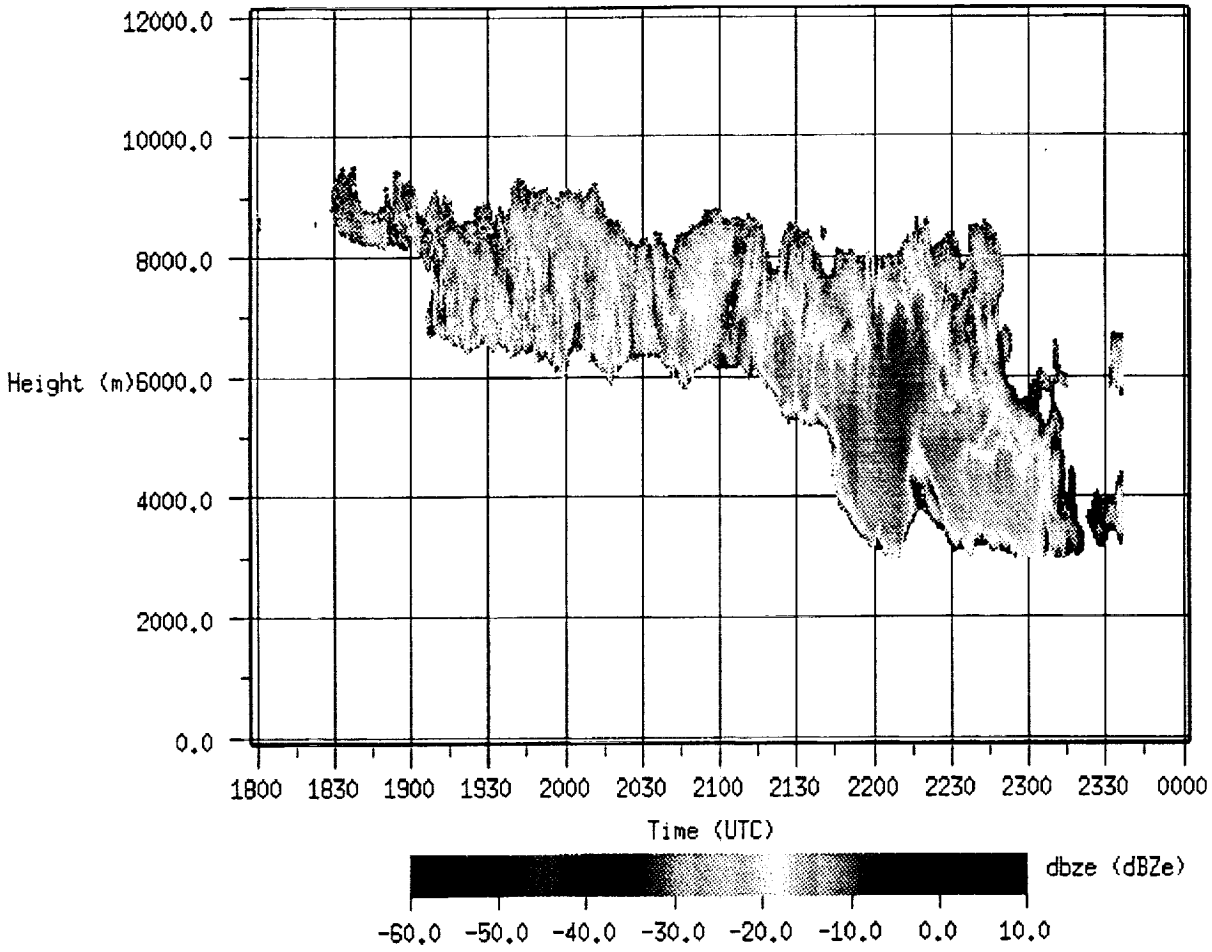


Fig. 18

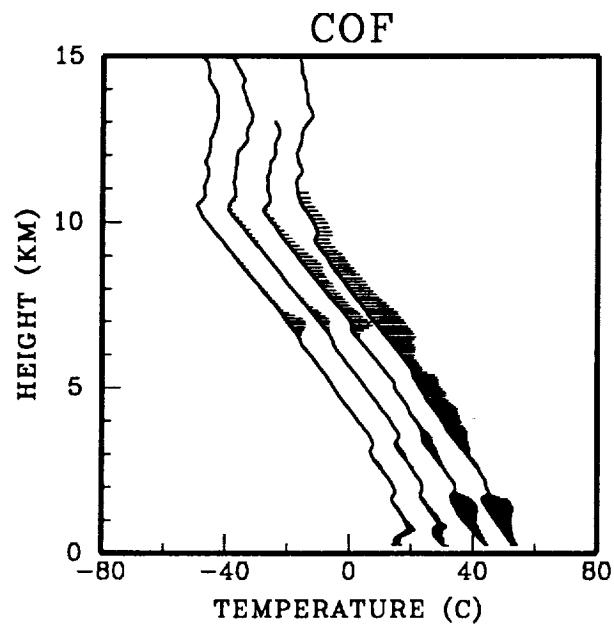
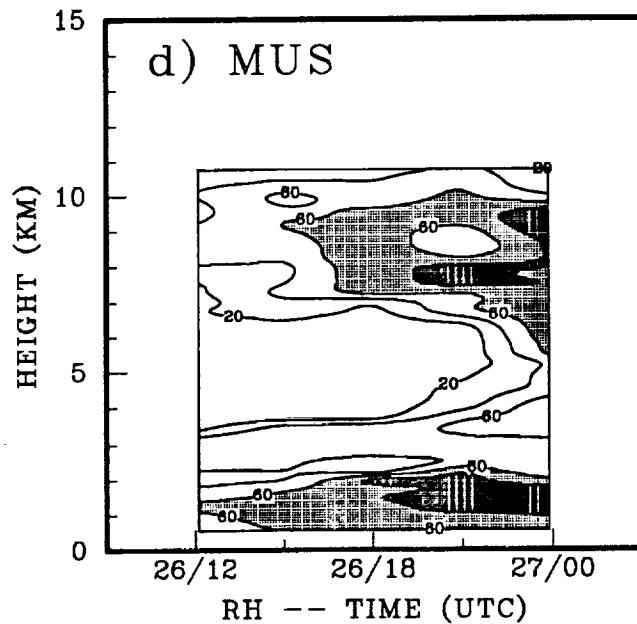
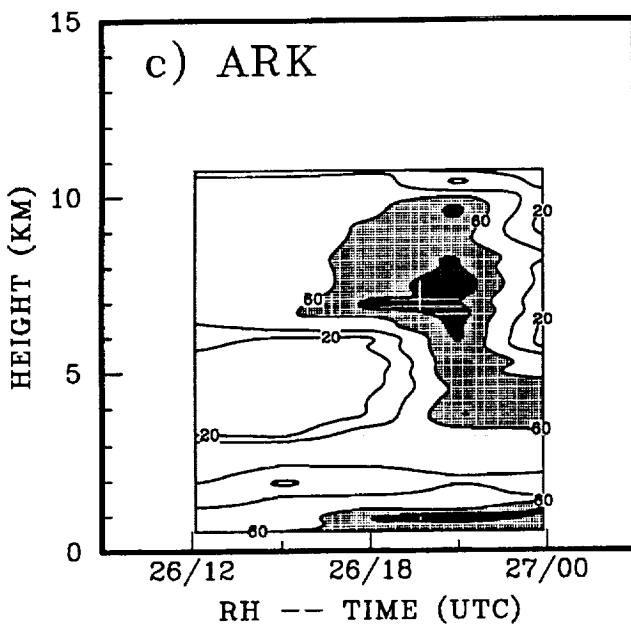
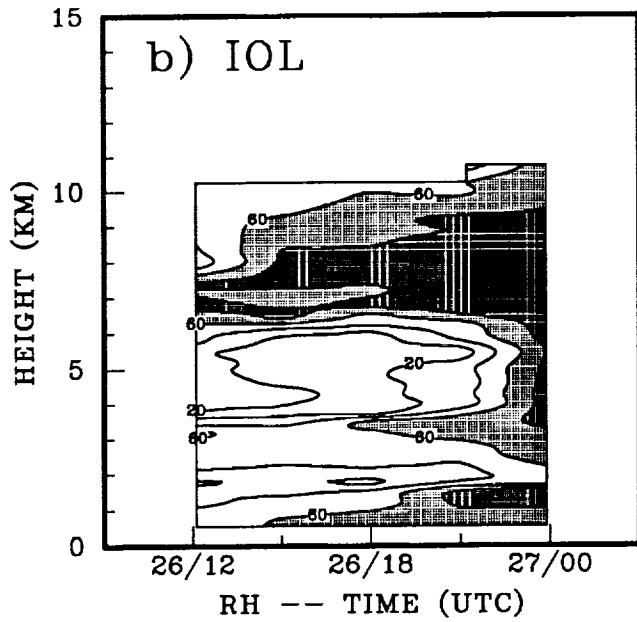
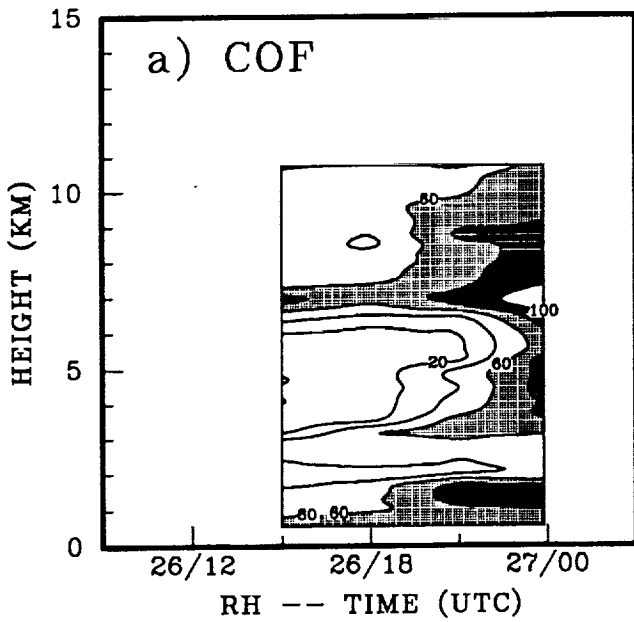


Fig. 19



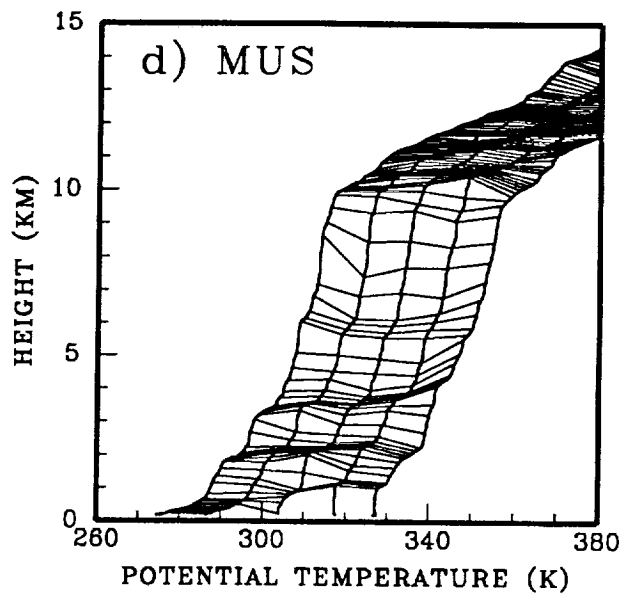
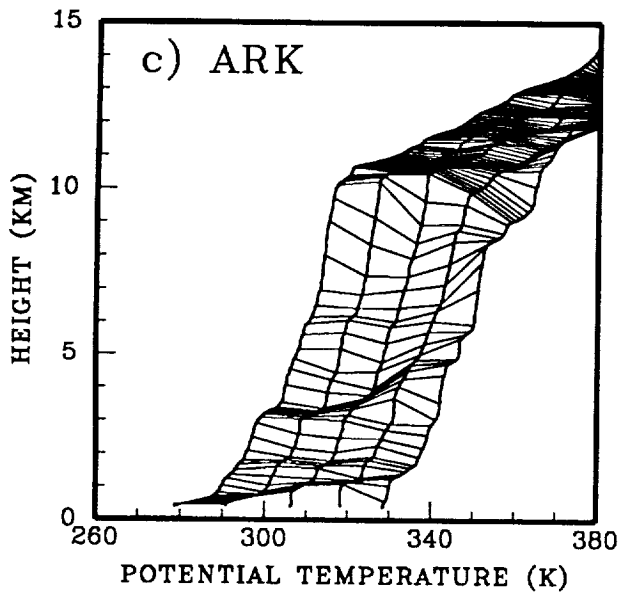
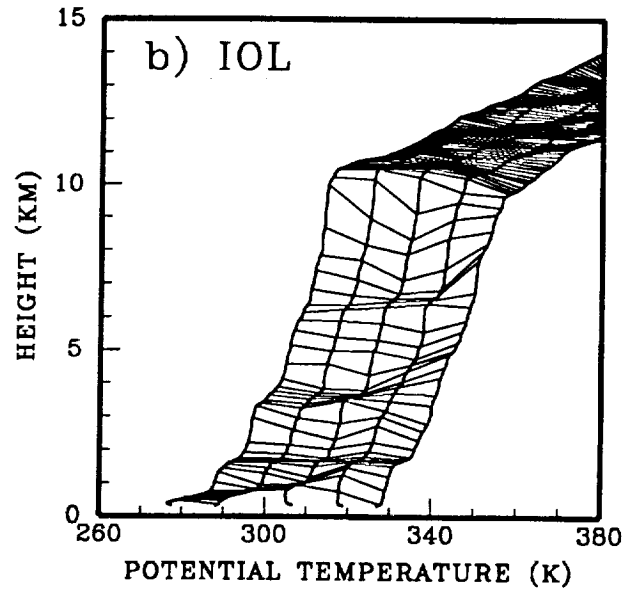
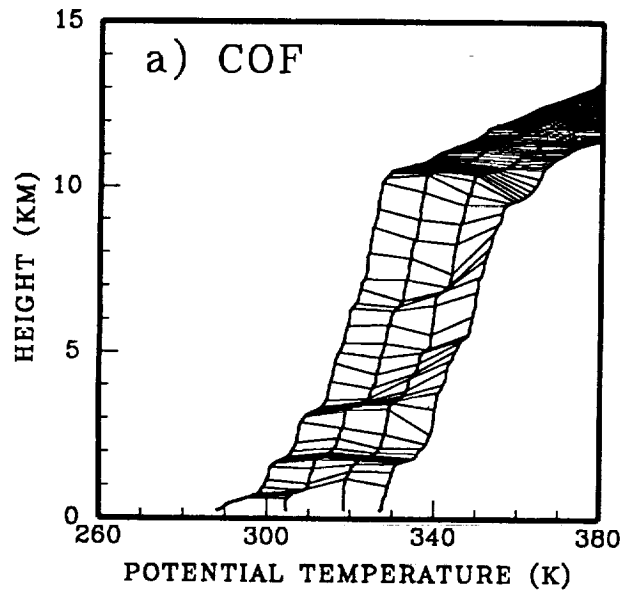


Fig. 21

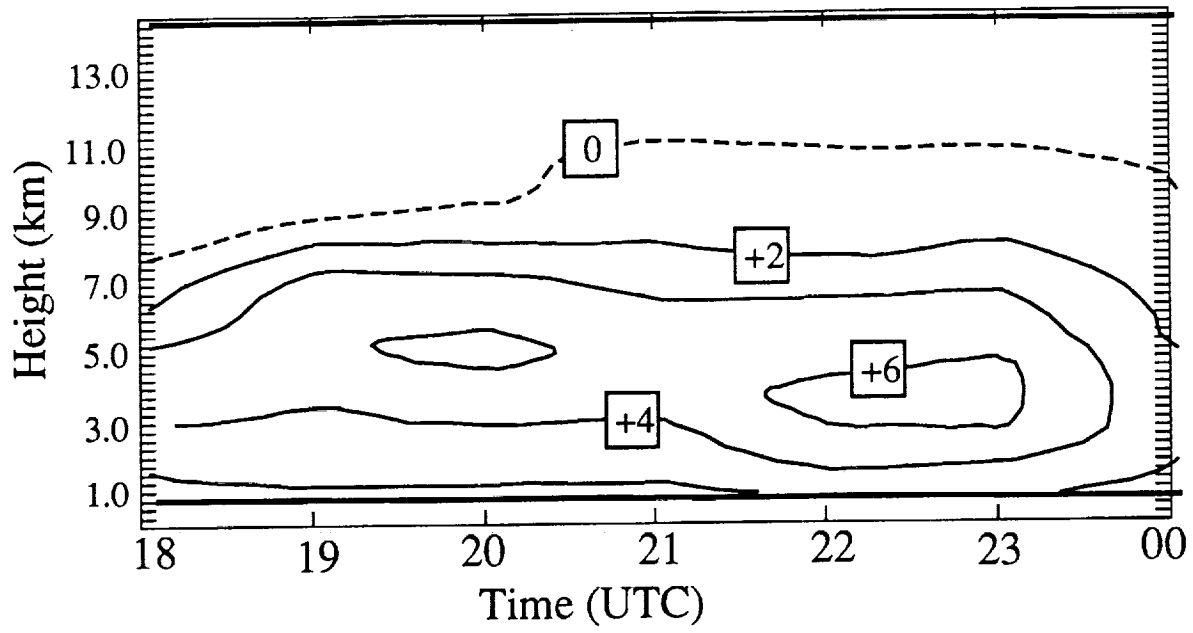


Fig. 22

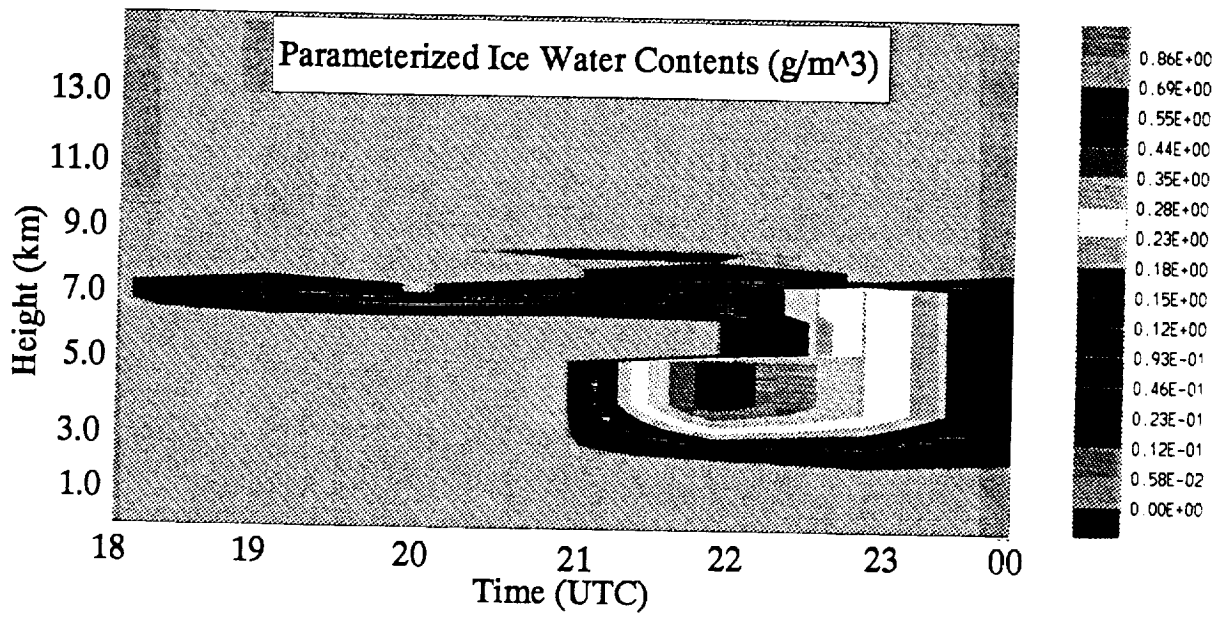


Fig. 23





## Vita

**Gerald G. Mace**



### **Education**

Ph.D. Meteorology	The Pennsylvania State University	University Park, PA (1994)
B.S. Mathematics (Summa Cum Laude)	Ohio University	Athens, OH (1989)

### **Professional Experience**

1994-present	Research Associate, Department of Meteorology, The Pennsylvania State University
1990-1994	NASA Goddard Earth Sciences Graduate Student Program Fellow Department of Meteorology, The Pennsylvania State University
1989-1990	Graduate Research Assistant Department of Meteorology, The Pennsylvania State University
1980-1987:	Meteorologist, U.S. Navy

### **Publications** (*refereed journals*)

Mace, G. G., D. O'C. Starr, T. P. Ackerman and P. Minnis, 1994: Examination of coupling between an upper tropospheric cloud system and synoptic scale dynamics diagnosed from wind profiler and radiosonde data. Accepted for publication, *J. Atmos. Sci.*

Sassen, K., D. O'C Starr, G. G. Mace, M. R. Poellot, S. H. Melfi, W. L. Eberhard, J. D. Spinhime, E. W. Eloranta, D. E. Hagen and J. Hallet, 1994: The 5-6 December 1991 FIRE IFO II jet stream cirrus case study: the influence of volcanic aerosols. *J. Atmos. Sci.*, in press.



Gerald has two other manuscripts in preparation stemming directly from his graduate work and anticipates submission of these to peer-reviewed journals by the end of this calendar year.

The interaction that was fostered by the NAGESGSP Fellowship with you as Gerald's fellowship advisor at NASA Goddard proved to be an extremely valuable fringe benefit of the fellowship. Not only did Gerald benefit by the numerous visits to Goddard, but I found the exchange of ideas and information between us in relation to Gerald's work to be very productive.

Gerald is currently under my employ at The Pennsylvania State University as a post-doctoral research associate. He plans to seek a faculty position at a university within the next two years and to continue active research in the area of cloud-climate interaction.

Sincerely,



Thomas Ackerman  
Associate Professor and  
Principal Investigator

Enclosures

cc: NASA Scientific and Technical Information Facility

